Characteristics of a cavity soliton laser based on a VCSEL with frequency selective feedback

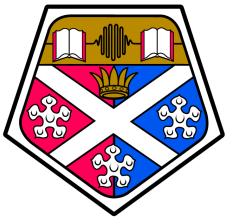

Neal Radwell

Department of Physics and SUPA

University of Strathclyde

A thesis presented in the fulfilment of the requirements for the degree of

Doctor of Philosophy

2010

‘This thesis is the result of the authors original research. It has been composed by the author and has not been previously submitted for examination which has led to the award of a degree.’

Signed: Date:

I would like to dedicate this thesis to my loving parents.

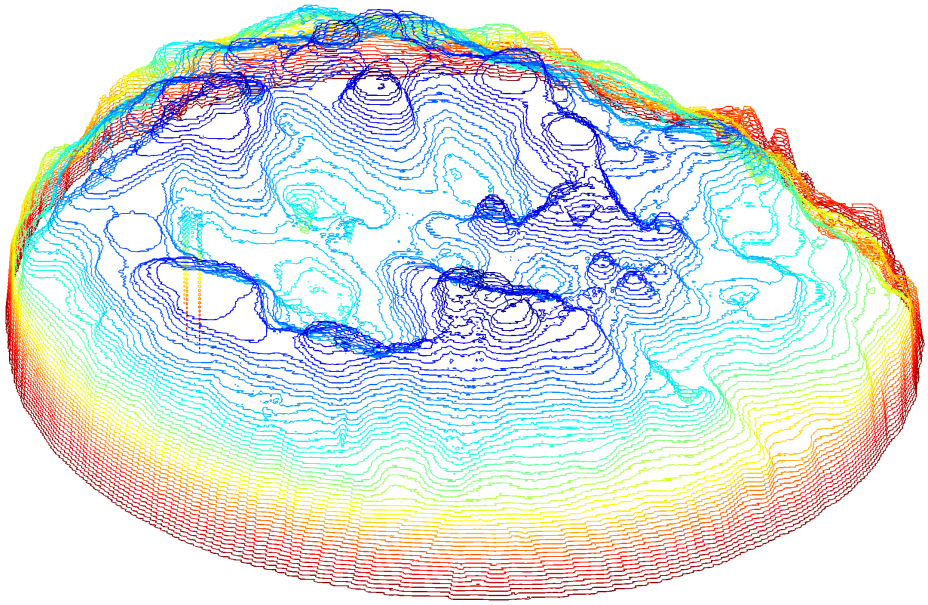

Acknowledgements

I would first like to thank Thorsten who has been the ideal supervisor, always having time for a discussion and always guiding me in the right direction. I am simply so grateful for his help and guidance and it is because of him that this thesis even exists.

I would like to acknowledge all the people that have made my time as a PhD student both enjoyable and successful. I would like to acknowledge Yann, as without his help in the initial months, I would probably still be lost and confused. Next I would like to thank the guys from the office, past and present, in no particular order; Kyle, Ian, Wei, Kenneth, Mateusz, Alessio, Matt, Stef, Chris, Griff, Aline and Yoann.

I would also like to thank the guys from CNQO doing the theory and offering great insights into my experiments, namely Gian-Luca, Willie, Craig and Andrew.

I would further like to thank the guys from Muenster with whom I worked on many successful experiments, and would like to thank Patrick and Berndt in particular for making my stay in Germany one to remember.

Thanks also to Bob and Ewan for their help keeping the lab in one piece.

Lastly I would like to thank Gael, who is just the raddest person on earth.

Contents

List of Figures

Abstract

In this thesis a cavity soliton laser (CSL) based on a vertical-cavity surface-emitting laser (VCSEL) with feedback from a volume Bragg grating (VBG) is demonstrated and its properties are investigated. This system is capable of supporting self-localised lasing spots which are confirmed to be laser cavity solitons (LCS), i.e. small coherent emitters (micro-lasers). They are bistable and can be switched on and off by an external optical beam.

The LCS are shown to have several freedoms which are not present in other cavity soliton realisations, in that the frequency, phase and polarisation properties of each LCS are essentially free parameters. A consequence of this is that the LCS are capable of locking in frequency and phase by appropriate tuning of parameters. The freedom of polarisation leads to each LCS having unique polarisation angle, controllable by the addition of polarising elements.

Strong temporal dynamics are also found both transiently during switch-on and as stable steady state oscillations. Switching is found to follow a minimum threshold power requirement and spectro-temporal analysis reveals the tendency for the LCS to show strong oscillations during switch-on which results from a transient spectral broadening.

The LCS have also been observed to produce pulse-like temporal intensity oscillations which are associated with a parameter region in which several external cavity modes are excited. Pulse like behaviour is not typical however and many other forms of oscillations are possible.

The positions and thresholds of the LCS are believed to be dictated by an unintended underlying spatial variation of cavity parameters referred to as disorder. Once this disorder is mapped, a compensation scheme is proposed and tested. A spatial light modulator (SLM) is used to shift the relative thresholds of 2 LCS and this method is proposed as a viable method of compensation and this should facilitate the realisation of future applications.

Chapter 1

Introduction

Some years ago it was discovered that nonlinear optical systems could support soliton-like structures, that is structures which do not diverge or disperse in the presence of diffraction or dispersion. Initially the interest sparked from the large variety of physical systems which display nonlinearity. Systems which were capable of supporting a patterned state in conjunction with an unpatterned state were investigated quite extensively [8, 21, 22, 23, 26, 30, 32, 37, 47, 61, 66, 72, 81] and this lead to these structures being considered for applications [7, 9, 37, 115]. When realised in an optical system then the bistable nature of these structures makes them candidates for optical bits, since they are stable in the off (0) state and also in the on (1) state for the same input power. It would therefore be ideal if these patterns could be disconnected, such that many of these optical bits could be realised in the same device.

It was discovered that a certain region of parameters exists where only a single part of the overall pattern is stable, leaving only a single, independent high intensity spot [53]. If these spots were formed within a cavity, these bistable, independent spots which are stabilised by nonlinearity became known as 'cavity solitons' (CS). If many CS could be created in one device then this would be an excellent candidate for optical memory.

There were several systems capable of supporting CS and early investigations of laser systems which support CS in non-semiconductor media [17, 35, 121] used saturable absorption to induce bistability into a laser system, with the coexistence between different spatially extended states being a prerequisite for the

existence of CS, e.g.[2] however if they are to be used in optical networking then the CS creation system should be compact (μm scale) and have fast inherent timescales (ns or better) to meet modern bandwidth requirements. The best candidates appeared to be semiconductor microcavities with their nonlinear gain regions, compactness and quite fast fundamental timescale (1 ns). The prevalent semiconductor microcavity for investigations on CS was the vertical-cavity surface-emitting laser (VCSEL). The VCSEL alone is not enough to support CS however and the first demonstration of CS in a semiconductor device was performed in a VCSEL with an externally injected laser beam to support optical bistability [15]. The VCSEL device was much larger than a standard single-mode VCSEL, with an aperture diameter some 40 times greater than standard devices and this was in order to support many CS simultaneously.

The seminal experiment of [15] demonstrated that the CS in this externally optically pumped system could be formed, and switched on and off by external injection, without changing the VCSEL parameters, as theoretically predicted. Some drawbacks were identified with this system however, as the reliance on optical injection with a high degree of spatial and temporal coherence is disadvantageous for applications. Thus, systems which did not rely on the optical injection were sought after and thus the idea of a semiconductor based cavity soliton laser (CSL) was born. Such a CSL could be realised if a bistability mechanism could be added to an electrically pumped device. The first semiconductor CSL was realised only quite recently by inducing bistability via frequency-selective feedback to a broad-area VCSEL [85, 108, 118, 119, 127]. A scheme employing gain and saturable absorption of two face-to-face coupled VCSELs structures soon followed [41, 42] and modeling, fabrication and characterisation of monolithic structures is progressing well [11, 33].

The most obvious advantage of a self-sustained CSL for applications is the absence of the external coherent beam which requires a controlled detuning to the resonance of the microcavity. Furthermore in driven systems the CS are 'slaved' because their phase, polarisation and frequency is locked to that of the HB. A CSL on the other hand – as any laser – has the freedom to choose its own phase because it originates from a spontaneous symmetry breaking. Assuming that the cavity is sufficiently isotropic and broadband, polarisation and frequency

of its output is also undetermined. In a CSL, every single CS within the laser aperture should have the freedom to chose between all these possibilities. This gives exciting new opportunities for fundamental studies as well as applications.

Therefore in this thesis I would like to give a demonstration of the behaviour of such a CSL based on a VCSEL with frequency selective feedback provided by a volume Bragg grating (VBG). This previous success of a CSL based on a VCSEL with feedback from a diffraction grating [118, 119, 127] showed that such systems could sustain CS, or rather laser cavity solitons (LCS) however also suffered from some restrictions, primarily its large size and the asymmetry of the feedback. Exchanging the diffraction grating for a VBG was thus proposed as a prospect as it seems to offer several benefits. Miniaturisation is the primary benefit, since the frequency selectivity would not be limited by the cavity geometry, as in the diffraction grating case. This not only allows compact setups to be produced but is also believed to be conducive to pulsed operation, opening the door to 3D localisation and pulse trains on demand. In addition the VBG has essentially isotropic feedback allowing the LCS to choose their own polarisation. Finally the narrower feedback bandwidth possible should allow a greater contrast between patterns and LCS, producing a larger range of parameters where only LCS should exist. The results which this new CSL produce shall be shown in this thesis.

I will first give an overview of some background topics such as semiconductor lasers and dissipative soliton fundamentals in chapter 2. I will then go on to describe the properties of the devices and equipment used in the experiment followed by detailed experimental procedure in chapter 3.

The basic properties of the behaviour of the system at threshold will then be presented and the structures which are seen will be proved to be cavity solitons in chapter 4. After these basic properties are found, I will investigate the hypothesis that this system should have extra degrees of freedom over previous realisations, and will explore the frequency in chapter 4 then phase and polarisation properties of the LCS in chapter 5.

I will then explore the temporal properties of the LCS in chapter 6, investigating whether the relatively short cavity length promotes self-pulsing. At this time I will also investigate in detail the switching properties of the LCS, with a

detailed investigation of switching parameters as well as the temporal dynamics occurring at switch-on threshold.

As will be seen, the majority of the properties of the LCS in this system are linked to a spatial variation of cavity parameters. Thus I will demonstrate methods to detect this variation or 'disorder' and then show the first demonstration to compensate for this disorder in a semiconductor system in chapter 7. This method will then be demonstrated and the benefits and restrictions of such a system will be revealed.

I shall then conclude the thesis, with an optimistic view of the progress made towards a viable CSL for applications and fundamental studies.

Chapter 2

Background

2.1 Semiconductor Lasers

With the advent of semiconductors it became possible to create extremely compact new laser designs. The basis of most semiconductor devices is the p-n junction. A semiconductor material is one which has an electrical conductivity which is between an insulator and a conductor. This conductance may be altered by adding impurities or acceptors to the semiconductor. If impurities, called donors, are added then the semiconductor has more electrons than a natural sample, and conversely if acceptors are added, the semiconductor has fewer electrons, or more 'holes'. These are referred to as p-type doping and n-type doping, and when both types are placed next to each other, it forms a p-n junction.

The Fermi energy levels in p-type and n-type semiconductors are different and when placed together in a junction the Fermi energy has to be continuous and thus causes the bands to bend in a small region at the interface. This region is the depletion region since all donors and acceptors in this region recombine. The depletion region causes the electrons next to it to feel an effective potential or barrier, i.e. they cannot pass through it without a 'push' and this stops further recombination. If however the junction is electrically biased in the correct direction such that the electrons are pushed across the barrier and the holes are dragged beneath it, they can recombine in a small region. Recombination produces spontaneous emission with photon energies corresponding to the bandgap

energy of the semiconductor [79].

The simple p-n junction is non-optimal however and while able to emit light (LED) this is not yet a laser. To achieve lasing threshold in such a configuration requires extremely high currents and low temperatures. Therefore various methods of increasing electron-hole recombination were investigated. This lead to the development of the double-heterostructure which is formed by sandwiching a smaller bandgap material such as GaAs between two larger bandgap materials such as Ga_{1-x} giving a top-hat like refractive index profile which guides the light in a similar situation to light guided in a fibre [27]. This allows greater population inversion by confining the carriers and also the optical mode, enabling the first lasing at room temperature and greatly lowering the threshold. This design is still sub-optimal and all modern semiconductor lasers contain quantum wells (QW) as the gain region.

The quantum well is an extension of the principle which lead to the development of the double heterostructure. If the layers are made thinner, so thin that their thickness is less than the De Broglie wavelength of the carriers then quantum effects begin to manifest. In such a potential well, a quantum well, the carriers are confined to discrete sub-levels (in one direction) resulting in a hard band-edge the physical result of which is that the laser requires less electron-hole pairs to achieve threshold, resulting in higher gain. Due to the more efficient nature of the QW, they are used in essentially all modern semiconductor lasers, including modern edge-emitting lasers (EELs).

The key mechanism in a laser is stimulated emission, in which a photon enters the device, interacts, and two photons with the same wavelength and phase are emitted. This is gain. It is therefore crucial to feed the spontaneously emitted photons back into gain region to stimulate further photons. This requires a cavity, simply mirrors around the gain region, as in any laser.

Semiconductor lasers are some microns to tens of microns in scale, making conventional mirrors inappropriate, however the relatively high refractive index of semiconductors means that the Fresnel reflection at an interface with air will be sufficient to create a cavity with sufficient gain. However if gain is an issue, other solutions are required.

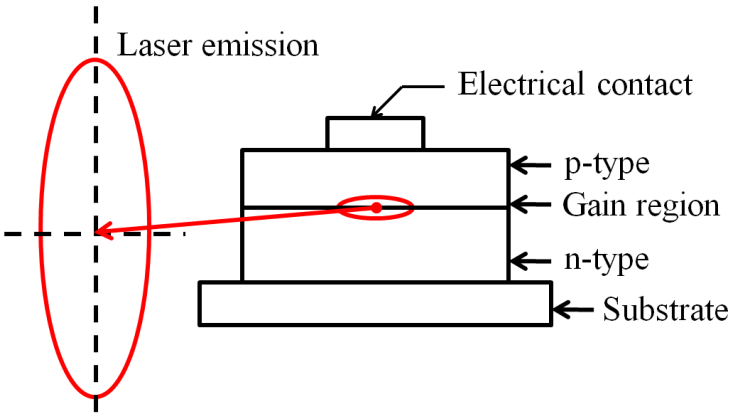

Figure 2.1: Schematic diagram of an edge emitting laser

The emission wavelength of such a laser is dictated by the bandgap energy of the semiconductor. This imposes a restriction on the possible wavelengths which may be achieved by semiconductor lasers of similar composition however a broad range of wavelengths may be achieved by altering the composition of the devices. A further restriction is imposed since the separation of the atoms in the material must be appropriately matched such that the materials will bond [100]. There are however semiconductor materials which have similar lattice constants which have bandgap energy differences in the infra-red region of the electromagnetic spectrum. This group of 'III-V' semiconductors include GaAs, AlAs and InAs as well as the ternary compounds of AlGaAs, InGaAs and InGaP. These have been used enormously successfully to create semiconductor lasers between 780 nm and 1.1 μm [65]. Progress has also been made with III-V semiconductors to extend the possible wavelengths down towards visible light and InP has been used to extend the range up to 1.3 μm and 1.55 μm which are now the industry standard for telecommunications. The advent of quantum dots [18, 116] has also allowed these telecommunication standard wavelengths to be reached using GaAs rather than InP, allowing better integration with the already established GaAs technologies.

2.1.1 Edge Emitting Lasers

The first semiconductor laser design to become popular was the so called edge emitting laser (EEL). The structure of this design is shown schematically in Fig. 2.1. Layers of n-type semiconductor are grown onto a substrate followed by the gain region and then capped by the p-type semiconductor and an electrical contact for pumping. The simplest possible emitter may be possible with a simple p-n junction however as stated above, modern semiconductor lasers all use quantum wells as the gain region due to the much improved gain over p-n junctions and double-heterostructure arrangements.

The mirrors are formed by cleaving or etching on the front and back to create facets which reflect the light inside via a Fresnel reflection at the interface with air or alternatively coated with either a highly reflecting coating or anti-reflecting coating allowing variable reflection coefficients. If the gain is great enough this cavity can support lasing. The main benefit of this design is that to increase gain, the dimensions of the gain region can simply be increased, i.e. increasing the cavity size in the longitudinal dimension. This does not come without cost, as increasing this dimension will also induce more longitudinal modes, however since the laser is multiple longitudinal mode already, this is acceptable in most cases. Increasing the transverse dimension of the gain region is also possible however this comes with a larger cost, exciting higher order transverse modes which would degrade the already asymmetric beam shape.

The main disadvantage with this design is that there is a large disparity between the lateral (perpendicular to the emission axis and along the growth axis) and transverse (perpendicular to the growth axis and to the emission direction) dimensions of the gain region, and hence laser output. Since the gain region is necessarily thin due to physical restraints, and wide in order to increase gain, the laser output is elliptical in both near and far fields (i.e. elliptical in shape and divergence) with typical ellipticity of between 2:1 and 5:1 major to minor axis.

This becomes a problem when trying to incorporate EELs into interconnected networks, which their small size makes them otherwise ideal for. With the advent of optically connected networks via fibre optic cables, the optimum coupling

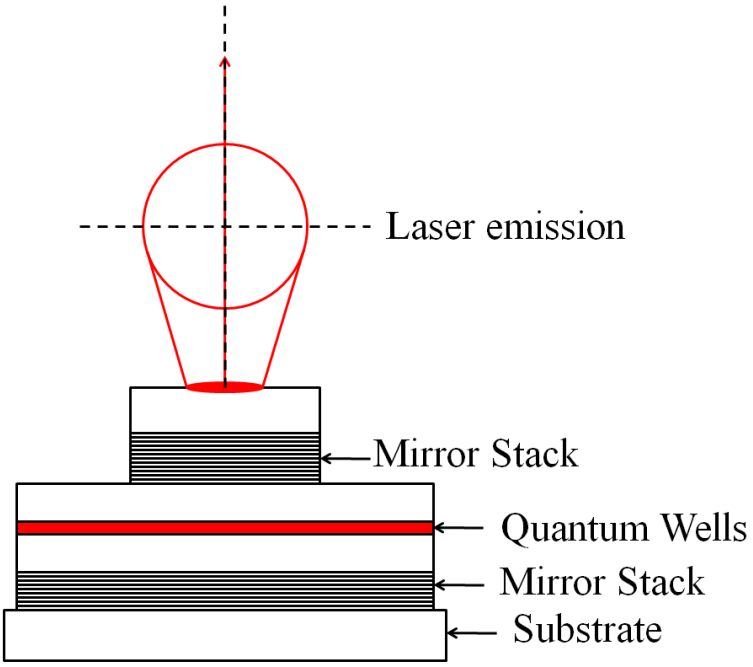

Figure 2.2: Schematic diagram of VCSEL structure

to such fibres is critical. Fibres have circular cross sections and the coupling efficiency is therefore limited by how circular the incoming beam is.

2.1.2 VCSELs

A combination of fibre coupling considerations, on-wafer processing demands and scientific curiosity lead to the invention of the vertical cavity surface emitting laser (VCSEL). In this configuration the cavity would be, as the name suggests, placed vertically (along the growth axis) within the semiconductor and therefore the emission shape can be chosen almost arbitrarily by selecting the shape for the aperture. The schematic design of such a VCSEL is shown in Fig. 2.2.

The VCSEL has several advantages over previously designed EELs. Their vertical emission means that the devices can be tested and processed while still on the wafer in which they are grown, whereas EELs require cleaving (i.e. cut off from the wafer) and processing to test their operation. In addition the output beam profile can be chosen almost arbitrarily by shaping the output aperture, with

the obvious advantage that symmetric output beams are possible. Furthermore a VCSEL can be designed to be is intrinsically very small with only a 1 λ long cavity producing single longitudinal mode.

However it should be noted that the gain cannot be increased by simply adjusting the dimensions of the gain region. The transverse dimensions (perpendicular to the emission axis) are fixed since increasing the transverse dimension would lead to unwanted transverse modes, leading to degraded beam shape quality. If the cavity length is increased to achieve more gain, multiple longitudinal modes would lase, negating one of the key advantages which VCSELs provide, their single mode operation. There are also manufacturing considerations to take into account when increasing the cavity length; due to the cavity running along the growth direction, the manufacturing time scales directly with the cavity length which is a significant disadvantage. Therefore in a typical engineering design the vertical cavity length is fixed at 1 λ to maintain single mode operation and hence the size of the gain region is also fixed in the vertical dimension.

Due to the small dimension of the gain region, the gain has to be maximised, and this is achieved by using quantum wells. Multiple quantum wells are placed at the anti-nodes of the resonant standing wave created in the 1 λ cavity. The quantum wells are separated by cladding layers and are isolated from the cavity limits by layers of cladding.

Even with the relatively high gain of the QWs the Fresnel reflections at the top and bottom of the device are insufficient to support lasing. Distributed Bragg reflectors (DBR) are used to create the laser cavity. These consist of $\lambda/4$ thick layers of alternating high and low index material (GaAs and AlAs for 980 nm devices) the reflections from which constructively interfere to produce very high reflection coefficients, typically $>$ 99.99% bottom mirror and $>$ 99% outcoupling mirror.

The high Q cavity created by the DBRs creates a narrow cavity resonance, which for optimum VCSEL operation should have its peak at the same wavelength as the gain curve. There is a complication however, since when the VCSEL is operating, the current heats the entire structure via Joule heating and expands the cavity, which in turn shifts the cavity resonance. The temperature increase also shifts the gain curve peak, but at a greater rate. This consideration means

that VCSELs are designed with cavity resonance peak and gain peak offset when the laser is not operational. They are offset in such a way that the two peaks shift and overlap for operational temperatures.

The electrical injection into VCSELs has most recently and most successfully been achieved by the growth of oxide apertures into the VCSEL structure. This oxide aperture provides current confinement but more importantly creates a sharp refractive index jump within the device which guides the optical mode, similar to the optical guiding in a double heterostructure or an optical fibre. The optimum mode shape is circular with typical transverse diameter around 5 μm to support only a single transverse mode. Oxide confinement of the VCSEL mode has proved to have many advantages over previous methods such as ion implantation or etched air post design and has set records for lowest threshold current of $<$10 μA, lowest threshold voltage of $<$1.33 V, highest power conversion efficiency of $>$50% and small signal modulation bandwidth of $>$20 GHz [60].

The benefits of high beam quality make VCSELs useful for applications which require fibre coupling, such as optical interconnects or optical networking. They also have the advantage that due to their vertical emission, they may be tested at a very early stage of production, compared to an EEL which requires several extra manufacturing steps such as cleaving, before they may be tested. The vertical geometry also makes them ideal for making laser arrays.

Single mode VCSELs are however limited to output powers of a few milliwatts, and as mentioned previously attempts to achieve higher power by increasing the transverse aperture size result in unwanted transverse modes, degrading beam quality. The transverse modes in so called 'broad-area VCSELs' can become very complex, with increasing complexity with aperture size however they also show self-organisation behaviour under certain circumstances [54], and this aspect of VCSELs will be the focus of this thesis.

2.2 Solitons

Soliton is the term given to wave which travels without changing shape, even in the presence of diffraction or diffusion. The first soliton or solitary wave was observed by John Scott Russel in 1834 when observing a boat in a canal [99]. The

boat was suddenly brought to a halt and the water collected at the front of the boat for a moment before moving off as a foot high wave. He followed the wave along the canal and observed that the wave retained it's shape for some miles before losing sight of it in a winding section. This is an excellent example of the fundamentals of solitons. At that time Russel called this phenomena a 'wave of translation'.

2.2.1 Conservative Solitons

More recently the term soliton was used to describe nonlinear localised solutions of exactly solvable models, such as the nonlinear Schrödinger equation. This was a purely mathematical concept however such solutions also existed in several physical systems. This lead to the discovery of a set of solitons referred to as 'conservative solitons' which refers to the idea that the energy of the soliton is conserved, or rather that the peak power is inversely related to the peak width such that a change of peak power due to dissipation can be compensated by an increase in width. The soliton changes shape then, but only on time and length scales which are greater than the characteristic diffusion or diffraction length if dissipation is low. Conservative solitons were demonstrated experimentally [110, 115] in several propagation systems where the losses were so low as to effectively stay in the conservative regime.

If the conservative limit no longer applies due to high losses then a soliton cannot exist for very long in propagation. However if this soliton is pumped such that the pumping energy accounts for the losses then the soliton can become stable over long ranges. These so-called 'dissipative solitons' have their own rich behaviour, so much so that it may be considered it's own area of research.

In optics the most common solitons arise when nonlinearity is used to counteract diffraction (spatial soliton) or dispersion (temporal soliton). In the spatial case this can be understood as the balancing of two phenomena. Propagating light naturally diffracts (dashed line in Fig. 2.3a), that is the size of the beam expands, diverging as it travels. However if there are nonlinearities inside the system, a contribution of the third order nonlinearity produces the 'Kerr effect'. This effect simply gives the material an intensity dependent refractive index, and

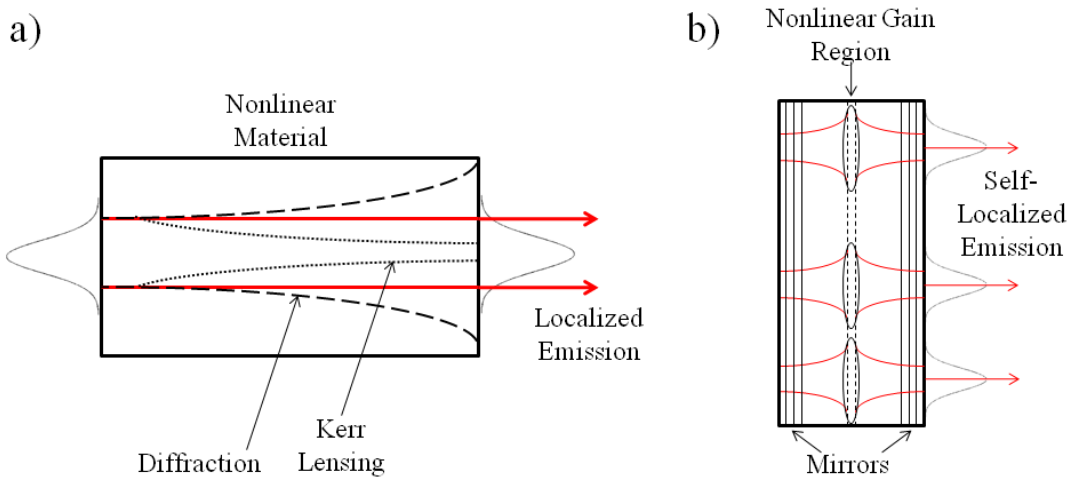

Figure 2.3: a) Sketch of diffraction, nonlinear lensing and soliton propagation in a nonlinear medium. b) Sketch of the stabilising mechanism of a cavity soliton.

so a Gaussian beam shape produces a Gaussian refractive index gradient and this gradient acts approximately like a lens, focussing the light (dotted line in Fig. 2.3a).

The spatially localised wave is thus supported when the natural diffraction of the beam is counteracted by the Kerr lens, the net effect of which would be that the beam would propagate inside the nonlinear medium without diverging or converging, i.e. it is spatially localised. A sketch of this effect is shown in Fig. 2.3. The dotted converging represents the effect of the Kerr lensing and the dashed diverging lens is the effect of the diffraction. The result is the red beam which neither diverges nor converges throughout the nonlinear medium and this is a spatial soliton.

2.2.2 Dissipative Optical Solitons

Compensating for diffraction is not the only consideration however, since in a real systems there are losses. The losses mean that any soliton would not be sustainable. Therefore in a non-conservative system formation and stabilisation also required a mechanism to counteract losses, energy injection, or in the case of a laser, gain. This balance of loss and gain gives these solitons their own set of behaviours and thus should be classified as dissipative solitons.

To access the nonlinear properties of a material high beam powers are necessary and thus it seems natural to place the nonlinear medium within a cavity. The cavity enhancement should increase intra-cavity power and under the correct circumstances, a spatially localised structure should resonate in the cavity. This is simply a dissipative soliton in a cavity, and it is referred to as a cavity soliton (CS) (Fig. 2.3b). If a planar-planar Fabry-Perot cavity is used to surround the nonlinear gain region then there are no stable Gaussian modes of this cavity. The CS can stabilise themselves however due to the nonlinearity present in the cavity. The cavity does not necessarily have to contain a nonlinearity everywhere to sustain a nonlinear mode however and this is the case shown in Fig. 2.3b. The nonlinear gain region acts like a lens between the two planar mirrors, creating a stable cavity, and creating self-localised lasing spots which retain their spatial profile after each round trip, i.e. a spatial cavity soliton. For a more detailed description and analysis refer to [6, 7, 37].

This self-localised lasing state is therefore not stabilised by boundary conditions such as mirrors or apertures, but by nonlinearities and should be able to exist anywhere in the transverse aperture of the laser. Many of these CS should also be able to co-exist within the same device and if not placed too close together should not be coupled to each other and are thus independent while also being highly parallel (many in a single system).

In addition to these properties CS are also bistable. Since CS form on a homogeneous background state, this background or 'off-state' is necessarily stable. For higher values of pumping parameter the background becomes unstable and spatially extended emission begins. Below this threshold for spatially extended emission there exists a region in which the CS can exist and crucially the background is still stable. The consequence of this is that in the CS region there are two possible states which are stable, one in which CS are present (on-state) and one in which no CS are present and only the background state is present (off-state) and this is bistability. Due to their independence each CS is bistable in its own right, meaning that each CS can be on or off independently of the others, which discerns the CS from a bistable pattern.

CS are particularly interesting for applications since if they can be realised in fast, compact media then they present themselves as candidates for optical

memories due to their high degree of parallelism, independence and bistability.

Research in cavity solitons seems to begin with the paper of Moloney et. al. [71, 76] where they investigate transverse effects in a ring cavity with optical bistability. They observe that if they increase the input pump intensity to a critical point, there was a transition to a spatial distribution of high intensity states surrounded by un-switched, low intensity states. This group of multiple intensity peaks present in the transverse plane were interpreted as a group of spatial solitons.

These groups of solitons were not independent however and only two states were possible, one in which all peaks were present and one in which no peaks were present. McDonald and Firth [69] then showed that it was possible to achieve independent structures by using a pump beam with a spatial modulation of intensity. Furthermore they show that it was even possible to switch these CS on and even off due to their intrinsically bistable nature and this opened up the possibility for optical memory applications.

The work of Rosanov [96, 97] in diffractive auto-solitons was one of the first to show 2D spatial solitons. The switching waves in systems with diffraction can cause two of these waves to lock, or one wave may bend so far that it locks with itself, becoming a stable island. These diffractive auto-solitons were also found in lasers and seem to be perhaps the first sighting of what would come to be known as the laser cavity soliton (LCS).

Experimental works involved driving liquid crystals inside a plano-planar cavity [62, 80] and there had already been experimental evidence for pattern formation and spatial structures in systems with sodium vapour with feedback [46].

2.3 Dissipative Solitons in Semiconductors

If these spatial dissipative solitons could be realised in a compact scheme, with fast intrinsic timescales then they may be useful tools for all-optical networking. Their suitability for networking would stem from their high degree of parallelism (many solitons can be supported by one device) and their independence, with the obvious application for optical memories. Previous schemes which use gases with nonlinearity or liquid crystals are either far too bulky, or have characteristic

timescales which are far too slow. The criteria for the ideal system are then a nonlinear system which supports bistability, has fast characteristic timescales and is compact, preferably μm to nm scale.

Semiconductor devices with a bistability inducing mechanism thus present themselves as a candidate for applications and study. They are compact, on the micron scale, they have quite fast intrinsic timescales on the order of ns and they have a nonlinear gain region. The weak relative nonlinearity of the gain can also be compensated for by a cavity. The semiconductor devices themselves do not have a mechanism to support bistability however, and there are two main approaches which emerge to achieve this. The first is the addition of an externally injected beam, the so-called 'holding beam' (HB), the second is the addition of an element to support bistability, primarily frequency selective feedback (FSF) or a saturable absorber (SA). Both the driven systems (HB reliant systems) and cavity soliton lasers (FSF or SA) will be discussed in the following sections.

2.3.1 Cavity Solitons in Driven Systems

The experimental journey towards creating CS in semiconductor systems was inspired by theoretical work on systems in which patterns are in competition with a homogeneous state [8, 21, 22, 23, 26, 30, 32, 37, 47, 61, 66, 72, 81]. Theoretical works predict a 'front' which separates the region in pump parameter where the homogeneous background state is stable and the region in which a patterned state is stable. These switching waves were found experimentally in [39] and were followed by the first experimental observations of CS, which were in semiconductor amplifiers, biased below threshold and injected with a spatially extended, ideally homogeneous external laser beam termed the holding beam (HB) [15].

The semiconductor device was an electrically injected broad-area VCSEL with an active region of bulk GaAs. The device had an unintended detuning gradient which results in the threshold for pattern formation varying in an almost linear way across the VCSEL. This resulted in the clear emergence of a front, on the left of the device there was a region of pattern formation, but on the right there is a region devoid of pattern, with only HB present. The two are separated by a high

intensity line which is interpreted as the front and in accordance with prediction, the front moves when varying the pump parameter.

The theoretical expectation is that CS should be able to exist in the unpatterned region close to the front. The seminal experiment of [15] showed that this was indeed true and used an external local writing beam (WB) derived from the HB to switch on localised structures within this region.

The experiments then deviated from the predicted theory when the spontaneous formation of CS was seen in a broad-area VCSEL amplifier with HB [14]. In an ideal system this should not occur, as the background state is stable until the point at which spatially extended states become stable resulting in a transition from background to spatially extended lasing for a simple pump increase. The formation of CS in such a system requires that the system is biased in the parameter region which supports CS, followed by the injection of a local perturbation, such that the system switches from the stable background state, to the stable self-organised state. In optical systems this perturbation is applied by an external laser beam with size similar to that of a CS. Contrary to this idealised view, the CS were seen to appear by simply increasing the power in the HB.

The explanation nucleated from the previous examples which shows that material gradients can have an impact on CS formation. Work in [31, 48, 52, 111] shows that self-organised patterns have rotational and more importantly translational neutral modes. This essentially means that translation is a neutral mode for a CS (being a self-organised pattern) the net effect of which is that the CS should move under any gradient, and move so fast as to be missed by the time-averaged detectors used in most experiments.

Unwanted gradients are always present in experiments in the form of unavoidable manufacturing defects and would cause the CS to drift to a boundary and be annihilated immediately after formation. It can thus be conjectured that these defects have some local minima which act as traps for the CS. If these traps were deep enough, they would pin the CS in place, stabilising them in position and avoiding annihilation with the boundary. It follows then that these traps would impose a spatial distribution of cavity parameters leading to a threshold distribution causing those parts of the laser with the deepest traps to cross the threshold

for pattern formation before the rest of the device, and if the trap is only large enough to support one piece of the pattern then a CS is formed.

The aforementioned optical amplifier with HB system was also capable of writing and erasing multiple CS within the device. Writing was performed by picking a part of the HB, demagnifying it and injecting it locally upon the VCSEL. Erasure is performed by the same method but the WB is imposed with the opposite phase which leads the destructive interference of the CS and WB, switching off the CS. This is one of the key advantages of the HB method, in that the CS are locked to the HB to a great extent and thus a phase reference is available, giving a reliable method of erasure.

This locking of parameters is also one of the constraints of the system however, as the frequency, phase and polarisation are all locked to that of the injection. Furthermore, such systems are not well suited to monolithic integration, which would be the end goal and essential for applications.

2.3.2 Cavity Soliton Lasers

Until now only driven bistable systems have been discussed. Such systems consist of a nonlinear cavity which is driven by a beam of high spatial and temporal coherence, the HB. This reliance on the HB is a disadvantage for applications and schemes which draw upon cheap and incoherent energy sources such as electrical pumping are sought after. Thus experiments towards creating a cavity soliton laser were commenced. In such a system, the HB would be removed, and bistability would be provided by feedback or saturable absorption alone, making monolithic integration possible and perhaps the freedom of CS parameters would lead to some interesting effects.

Such a system would behave as a laser, since all emission would be self-sustained. A self-sustained device capable of supporting cavity solitons would be termed a cavity soliton laser (CSL). Furthermore to the advantage of cheap, non-constraining pump source a CSL should also offer some unique aspects which are interesting not only for potential applications but also for fundamental studies.

As indicated, in systems employing a HB the frequency, phase and polarisation properties of CS are determined by and locked to the properties of the HB. In contrast such properties are not tied to any external pump source in a CSL, and as in any laser each laser cavity soliton (LCS) should be able to choose its own phase since LCS creation should arise from a spontaneous symmetry breaking. Given correct feedback parameters the frequency and polarisation properties of LCS should have more freedom due to the lack of external influences. External cavities also allow for the possibility to lase on several external modes, which may lead to mode-beating or mode-locking behaviour providing potential for pulsed LCS, or 3D solitons (2 spatial dimensions + time). Furthermore, the independence of LCS should allow every LCS to select all of these operating parameters independently, giving potential for new fundamental studies while also providing possibilities for applications. The phase freedom allows relative phase differences between different LCS which would allow experimental investigation into the theoretical prediction that such phase differences affect LCS dynamics and interaction properties [98].

The freedom for LCS to choose frequency and phase also opens the door to studies concentrating on frequency and phase locking which is known to be typical for lasers which can operate on frequencies close to one another [57, 58] and more generally frequency and phase locking in nonlinear oscillators [91].

The first proposed scheme for a cavity soliton laser was based on a laser with optical injection which is a scheme similar to that discussed before, and detailed in [15] but now biased above laser threshold. This system was demonstrated in [51]. Since it has been stated that the benefits of a laser system are that there is no strong pinning to the HB, it is not surprising that in this realisation, which contains a HB, the 'laser' aspect of this system only manifests itself in one distinct difference from the amplifier case in [15]. This was that the background on which the LCS exist might be temporally varying. This possibility arises due to the background not being strictly constrained to a phase-locked state with the injection, allowing oscillations due to beating between laser and injection. These oscillations were later experimentally demonstrated indirectly via spectral measurements [51]. Details can be found in the review [67].

An experimental system which does not rely on optical injection was thus sought after. A VCSEL alone is not sufficient to provide LCS, since the transition to lasing is continuous. Formation of LCS requires a mechanism to stabilise bistability i.e. stabilise the background state in the lasing region or stabilise the lasing state in a background region. One method is to employ saturable absorption which stabilises the background state due to the difference in saturable and non-saturable losses [96]. A second method of stabilising bistability is to use frequency selective feedback. Since it has been confirmed that optical injection which is detuned to the VCSEL resonance is capable to provide bistability, it seems interesting to ask whether the VCSEL can provide it's own optical injection, i.e. feedback. If a feedback element is chosen such that it only reflects a narrow wavelength band of the VCSEL emission (this is frequency selective feedback) then there can exist a detuning between this wavelength band (referred to as the grating frequency) and the VCSEL resonance and this system can once again support bistability [77].

The bistable nature arises because there are two states which may be stable simultaneously, one state with low amplitude and thus high carrier density, and a second state in which the intensity is high and the carrier density is low. These two states are both stable and thus compete with each other in a parameter region just below the onset of spatially extended lasing. Due to the stability of the background state, excitation to the high intensity state requires a 'hard' perturbation. If the system is biased in the bistable region, such a hard perturbation increases locally the intensity, lowering carrier density, and through phase-amplitude coupling increase the refractive index which red shifts the VCSEL cavity resonance. This is then shifting the VCSEL cavity resonance closer to the grating frequency which increases further this effect and cascades towards the high intensity state. A discussion in small VCSELs is given in [77, 78].

The first demonstration of a cavity soliton laser based on a VCSEL with frequency selective feedback was realised using a broad-area VCSEL with feedback from a diffraction grating [118, 119, 127]. The VCSEL was coupled to the diffraction grating via a self-imaging cavity in a Littrow configuration. The frequency selection arises due to the diffraction grating separating the different wavelengths spatially, such that if a wavelength is detuned to the Littrow wavelength then it

is not retro-reflected, but gains some angle to the feedback and if this angle is too large then it will lie outside the acceptance angle of the VCSEL and will not resonate in the external cavity.

The first appearance of a laser cavity soliton in this system was discovered when the grating frequency was set to be red detuned to the VCSEL cavity resonance. Upon increasing the current a small increase in intensity is observed closely followed by a sharp transition in emitted intensity and upon decreasing the current again this high intensity state is seen to remain stable for currents at which the system was previously in the low intensity state and for even lower currents where only the background state was stable previously. This is bistability. The spatial distribution of lasing emission associated with this high intensity transition is monitored in a CCD camera and is observed to be localised to a single spot of width of the order 10 μm FWHM (whole device aperture 200 μm diameter). The spot emits on axis and has an optical linewidth of 10 MHz and thus represents a small, local, coherent emitter, or micro-laser.

Several of these spots appear spontaneously for increasing current at different thresholds but their respective thresholds and positions are constant for repeated measurements and this is attributed to the 'traps' discussed earlier. Since several spots appear in the aperture of the device simultaneously it is possible to test their independence. To ascertain independence the VCSEL is biased at a current which is known to support several spots in the low intensity off state and high intensity on state simultaneously and this current is approached from the low current side such that the spots are off. A local beam with transverse size close to that of a spot is then externally injected onto the VCSEL at the location where one spot is known to appear. This results in the switching of the spot from the off state to the on state, which remains on even when the injected laser is removed. This is then repeated for a second spot, still at the same current and this second spot can be switched on without affecting the state of the first spot. The spots are then switched off again without affecting each other, demonstrating their independence.

These previous properties of locality, bistability and independence combined with findings that the spots have the ability to move position (though with limited range) and are all of almost equal size give strong indications that these structures

are a product of nonlinearities rather than boundary conditions. This is positive confirmation that these spots are cavity solitons, or rather, laser cavity solitons.

Though successful in creating LCS, there are several restrictions imposed by this realisation. The overall cavity length used was 76 cm, ideal for exploratory proof of concept measurements but with the goal of ultimately creating a monolithic device miniaturisation of the setup is important. The frequency selectivity of this setup arises from geometrical constraints, leading to a trade-off between cavity length and frequency selectivity such that miniaturisation would compromise the creation of LCS. The second related restriction is that the frequency selective feedback is rather broad-band, leading to the coexistence of LCS and extended states, even at low currents which is disadvantageous for applications.

Another issue is the non-isotropic nature of the grating. Due to the orientation of the lines on a diffraction grating and the angle at which it is required to be placed with respect to the beam several effects occur. The first is that there is a preferential lasing on one side, due to the wavefront tilt induced by the diffraction grating. The directionality of the lines on the grating also leads to only one polarisation propagating in the external cavity, removing the polarisation freedom which should be inherent to cavity soliton lasers.

When this project was begun, another solution was sought with the intent of promoting miniaturisation and narrowing feedback bandwidth. The solution which was proposed was the use of a volume Bragg grating (VBG) as the feedback element. Since the VBG feedback bandwidth is dependent on the number of $\lambda/4$ layers, miniaturisation is possible, even down to the monolithic scale. The frequency selectivity can also be specified during manufacture and allows far narrower bandwidth which should increase the LCS to extended state contrast. The isotropic nature of the feedback also removes any strong preference for a certain polarisation, allowing the LCS to potentially form their own polarisation based purely on laser parameters.

This thesis will present results on this system of a cavity soliton laser based on a broad-area VCSEL with feedback from a volume Bragg grating and in particular hopes to show that this system can support LCS, and that these display fast temporal dynamics and show the freedom of frequency, phase and polarisation not shown in previous schemes.

Chapter 3

Basic Properties of Experimental Equipment and Theoretical Model

3.1 VCSEL Parameters

The VCSELs which were used throughout the project were fabricated by Ulm Photonics. They are large aperture devices fabricated specifically for the purpose of creating cavity solitons. Standard VCSELs are designed with a transverse aperture size such that it only supports a single, or low number of, transverse modes, which is clearly advantageous for applications which require high quality beam shapes, however a single mode device has an aperture diameter on the scale of some microns, too small to support multiple CS (which have typical radii of 5 μm). For this reason large aperture devices were created, enabling multiple CS to exist within the same aperture simultaneously.

These devices have emission wavelengths around 980 nm and circular transverse apertures which are 200 μm in diameter. The composition of the VCSEL layers are shown in Fig. 3.1. The gain region is composed of three $In_{0.2}Ga_{0.8}As$ quantum wells with two GaAs barrier regions separating them. The active region is then completed by sandwiching the gain region between two 48.5 nm thick GaAs cladding layers. Below the active region is a 150 nm thick $Al_{0.5}Ga_{0.5}As$

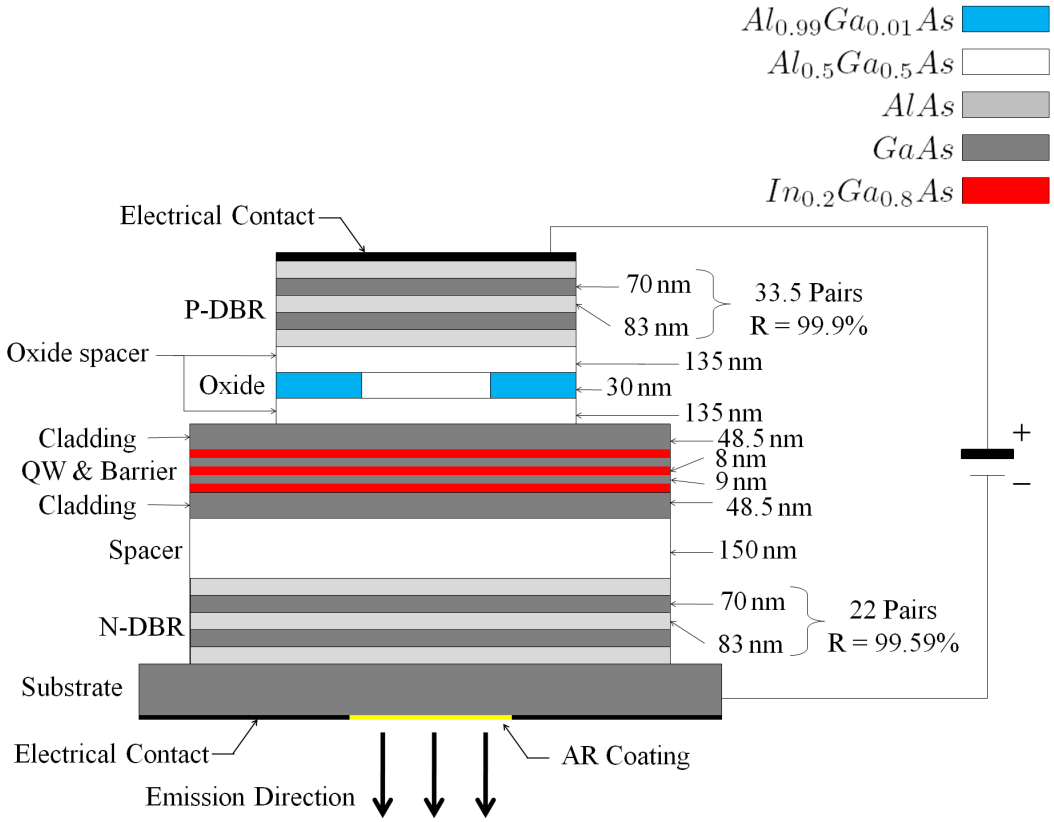

Figure 3.1: VCSEL structure diagram

spacer layer followed by the bottom n-type DBR, composed of 22 pairs of alternating AlAs and GaAs layers, giving a reflectivity of 99.59%. Above the active region there is a 30 nm thick layer of $Al_{0.99}Ga_{0.01}As$ oxide which provides both optical and electrical confinement. Surrounding this oxide layer are two 135 nm thick $Al_{0.5}Ga_{0.5}As$ spacer layers. Above this is the p-type DBR which is composed of 33.5 pairs of alternating AlAs and GaAs layers, giving a reflectivity of 99.99%. On the very top, an electrical contact composed of TiPtAu covers the entire surface. The layers are grown onto a GaAs substrate which is then thinned to around 200 μm and the output window anti-reflection coated (Fig. 3.2 shows the electrical contact surrounding the AR coated circular output window in a 106 μm aperture device).

The optical confinement is provided by the oxide aperture. This is achieved by oxidising a layer of $Al_{0.99}Ga_{0.01}As$ just next to the cladding/quantum well region.

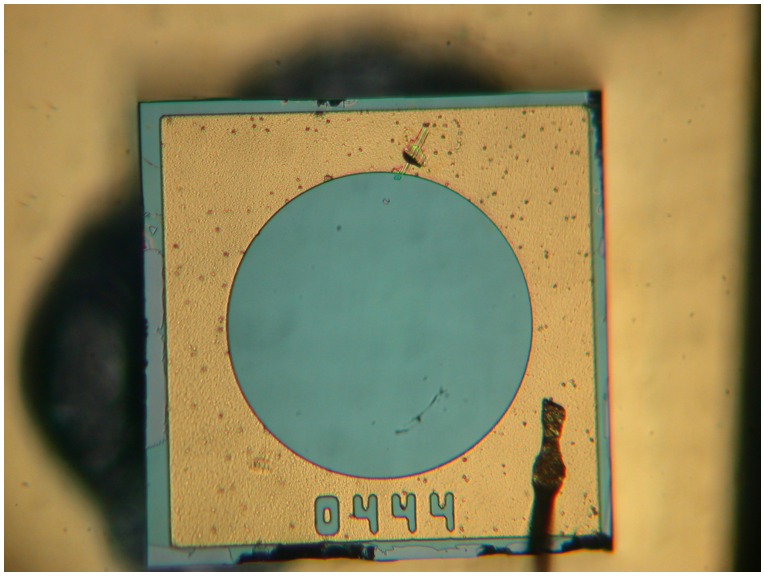

Figure 3.2: Microscope image of a VCSEL with 106 μm circular aperture.

The whole layer is oxidised except for a 200 μm circle in the centre of the device. The oxide layer provides a sharp refractive index jump creating a strong optical confinement which dictates the emission shape, confining it within the circular aperture.

The oxide has the further advantage that it does not conduct electricity, therefore when the current is injected via an electrical contact attached to the top of the device, the carriers travel through the top mirror and are focussed or funneled into the gain region, rather than diffusing all throughout the device.

There is one major deviation from a standard VCSEL, the devices are 'bottom emitters', i.e. they emit the light through the bottom mirror rather than the conventional top emission. This is achieved by growing the devices normally except for the number of layers in each of the DBRs. Since the device will emit from the bottom, the bottom mirror has slightly lower reflectivity than the top mirror, opposite to a standard top emitter. The primary advantage of this bottom-emitting layout is that it increases the homogeneity of the current and carrier distributions, meaning that the variation of cavity parameters across the aperture is reduced, which is a major concern when manufacturing large-area devices and will prove crucial in the performance of these devices for creating CS.

Once growth is complete the devices must be mounted to a heat sink, the standard would be to place the substrate on to the heat sink however this has the issue that the heat dissipation must pass through the thick (hundreds of microns) substrate, which limits thermal dissipation of the device. In the case of a bottom emitting device, the heat sink is attached to the top DBR, minimising the distance between the laser cavity and the heatsink. This is advantageous in a large aperture device since the larger aperture means more heat, and this must be dealt with. The laser output then passes through the bottom DBR and out through the transparent substrate.

Several different varieties of large-area devices were available at the outset of this project. The first question to tackle is which device should be used. Devices with aperture sizes ranging from 100 μm to 300 μm were available and tested. The larger aperture devices are desirable since they can potentially sustain more CS simultaneously however with larger diameters may come problems, increased heat and larger current crowding effects being prevalent. The devices also came in two different heat sinking configurations, TO-46 cans and TO-200 submounts. The devices were tested for their ability to sustain CS and their general lasing performance. Performance from VCSEL to VCSEL is quite varied and the device which will be used in most realisations is a 200 μm circular aperture VCSEL device mounted on a TO-200 sub-mount. Until otherwise noted all specs and data will refer to this device.

In spite of their large diameter, these devices are still capable of lasing. Fig. 3.3 illustrates the lasing emission pattern for the selected device at a temperature of 16°C. The spontaneous emission of these devices is essentially homogeneous over the entire circular aperture of the device for values below threshold, however close to threshold the spontaneous emission increases in intensity close to the boundary due to current crowding (Fig. 3.3a). When the threshold is crossed at approximately 405 mA the VCSEL begins to lase on a 'whispering gallery' mode around the outside of the device (Fig. 3.3b) and is manifested as a ring with a substructure of fringes which run perpendicular to the boundary. This mode has the lowest threshold due to the current crowding around the boundary which boosts gain. The current crowding is a common feature in large-area devices and is

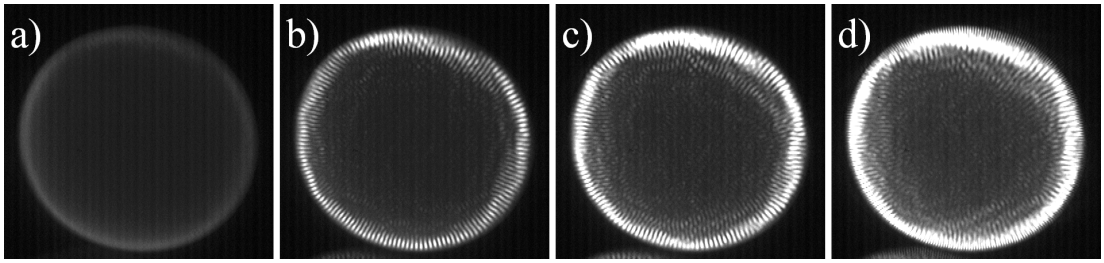

Figure 3.3: Near field emission pattern for a 200 μm diameter aperture VCSEL with current a) 400 mA, b) 450 mA, c) 500 mA, d) 600 mA

a consequence of the limitations of electrical injection at the boundaries. Bottom-emitting devices such as these were found to suffer less from the detrimental effects of current crowding compared to top emitters [73]. The whispering gallery mode continues to lase until 600 mA, only changing the fine structure of the fringes (Fig. 3.3c-d) possibly related to new modes lasing on different frequencies. Higher currents were not probed for fear of damaging the VCSEL. The behaviour of large-area VCSELs has been studied in detail previously and for further details on the free-running properties of large-area VCSELs refer to [103, 104, 105].

The emission wavelength at room temperature of one of these VCSELs is typically 975 nm however this may be tuned by altering the temperature of the device. This can be done directly by altering the heatsink temperature of the VCSEL, or indirectly through tuning the current supplied to the VCSEL. In the case of directly heating the heatsink, the cavity resonance shifts at 0.055 nm/K and is due to the expansion of the cavity, which directly increases the optical path length inside the VCSEL, coupled with the change in refractive index induced by increasing temperature.

Indirect heating via current occurs through the process of Joule heating, the phenomena whereby current passing through an ohmic conductor produces heat. Fig. 3.4 shows how the peak output wavelength changes with current. The shift is linear and the slope of the fitted line indicates that the shift is at a rate of 0.0035 nm/mA. These two rates lead to a Joule heating rate of 0.064 K/mA.

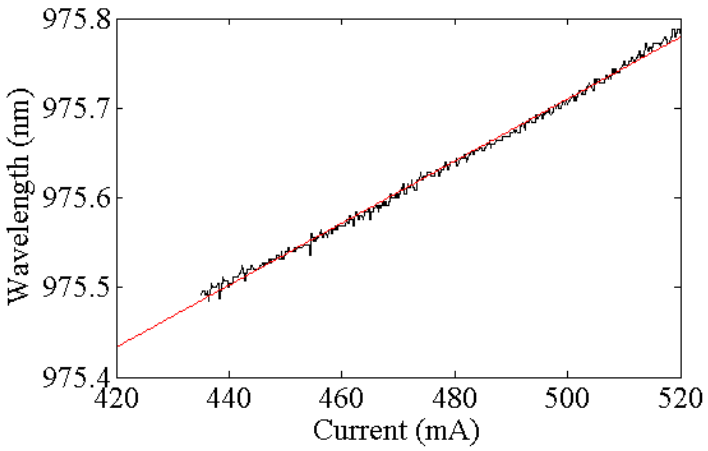

Figure 3.4: Peak wavelength shift with increasing current for the free running VCSEL at 16 °C. Black points are experimental data, taken every 0.1 mA, solid straight line is a numerical fit to the data.

3.2 Cavity and Feedback Parameters

3.2.1 Feedback Parameters

The frequency selective feedback element used is a volume Bragg grating (VBG). This is simply a glass cube with alternating high and low refractive index layers of $\lambda/4$ thickness. The number of layers determines the reflectivity and the thickness of each layer determines the position of the reflection peak. When light reaches each interface between high and low index layers, it causes a reflection and if the thickness of the layers is chosen to be $\lambda/4$ then each reflection constructively interferes to produce very high reflectivities. Since the grating relies on interference to produce reflection, only a narrow band of wavelengths experience this reflection, giving the VBG a very narrow reflection bandwidth; this is frequency selective feedback.

The VBG used was a custom specification grating manufactured by Optigrate [24, 82]. The material is crown glass and it has a size of $4 \times 5 \times 4.56$ mm. The grating is written into the glass using a UV laser with $\lambda/4$ wavelength where λ is the reflection wavelength. The grating is written with a wedge angle of 0.5 ° with respect to the front facet to avoid interference between the grating and facets. Even though this wedge is present, there were interferometric effects occurring,

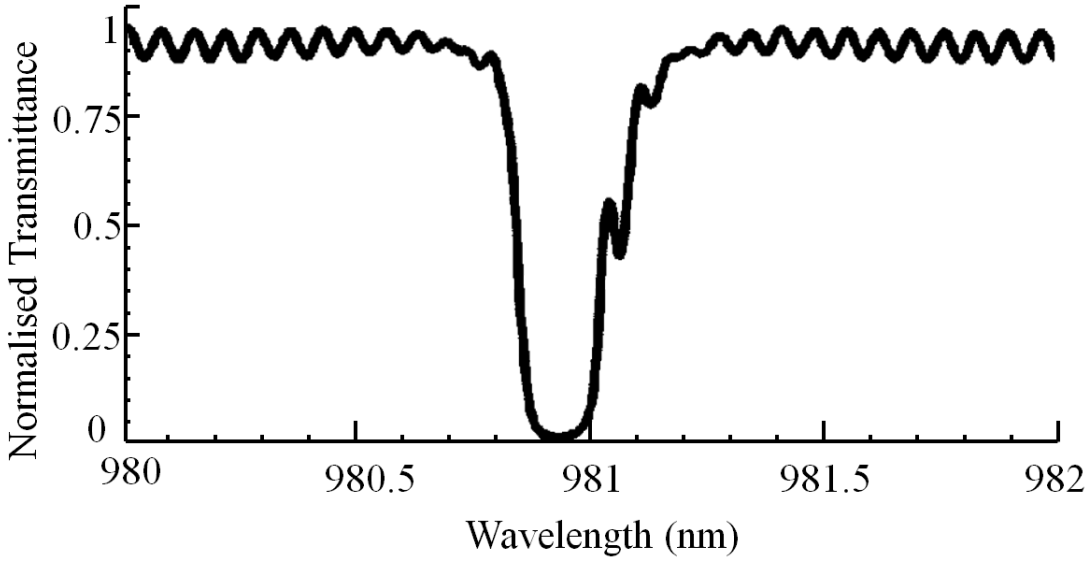

Figure 3.5: Reflection characteristics of the volume Bragg grating. Curve supplied by Optigrate [82].

the fringes of which could be turned by turning the VBG. The hypothesis was that there was still some interference between the grating and the facets, which lead to the VBG being sent for anti-reflection coating. This was successful in removing these interferometric effects.

The reflection characteristics can be seen in Fig. 3.5. The specifications state that the reflection peak is centred around 980.9 nm and has a width of 0.19 nm FWHM. The diffraction efficiency stated at peak centre is 99.1 %. In order to make sure that the data is self consistent, the peak of the VBG was measured by scanning the wavelength of a laser and measuring the transmission of the VBG. This experiment gave the central peak of the VBG to be 981.1 nm. Possible reasons for this discrepancy can be either temperature effects, i.e. the VBG expanded with temperature, shifting the central reflection peak to higher wavelengths, or it can be miscalibrated equipment, either on the part of Optigrate or in the equipment used to re-measure. Regardless, the value of 981.1 nm shall be used henceforth as the grating wavelength since the absolute wavelength is actually unimportant and only the relative detunings of each element in the system

is important and this value will ensure that all data is self-consistent. The same experiment was used to estimate the feedback bandwidth, which agrees with the stated value within experimental uncertainty. The reflectivity at the grating peak is not confirmed however, as the non-continuous tuning of the probe laser means that it is not possible to sit directly on the narrow grating reflection peak.

Correct alignment of the VBG is required to ensure optimum feedback parameters. To ensure accurate alignment the VCSEL current is increased such that with feedback the laser is lasing in an extended pattern over most of the aperture. For high currents the lasing emission forms a ring in far-field, corresponding to off-axis emission. This ring is sensitive to alignment of the VBG, with a slight tilt ruining the symmetry of the ring skewing it to one side. In this way it is possible to align the VBG such that the ring is maximally symmetric and this should be the alignment for which the VBG is as close to ideal as possible. Unless otherwise stated, the VBG is aligned according to this procedure.

3.2.2 External Cavity Parameters

The creation of LCS requires some mechanism to support bistability. In this realisation frequency selective feedback in the form of a VBG is used as this mechanism, and this must be coupled to the VCSEL via an external cavity. The constraints placed on this cavity are that it should image each point on the VCSEL to the same spatial position after each round trip, since this is a requirement to sustain spatial localisation. To satisfy this criteria, a self-imaging cavity is used in the form of a telescope (See Fig. 3.6).

There are two distinct external cavity setups, these will be referred to as the 'long cavity' and the 'short cavity'. The short cavity is believed to encourage self-pulsing, however is too short to allow extra intra-cavity elements such as a half wave-plate, and thus when extra elements are required, the longer cavity is used.

In both cavities the VCSEL emission is collimated by an 8 mm focal length plano-convex aspheric lens (Thorlabs C240TM-B). The lens used to focus the light onto the VBG differs between the short and long cavities however, in the short cavity a 1 inch aperture, 30 mm focal length plano-convex lens (Thorlabs

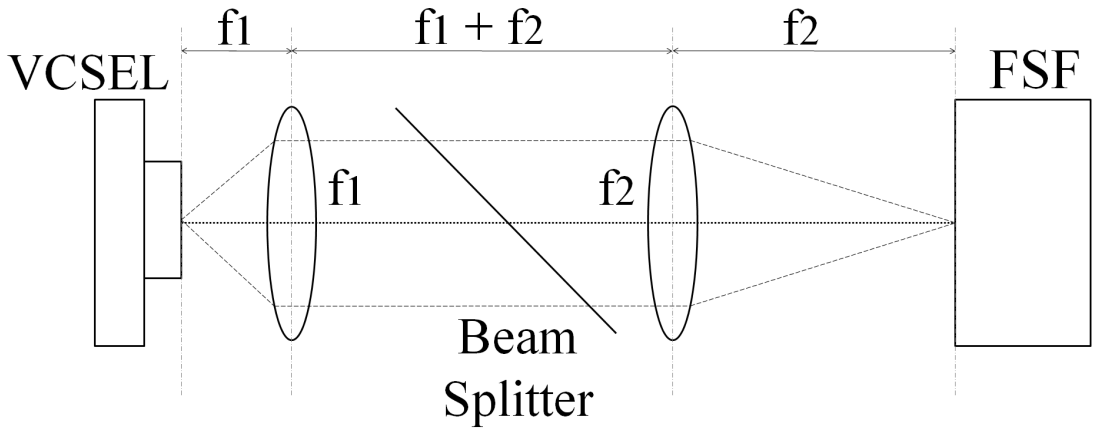

Figure 3.6: Schematic diagram of a self imaging cavity coupling a VCSEL to frequency selective feedback (FSF). f_1 and f_2 are the focal lengths of the lenses.

LA1805-B) was used, and in the long cavity a 1 inch aperture, 50 mm focal length plano convex lens (Thorlabs LA1131-B) was used.

In an ideal system the total cavity length would be $2(f_1 + f_2)$, where f_1 and f_2 are the focal lengths of the lenses, as in Fig. 3.6. This means that the short cavity should have a length of 76 mm, and the long cavity should have a length of 116 mm. In reality however, the position of the lenses to achieve a self-imaging cavity is not clear. The first lens can be placed such that the emission is collimated, however the positioning of the second lens and VBG is not so easy. Since the lenses are in reality thick, and placed within mounts it can be difficult to know where to measure the intra-cavity distances from. Though the lens system magnifies the emission from the VCSEL, creating a larger depth of focus, the focal plane is also a source of error since there should be only one position for optimum feedback. Therefore in practice the second lens is placed from the approximate middle of each lens, and the frequency selective feedback element can be translated along the axis of the cavity.

The procedure to choose the correct position of the feedback element is simple. The VCSEL is biased at high current, such that with feedback the device is lasing over most of the aperture. The VBG is then translated such that when the near field plane of the VCSEL is imaged onto a camera, the highest definition of the boundary between lasing and non-lasing is reached.

The exact optical length of the cavity is not only affected by thick lenses and errors in cavity length, but also by intra-cavity components. An intra-cavity beam splitter is used to couple some light out of the cavity for detection, this induces a small path length increase. More significantly, in some realisations an intra-cavity polariser is used to control the polarisation of the cavity. This polariser is of the Glan-Thompson type, and the length is in the region of 30 mm. This beam propagation through 30 mm of glass can substantially alter the optical path length.

A rather accurate determination of the optical path length can be made by taking into account the thicknesses of all elements and by precise measurements of lengths. This is performed however the cavity length can be known even more accurately by using the RF spectrum. If the VCSEL with external cavity can be made to operate on several external cavity modes it can produces intensity modulation at the cavity round trip frequency and harmonics. The spacing of these RF modes can be measured and the external cavity free spectral range is known. From this the round trip time and hence optical length can be determined. The length determined by the RF is then compared to the direct measurement and calculation to confirm the validity and to gauge that the measurement is not wildly off-target.

The short cavity was found to have a round trip frequency of 1.65 GHz corresponding to a round trip time of 0.606 ns. The long cavity without intra cavity polariser has a round trip frequency of 1.3 GHz corresponding to a round trip time of 0.77 ns. The long cavity with an intra-cavity polariser has a round trip frequency of 950 MHz, corresponding to a round trip time of 1.05 ns.

3.3 Writing Beam

To perform switching experiments an external laser beam is required. It should be possible to switch LCS from an off-state to an on-state without changing any parameters of the CSL by shining an external beam onto the location where you wish to switch. This external laser beam will henceforth be referred to as the writing beam (WB). The WB should be tunable in wavelength to achieve optimal switching and should be able to operate in cw or produce single pulses.

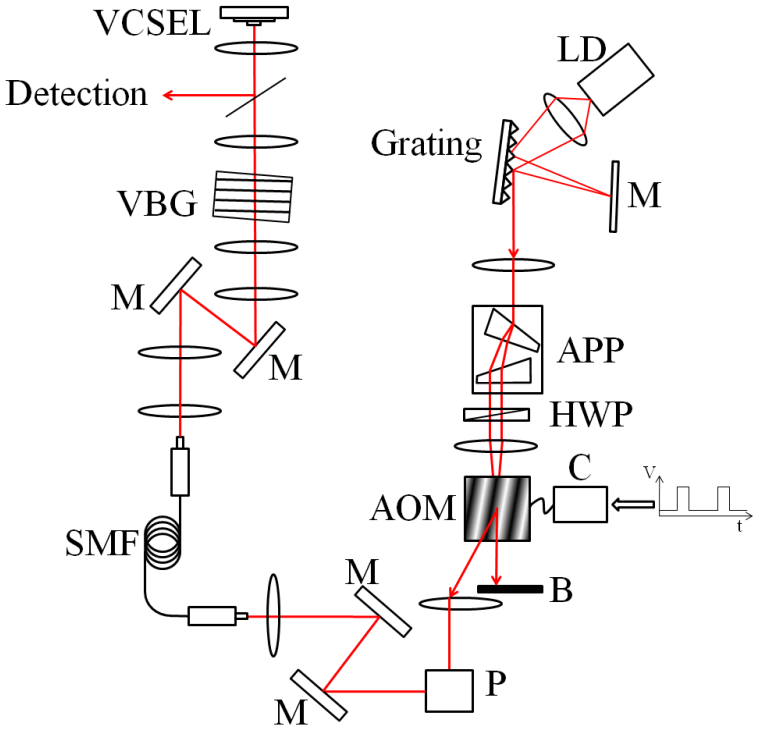

Figure 3.7: Schematic diagram of the experimental setup of the writing beam. LD: Laser diode, M: Mirror, APP: Anamorphic prism pair, HWP: Half wave-plate, AOM: Acousto-optic modulator, C: AOM controller B: Beam stop, P: Periscope, SMF: Single-mode fibre, VBG: Volume Bragg grating, VCSEL: Vertical-cavity surface-emitting laser.

The setup used to create the WB is shown in Fig. 3.7. An edge-emitting laser diode is setup with an external cavity composed of a diffraction grating and a mirror. The zeroth order is outcoupled while the first order is retro-reflected by a mirror and returns to the diode via the grating. The angle of the grating is tunable, which tunes the wavelength which returns to the laser, thus tuning the emission wavelength. This allows the WB to be tuned by up to 10 nm around 980 nm. The emission is single transverse mode and single longitudinal mode for low currents and the WB will be operated in this single mode unless otherwise stated.

The beam from the tunable diode setup is elliptical, thus it is passed through an anamorphic prism pair which stretches the short axis of the ellipse to achieve a circular beam. An acousto-optic modulator (AOM) is next and a half wave-plate

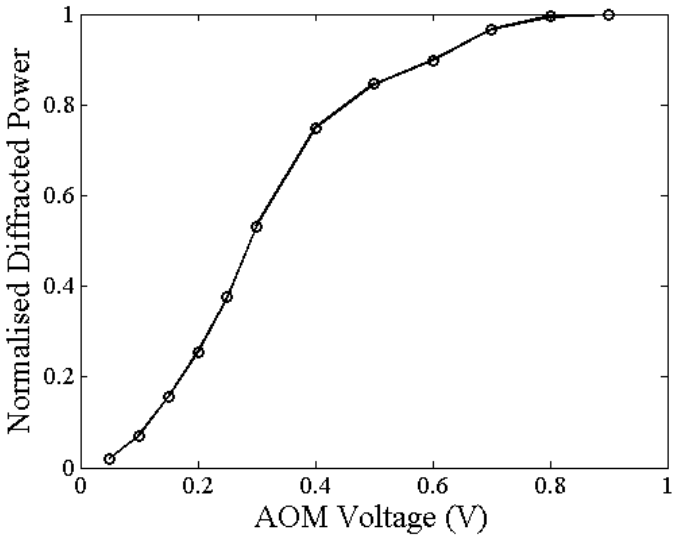

Figure 3.8: Output power of the AOM normalised to the maximum diffracted power in the first order for increasing DC input voltage.

optimises the diffracted power through it. The AOM is essentially a controllable grating. When there is no signal sent to the AOM the beam passes straight through and in this setup is blocked by a beam stop. However if a DC signal is sent to the AOM, this is converted by a control box to an AC signal which creates an acoustic wave in the AOM medium which causes incoming light to be diffracted as in a diffraction grating. The diffraction efficiency can be controlled by the strength of the DC signal supplied to the control box. Increasing the voltage increases the diffracted light such that a signal of 1 V is enough to reach saturation, however the optical output is not linear with input voltage. The output curve has been measured (Fig. 3.8) and may be used to correct for the nonlinearity.

The AOM is also capable of producing pulsed output from a cw input. If an electrical square pulse is applied to the AOM via the control, then an optical pulse which is approximately equal in length to the electrical pulse is produced. For short pulses the electrical and optical pulses lengths do not match due to the rise time limit of the AOM, which limits the optical pulse length to as short as 15 ns. Due to the rise time, pulses close to the lower limit are essentially Gaussian, whereas long pulses are essentially square if driven by square pulses.

The diffracted beam from the AOM passes through a periscope which raises the beam up to the height of the fibre coupling stage. Two steering mirrors and a lens mount with fine adjustment are used to couple the WB into a single mode fibre which ensures high beam quality at the output and gives flexibility to the setup. The trade-off is reduced beam power, with typical fibre-coupling efficiencies of 60%.

For injection into the CSL, the WB is outcoupled and then passes through beam expanding optics which ensure that the beam size of the WB matches that of a LCS at the VCSEL surface. Two mirrors are used to control the position of the beam on the VCSEL while ensuring that the beam is also on-axis with respect to the LCS. The beam also passes through a linear polariser and then a half wave-plate such that the injected beam may have any polarisation desired.

To inject the writing beam into the CSL cavity two options are available, injection via a beam splitter and injection through the VBG. A beam splitter is already in place to couple the light out of the cavity for detection, therefore the first option would be to inject the WB via this beamsplitter, on the opposite side to the outcoupled detection arm. This however has the issue that the WB would first travel to the VBG and thus injection which is not resonant or near-resonant with the VBG is not possible. A second beamsplitter could be added but this would not allow enough space to place an intra-cavity polariser, adds losses to the cavity and would make the coupling polarisation dependent. The WB is thus injected through the back of the VBG which results in the power reaching the VCSEL depending strongly on wavelength since at the VBG reflection peak, there is essentially no transmission. However since it is desirable to bypass the external cavity resonance, such that the writing need not rely on this resonant enhancement to be effective, injection away from the VBG peak allows for superior in-coupling than the beamsplitter method.

3.4 Detection Details

In this section the methods and parameters for specific experiments shall be detailed. For reference the basic experimental setup is shown in Fig. 3.9.

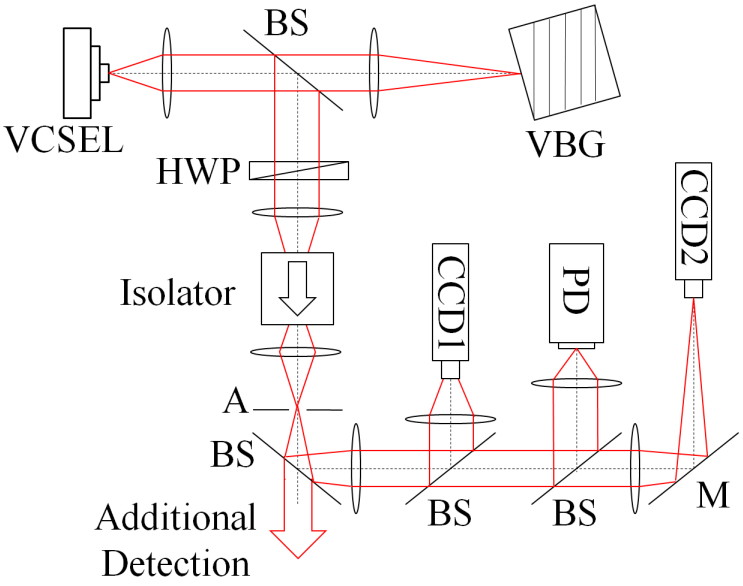

Figure 3.9: Basic experimental detection setup. VCSEL: Vertical-cavity surface-emitting laser, VBG: Volume Bragg grating, BS: Beamsplitter, HWP: Half wave-plate, A: Spatial aperture, M: Mirror, PD: Photodiode, CCD1(2): Far (Near) Field camera.

The light is coupled out of the cavity using the Fresnel reflection from an uncoated glass plate. This plate is referred to as a beam splitter. Due to the nature of Fresnel refections, this reflection is polarisation dependent, reflecting approximately 10% of the polarisation perpendicular to the table and 1% of the polarisation parallel to the table when placed at an angle of incidence of 45° to the incoming beam.

The detection elements are separated from the CSL using an optical isolator. This acts as an optical diode, allowing light to pass only in one direction, such that there is no feedback from the detection to the CSL. The isolator utilises a Faraday rotator placed between two linear polarisers. The half wave-plate before the isolator aligns the incoming polarisation to match the front polariser for maximum transmission. The linearly polarised light is then rotated by the Faraday rotator and is turned by exactly 45° by the end of the isolator. The output polariser is aligned at this angle to allow all light to pass. If light enters in the opposite direction and is aligned to pass the rear polariser, the polarisation would be rotated such that when it reached the front polariser, the light would be

orthogonally polarised with respect to this polariser, hence blocking transmission. This effect can be used to isolate with up to 40 dB attenuation however as a consequence of this method of isolation, only a single polarisation is detected at a time.

3.4.1 Images

Two CCD cameras are incorporated into the experimental setup, one which produces images of the VCSEL gain region (near field) and one which produces images of the fourier plane of the VCSEL gain region (far field). The near field camera is a Pulnix TM-765E which has 756×581 pixels, each $11\mu\text{m} \times 11\mu\text{m}$. The output voltage ranges have been set to the most linear parts of the camera responses. The far field camera is custom constructed with greyscale output from 756×581 pixels.

The imaging system for both cameras is based on a series of telescopes (beam expanders). The setup of a telescope lens system is the same as that seen in Fig. 3.6, where the image at the input of the system is directly imaged at the output with a magnification of f_2/f_1. The cameras have a detection aperture of approximately 5×5mm hence the 200 μm VCSEL aperture must be expanded by a factor 25 to fill the camera chip.

Fig. 3.9 shows the experimental setup with the beam path and cameras. The light is first expanded by two telescope systems and then imaged 1:1 by a single lens. An adjustable spatial aperture is placed in this re-imaged near field plane to provide spatial filtering of the detected light which will allow the detection of only part of the VCSEL, e.g. a single CS . This image plane is then further magnified by another telescope and the camera is placed in the re-imaged VCSEL image which now has a diameter of approximately 4 mm. A set of adjustable neutral density filters are placed before the camera to avoid over-exposure. The exact placement of the camera is adjusted such that the spontaneous emission aperture boundary has the highest definition.

The setup for the far field camera follows the same path until the lens after the spatial aperture, but afterwards a beam is split off and passed through another lens with shorter focal length than that of the near field imaging. The far field

plane is identified by placing a thin wire in the far field plane of the VCSEL after the first lens. The camera is then moved in the beam path until the edge of the wire has the highest definition. A set of adjustable neutral density filters are placed before the camera to avoid over-exposure.

The cameras are both connected to a PC via an IMAQ frame grabber which allows images to be saved via a LabVIEW program producing a 10-bit greyscale image. LabVIEW is a visual programming language (using icons rather than lines of code) which specialises in making virtual instruments, and is particularly well suited to lab experiment automation.

3.4.2 LI Curves

A light–current curve (LI curve) measures how the laser output varies with pump current. Typically these would be used to find lasing threshold points and the thermal rollover point. In a standard LI curve the current is only ramped in one direction, i.e. increased, however since bistability is desired and expected in a CSL, the current is ramped in both direction, upwards and then downwards. Bistability would then manifest itself as differing output levels between the up-ramp and down-ramp for a range of current values.

The light output from the CSL is monitored on a slow (sub MHz temporal bandwidth) photodetector (Siemens BPW 34) with adjustable gain (3 orders of magnitude variable). The output of this photodetector is then connected to a computer and read by a DAQ board. The DAQ is a analogue to digital signal converter allowing the computer to read and write to various instruments, in this case it is reading an analogue photodetector output signal.

The current is supplied by an Arroyo 4210 current driver capable of supplying currents up to 1000 mA with 0.1 mA resolution and an accuracy of $0.05\% \pm 0.2$. This current driver is connected to a PC via a USB cable acting as a virtual serial port.

The LI curve is then performed automatically by a LabVIEW program running on the PC. The LabVIEW program incrementally increases the current to the laser and then records the reading on the photodetector at each step. When

the maximum specified current is reached, the current is then decreased and the photodetector output measured at each point once more.

The speed at which to perform the ramp required some consideration, if it is performed too quickly then the experimental system will not be able to react in time, and will lag behind the inputs. In particular there are thermal effects to consider, as increasing current to the laser will increase temperature via Joule heating. If the current is ramped too quickly then the device temperature will lag behind the inputs, causing erroneous bistability, i.e. the intensity profile measured for increasing and decreasing current will differ from each other simply because the system is not in thermal equilibrium for any current. This is not to be confused with true optical bistability, which is characterised by abrupt transitions in intensity and is present for even very slow scan speeds.

To ensure that there is no error arising from the speed of the ramp, an LI curve is performed very slowly, in a region where the up-ramp and down-ramp intensities should overlap (i.e. there is no hysteresis or bistability). The speed of the ramp is then increased until the up-ramp and down-ramp no longer overlap, and this is the threshold for erroneous bistability. The speed is then reduced once more to avoid this erroneous bistability and thus in this way the optimum speed for the ramp was measured to be approximately 1 mA/s and all LI curves were performed at this rate.

3.4.3 Optical Spectra

The first instrument used to record optical spectra is an optical spectrum analyser (Hewlett Packard 86140A). The primary limitation of this device is the poor spectral resolution (0.07 nm or 22 GHz at 980 nm) and it is therefore unsuitable for spectra which require a high degree of resolution. It is however useful for finding absolute wavelengths, a measurement which is not available with a Fabry-Perot interferometer.

Fabry-Perot spectra are measured using a scanning confocal Fabry-Perot interferometer. This is composed of two mirrors with radius of curvature -7.5 mm and reflectivities $> 99\%$. One mirror is stationary, the other is attached to a piezoelectric transducer. A ramping high voltage is supplied to the piezo which scans

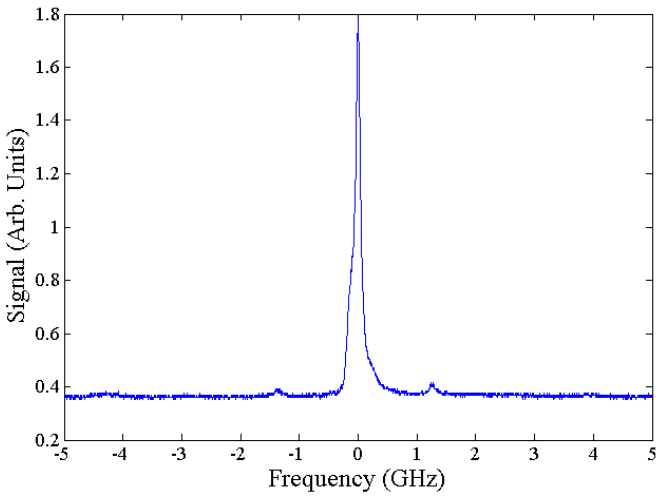

Figure 3.10: Sample Fabry-Perot Spectrum showing the main peak at zero with small side peaks at 1.3 GHz.

the length of the cavity. A photodiode is placed after the cavity and connected to an oscilloscope, which is then triggered on the voltage ramp to synchronise both and the result is a signal which is very low when the cavity is off-resonance to the light, and high when in resonance. In this way we obtain an optical spectrum of the incoming light. A complete scan with several repetitions of the spectrum are taken to normalise the frequency to the free spectral range (FSR) of the confocal cavity. The spectrum is then cropped to one peak and one FSR, a sample spectrum is shown in Fig. 3.10. From this spectrum the finesse of the cavity is observed to be 93.

The alignment of the cavity is extremely important and some time was taken to optimise this alignment, however there is still some erroneous asymmetry in the Fabry-Perot peaks which may be attributed to a non-linear piezo scan or the very short cavity length making perfect alignment troublesome.

The free spectral range (FSR) of the cavity should be 10 GHz from the theoretically expected value, and this was indeed verified to be the case experimentally, with an error less than 1%.

The oscilloscope measuring the spectra is connected to the PC such that the spectra may be recorded. This also allows the spectra to be taken while scanning

another parameter. In the case that we wish to scan the current while measuring spectra the Fabry-Perot spectrum is taken for each value of the current and afterwards plotted in a 3 dimensional plot with current and frequency being the two parameters.

3.4.4 Polarisation Angles

To measure the polarisation of the LCS the experimental setup is altered from the norm by removing the beamsplitters leading to the Fabry-Perot interferometer and cameras. We then place a Wollaston polariser in the beam path and send each polarisation component to separate detectors. For a rigorous determination of the entire polarisation state all four Stokes' parameters for each LCS should be measured. However, for simplicity, to characterise the polarisation state in this first investigation only the relative intensities in the polarisation components parallel and perpendicular to the table are measured. The measured intensities are then normalised to account for the polarisation anisotropy of the beam splitter discussed in Sec. 3.4. We then convert these two intensities, I_x and I_y respectively, to an associated polarisation angle, θ, where:

$$\theta = \tan^{-1}(\sqrt{I_y/I_x})$$

For this calculation the unpolarised spontaneous emission contribution is removed and this is taken before each measurement by blocking the feedback from the VBG and recording the LI-curve, thus obtaining the polarisation state of the LCS only.

3.4.5 Fast Dynamics

The presence of an external cavity in this realisation of a CSL leads to the possibility of the LCS operating on several external cavity modes. This can produce mode beating or mode locking behaviour leading to fast temporal dynamics at timescales relating to the external cavity round trip and its harmonics. To probe the time domain it is therefore necessary to use specialised equipment with high frequency bandwidth detection.

There were two detectors used to measure the temporal dynamics of LCS. For dynamics below 2 GHz an avalanche photodiode (APD) was used and has a 3 dB bandwidth point of 1.2 GHz (New Focus 1647), however frequencies up to 2 GHz can still be resolved. The APD has integrated, adjustable gain and this results in an optimum conversion gain of 14000 V/W which means that external amplification is not required. The second detector used for higher frequency dynamics is a photodetector with a 3 dB temporal bandwidth of 12 GHz (New Focus 1544-A). The output is boosted by an integrated transimpedance gain of 1000 V/A however due to the low intrinsic powers of an LCS, this is still insufficient gain in most cases. To boost the output an external amplifier (Picosecond Pulse Labs 5867) with temporal 3 dB bandwidth of 15 GHz and 15 dB gain is used. Both of these detectors are fibre-coupled and the fibre is placed at the point marked 'additional detection' in Fig. 3.9 to maximise power to the detector while still sending some power to the cameras.

For time-averaged measurements a low bandwidth (100 MHz Tektronix TDS 3014B) oscilloscope is used however when time resolution is required an oscilloscope with higher temporal resolution is required. Three separate oscilloscopes were used for these time-resolved measurements. The LeCroy Wavepro 960 has a temporal bandwidth of 2 GHz and a maximum sampling rate of 16 Gs/s. The LeCroy Wavemaster 820Zi has a temporal bandwidth of 16 GHz and a max sampling rate of 40 GS/s. Finally the Tektronix DPO71604B has a temporal bandwidth of 16 GHz and a sampling rate of 50 GS/s.

3.4.6 Time-Frequency Analysis

It is possible to create a frequency spectrum by Fourier transforming a time series. However if the frequency spectrum is known to evolve over the time window, such as in the case of a switching event, then the frequency spectrum should be evaluated many times over the time window to plot the evolution.

Time frequency analysis converts a time series into a spectrogram which plots how intensity modulation frequency varies in time. This is achieved by splitting the time series into many sections and performing a fourier transform on each

section. A MATLAB program performs this calculation and the three main parameters are the window size, overlap size and FFT (fast Fourier transform) size. The window size specifies how many points are in each Fourier transform, and is set to 1024 for future results. The overlap specifies how much one window overlaps another window and is set to 1000 to increase the temporal resolution. Finally FFT size is set to 1024 to match the window. In the case that there is a strong DC (0 frequency) component then the lower frequencies are removed from the final figure to increase the clarity of the high frequency components. The upper frequency can be as high as half of the sampling frequency however the upper frequency cutoff is set to 10 GHz since the frequency components typically die out before.

3.5 Theoretical Model

The following model was developed by the computational nonlinear and quantum optics group (CNQO) at Strathclyde and though I played no part in its development, it is included for reference to following results.

To model the basic experimental set-up, separate descriptions of the VCSEL device and the VBG are required. The latter provides frequency–selective feedback, lowering the laser threshold but only in a narrow frequency range around the peak of the Bragg reflection. Away from this frequency the feedback is negligible, as most light is transmitted by the VBG.

The temporal dynamics of semiconductor lasers with optical feedback has been modeled for some time (see for example [59]). The present experimental setup however, requires the inclusion of the transverse-space degrees of freedom, including diffraction, and also of high reflectivity of the feedback mirror. All of these elements are combined in a single model that can be compared with the experimental realisations and does not restrict to purely temporal regimes and/or introduce restrictions in the magnitude of the feedback [108].

The model for the intra–VCSEL optical field E and carrier density N is based on that used for the study of CS in amplifiers [15, 88, 113]. The holding beam is, however, replaced by the external cavity field at the VCSEL output mirror,

F. The complete system is described by the following system of coupled partial differential equations and mapping [108]:

$$\begin{aligned} \partial_t E &= -(1+i\theta)E + i\nabla^2 E - i\sigma(\alpha+i)(N-1)E \\ &+ \frac{2\sqrt{T_1}}{(T_1+T_2)}F \\ \partial_t N &= -\gamma\left[N - J + |E|^2(N-1) + D\nabla^2 N\right] \\ F(t) &= e^{-i\delta\tau_f}\hat{G}(t-\tau_f/2)\ [-r_1 F(t-\tau_f) + t_1 E(t-\tau_f)] \end{aligned} \tag{3.1}$$

where θ is the detuning of the VCSEL cavity with respect to the chosen reference frequency, σ is a coupling constant, α is the linewidth enhancement factor, T_1 and T_2 are the transmittivities of the VCSEL mirrors, and J represents the injection current, normalised to the value at transparency. Time is scaled to the VCSEL cavity lifetime, and γ is the ratio of cavity lifetime to carrier response time in the VCSEL. The term $\nabla^2 E$ describes diffraction in the VCSEL cavity. $D\nabla^2 N$ is the carrier diffusion but it is usually considered small, and will henceforth be omitted.

The external cavity round–trip time and its detuning at the reference frequency are denoted by τ_f and δ respectively, while r_1 and t_1 are the (real) amplitude reflection and transmission coefficients of the VCSEL output mirror, (i.e. $T_1 = t_1^2 = 1 - r_1^2$: for a detailed description of the external cavity, see [45]). The operator $\hat{G}$ describes the frequency–selective operation of the Bragg reflector on the field envelope and is given by

$$\hat{G}(t)\ [h(t)]\ = \frac{r_g}{2\beta}\int_{t-2\beta}^{t} e^{i\Omega_g(t'-t)}\ h(t')\ dt' \tag{3.2}$$

in the time domain or, equivalently,

$$\hat{G}(\omega)\ [h(\omega)]\ = r_g\ e^{-i\beta(\Omega_g-\omega)}\ \mathrm{sinc}(\beta(\Omega_g-\omega))h(\omega) \tag{3.3}$$

in the frequency domain. The frequency $1/\beta$ determines the bandwidth of the Bragg reflector while Ω_g is its central frequency (henceforth referred to as the Bragg frequency) relative to the reference (carrier) frequency. The parameter r_g

is an overall reflection coefficient. Note that in this description we neglect the transverse wavevector dependence of the reflector response. We have also ignored transverse effects of free–space propagation (i.e. diffraction) in the external cavity, since in the corresponding experiment the VCSEL output coupler is imaged directly onto the Bragg reflector (see Fig. 6.1). Note that all variables and parameters in Eqs. (3.1) are dimensionless. We use $\Omega_g = 0$ here, i.e. the carrier frequency is chosen to be the Bragg frequency.

The validity of Eqs. (3.1) extends to regimes of high reflectivity of the feedback mirrors that cannot be investigated with the more usual Lang–Kobayashi (L–K) approximation for lasers with external feedback [59, 64, 84, 85], in which the effects of multiple round trips in the external cavity are neglected. The model (3.1), however, describes operational regimes of CS lasers with arbitrarily high reflectivities of the frequency–selective feedback mirror and captures the physical status of the feedback loop as a true optical cavity [45]. From the simulation point of view, the inclusion of multiple round trips is accomplished with essentially no computational overhead with respect to the L–K approximation [108]. CS have been described in [108].

Chapter 4

Laser Cavity Solitons in a VCSEL with Frequency Selective Feedback

In this chapter the general properties of the observed lasing emissions are outlined. The spatial properties will be explored first, followed by characterisation of the optical properties. Following this the spots which are present in the system shall be confirmed to be cavity solitons via the standard criteria of locality, bistability, mobility and independence.

4.1 Threshold Properties

If the VCSEL does not emit wavelengths which overlap the reflection band of the VBG, then the frequency selective feedback (FSF) has no effect. For this reason the VCSEL should be temperature tuned such that the cavity resonance of the VCSEL approaches the VBG reflection peak (See Sec. 3.1 for tuning details). To this end the VCSEL is heated to $81°C$. As described in Sec. 3.1 the threshold at low temperatures ($16°C$) is around 405 mA however at $81°C$ the threshold has shifted and is now not reachable for currents below the damage threshold, i.e. free running lasing is not possible.

With the VCSEL cavity resonance tuned such that the VCSEL will experience

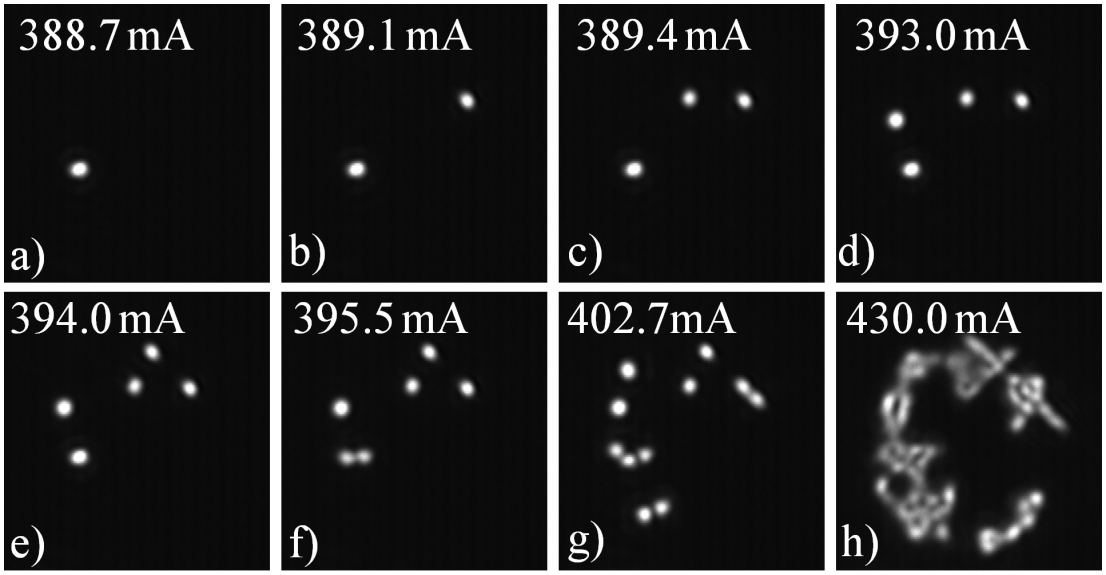

Figure 4.1: Near field images taken when increasing current to the values shown inset. White corresponds to high intensity. Area shown in each image is approximately $220\mu m \times 220\mu m$.

feedback, lasing can be achieved. When the current supplied to the VCSEL is increased, at some current a small lasing spot will appear (Fig. 4.1a). The value of this threshold current varies with the temperature of the device, however an accurate study of this dependence in this system is not possible due to inaccurate temperature control and detection. An estimate of this dependence can be gathered from the previous realisation in [119], which utilises the same VCSELs with different frequency selective feedback. For that system the threshold current dependence on temperature was found to be linear with a rate of 1.6 mA/K [25].

Increasing the current further yields a further lasing spot, separate from the first (Fig. 4.1b). The additional spots continue to appear for increasing current (Fig. 4.1c-f) and their appearance is very abrupt, with no lasing pattern or visible increase in spontaneous emission preceding it, just a sharp and sudden switch on and this will be discussed in detail in the sections which follow. At higher currents, spots which were already formed can make a sudden transition to a multi-peaked structure (Fig. 4.1f-g). If the current is increased yet further then the spots turn to extended lasing patterns or structures (Fig. 4.1h) and even higher current returns the VCSEL to a lasing state which closely resembles the same system

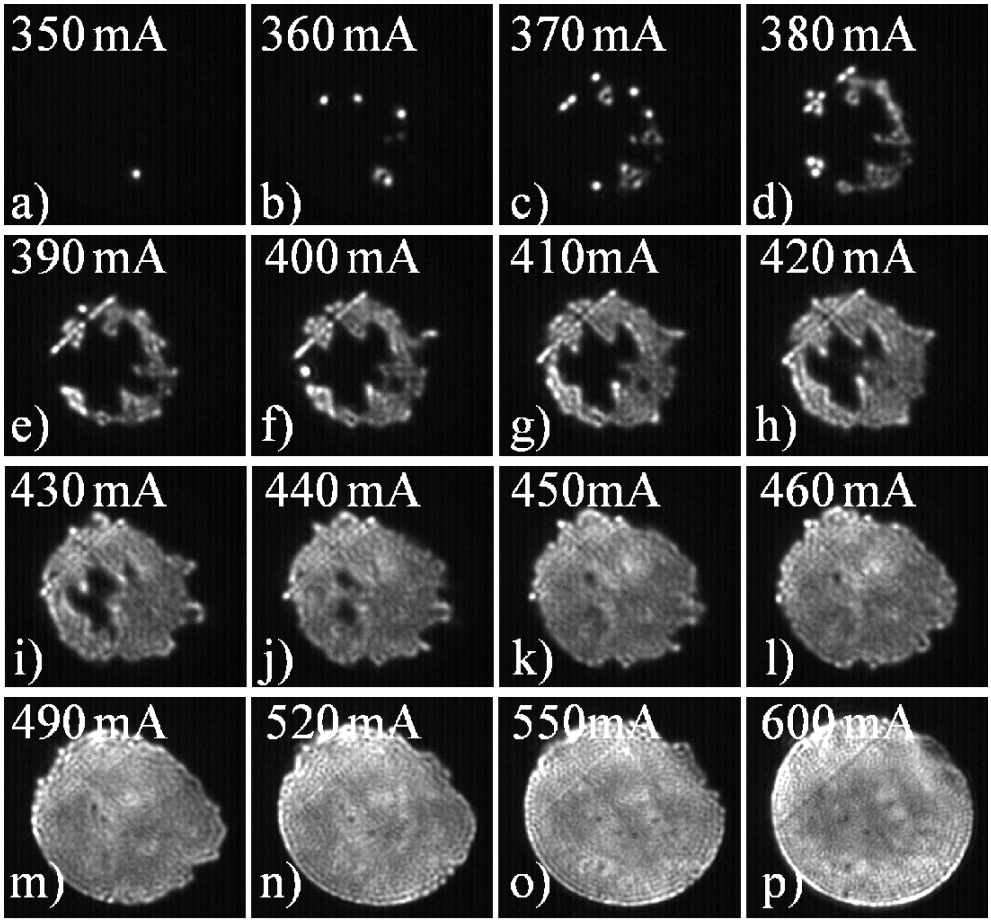

Figure 4.2: Near field images taken when increasing current to the values shown inset. White corresponds to high intensity. Area shown in each image is approximately $220\mu m \times 220\mu m$.

with feedback from a plane mirror, i.e. spatially extended lasing states which cover the entire aperture. This evolution all the way up to the spatially extended states is shown in Fig. 4.2 and the states in Fig. 4.2m-p resemble closely the states which lase when a standard plane mirror is used in place of the VBG. It should be noted at this point that during the course of this work, an additional mirror has been placed in the setup before the near field camera. This should have the effect of flipping some of the images from left to right, as is the case from Fig. 4.1 to Fig. 4.2. Throughout this thesis both flipped and unflipped images are displayed and one should be mindful of this.

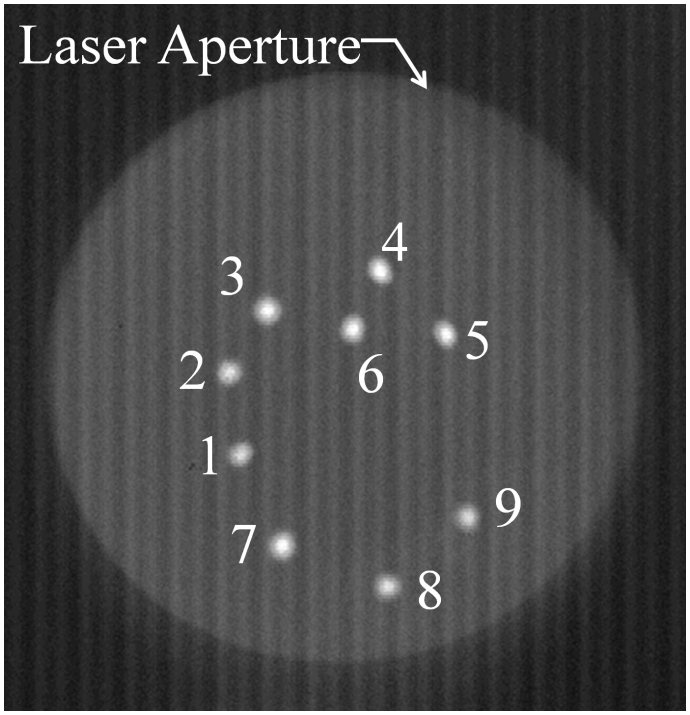

Figure 4.3: Image showing the relative position and numbering of the nine spots. This is created by overlaying pictures of each spot at threshold together with a picture of the laser aperture below threshold.

If the current ramp is repeated within one experimental campaign, the spots always appear in the same position and in the same order with approximately the same thresholds from ramp to ramp. Over longer periods of time, days to months, the relative thresholds of the spots differ, and some spots even cease to appear however the spots always appear in the same places. Since the spots are repeatable, and predictable, for one set of experiments it is useful to label each spot for further study. Fig. 4.3 shows the nine spots with lowest threshold and their relative positions to each other and to the VCSEL boundary. This figure was created by spatially filtering each spot at it's respective threshold such that only the single spot is visible in the camera. These nine pictures are then overlaid onto an image of the spontaneous emission to compare their positions and their proximity to the boundary. Therefore this picture is only for reference, as there is no current at which all spots are single peaked.

The reproducibility of the thresholds of the spots is demonstrated in Fig. 4.4,

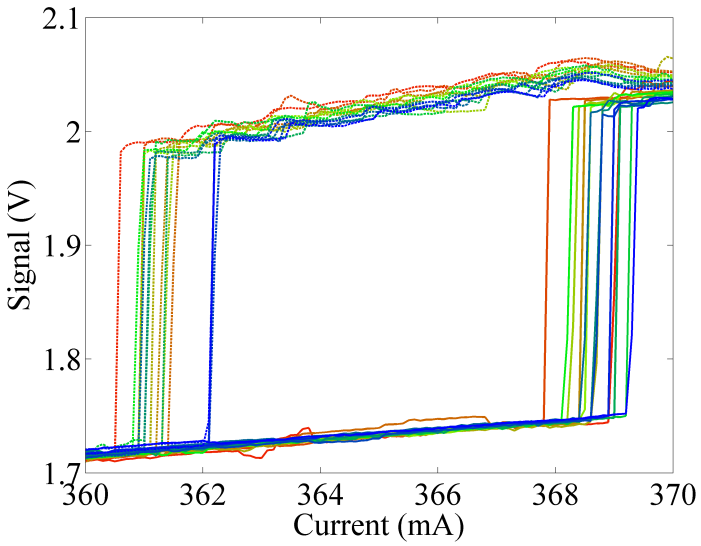

Figure 4.4: Fifteen LI curves taken for spot number 1 (see Fig. 4.3) with increasing (solid line) and decreasing (dotted line) current. The different colours represent each new scan. The total time from the first scan to the last scan was 9 minutes.

where the current was ramped up and down repeatedly. Only one spot is spatially selected for the detection. Concentrating on the upward scan of current (Solid line) it is observed that the intensity varies very little until the threshold current for a spot is reached (369 mA), at this point the intensity increases abruptly corresponding to the appearance of a lasing spot. This transition will be henceforth referred to as a switch-on. For repeated upward scans the current at which this switch-on occurs remains reasonably constant, with a variation of around $1mA$ over a timescale of 9 minutes. The reason for the fluctuation in threshold current is believed to be due to macroscopic thermal fluctuations. The temperature controller is capable of stabilising the laser submount temperature to some mK however the thermal contact with the submount can be sub-optimal, leading to small temperature fluctuations.

The downward current scans shown in Fig. 4.4 show that the spots do not switch off at the same current at which they switch-on. During the downward scan of current, between 361 mA and 369 mA the spot is still lasing, which was not the case for increasing current. This property is referred to as 'hysteresis' which is a result of bistability and will be discussed in detail in further sections.

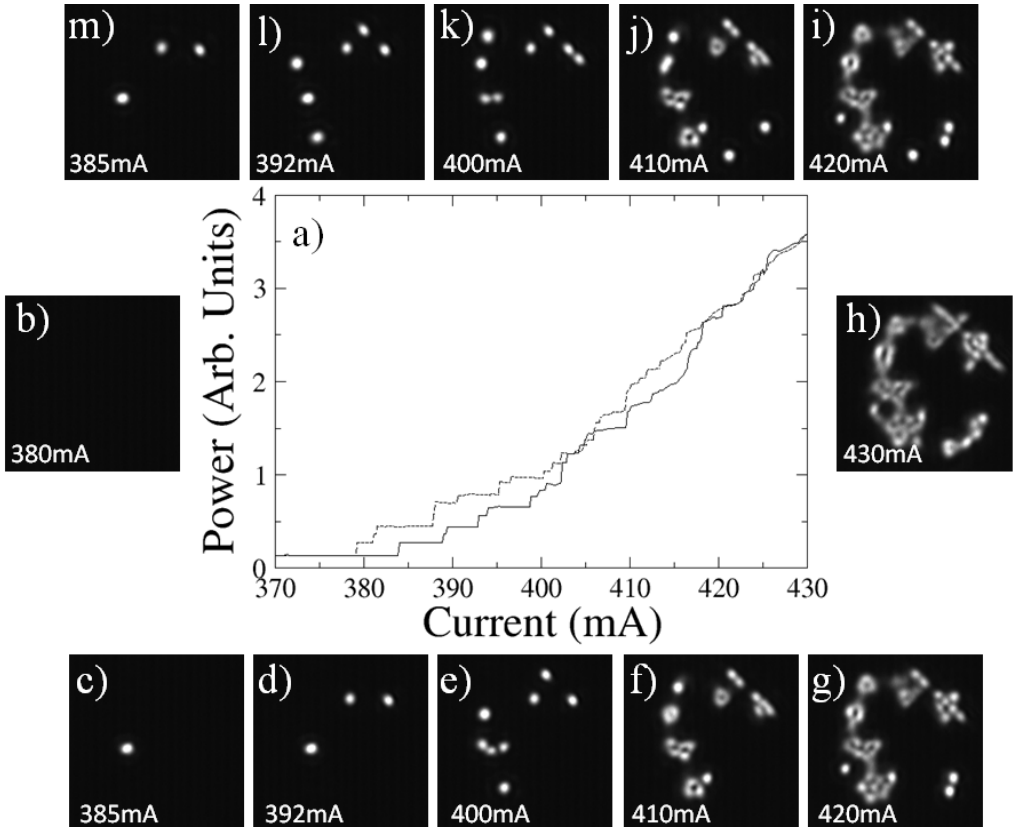

Figure 4.5: a) LI-curve taken over the whole VCSEL aperture. The solid line was taken with increasing current and the dashed line was taken for decreasing current. (b)-(g) Images taken for increasing current, (h)-(m) images taken for decreasing current. The images display near field intensity distributions at their respective current values. White corresponds to high intensity. The pictures show an area with size approximately 200 μm $\times$ 200 μm. Measurements taken at 0.1 mA intervals at a rate of 1 mA per second to avoid thermal hysteresis. The analysing polariser was set such that all spots have approximately equal intensity.

Once again it can be seen that there is a jitter in the off-switching point and this should be due once again to the thermal fluctuations.

If an LI curve is recorded for the entire VCSEL aperture, not just for a single spot as before, then the LI curve in Fig. 4.5 is obtained. All nine of the lasing spots show bistability. Not only this but the transition from spots to structures with multiple peaks also displays bistability between intensity levels. In actual fact the system output results from the switching on and off, at different thresh-

olds, of individually-bistable spots. In other words, the system is highly bistable and probably multi-stable, but this is not yet proven. The bistability and the possibility of multi-stability will be explored in a further section.

4.2 Size and Angular Spread

The single peaked spots have intensity distributions which are shown in Fig. 4.6. To characterise the width of the spots a Gaussian fit is employed and gives quite good fits with sizes ranging from 4.8 μm to 5.8 μm (radius at $1/e^2$-point of intensity, see Table. 4.1 for individual sizes). The inclusion of a Gaussian fit may seem odd, since typically dissipative soliton profiles are non-Gaussian and while the fits in Fig. 4.6 seem to be well suited, certain realisations show the spots to have dark rings in the wings, a feature not possible with a Gaussian profile. Thus a Gaussian profile is used to obtain the widths of the spots, but it is merely a measurement tool of convenience, and it should be noted that other profiles are possible, even more likely. It should be noted that though the intensity of each spot is measured to be different, this is due to the polarisation sensitive detection scheme. As will be discussed in detail later the spots each have their own polarisation. The outcoupling beamsplitter couples out 1% of the horizontally polarised component and 10% of the vertically polarised component. This anisotropic coupling leads to differing detected intensities of each spot which is dependent on the polarisation state. The expectation is that each spot has nominally the same amplitude, differing only due to a spatial variation of cavity parameters. While there is not a substantial variation in intensity, a qualitative study was never performed.

The angular spread in far field for each spot can be seen in Fig. 4.7. Their angular widths are between 57 mrad and 69 mrad (again radius at $1/e^2$-point of intensity, see Table. 4.1 for individual sizes), which is indistinguishable from being diffraction limited within the experimental uncertainty, i.e. the spots have a high spatial coherence. The widths are once again characterised by a Gaussian fit for simplicity and in the wings of the distribution this fits well however the peaks of the distributions are better estimated as a sharp monotonic peak. This supports the previous assertion that the spots are not exactly Gaussian.

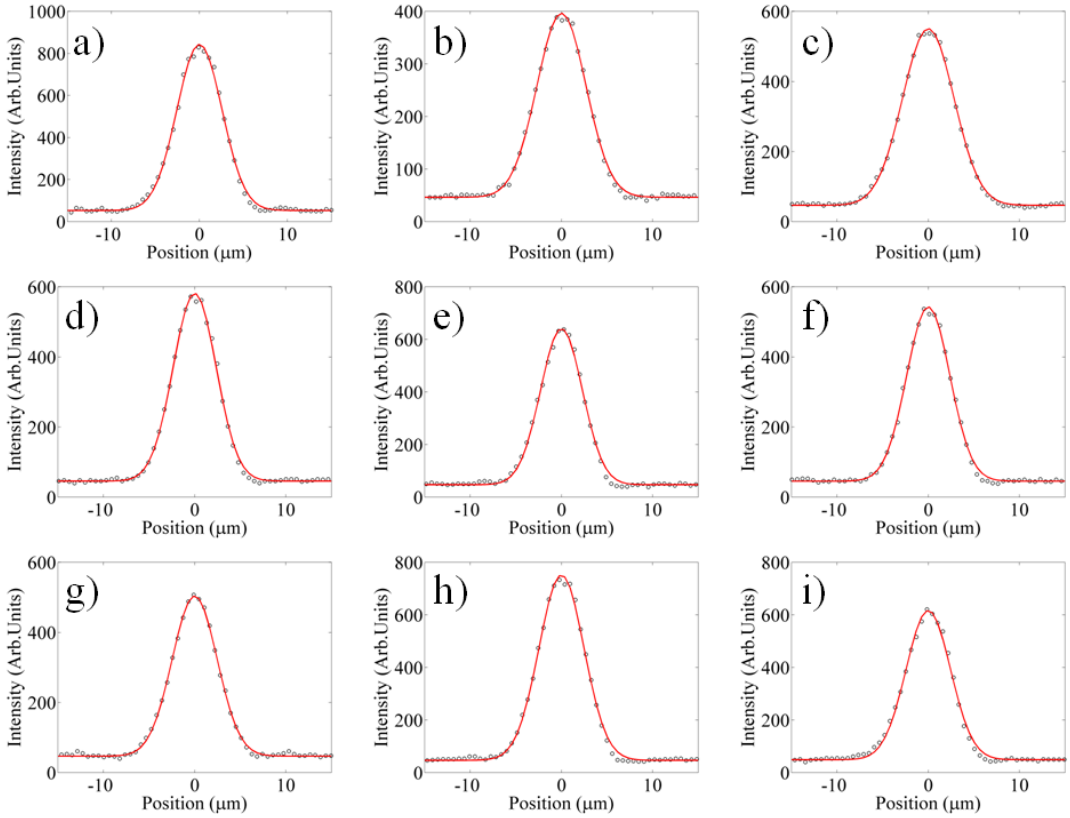

Figure 4.6: Near field profiles of the 9 spots. a)-i) Near field profiles (dots) with Gaussian fit (red line) of the spots in numbered order (See Fig. 4.3 for numbering).

Under normal operation the external cavity is aligned such that at high currents, when the VCSEL is producing spatially extended lasing emission, the corresponding emission structure is approximately symmetrical, i.e. ring-shaped. The centre of this ring coincides with the centre of the spots within 18 mrad or 15% of the spot radius, i.e. the spots emit essentially on-axis. (The centre of the free-running laser emission is only accessible at low temperatures, and agrees within about 20 mrad with the centre at high temperature in presence of feedback. Hence it is thought that the optical axis is hard to determine with a much higher reliability.)

These observations match qualitatively the ones made before while using a diffraction grating as frequency-selective element [119, 127], but typically there are more, smaller spots in the system with VBG and a better discrimination

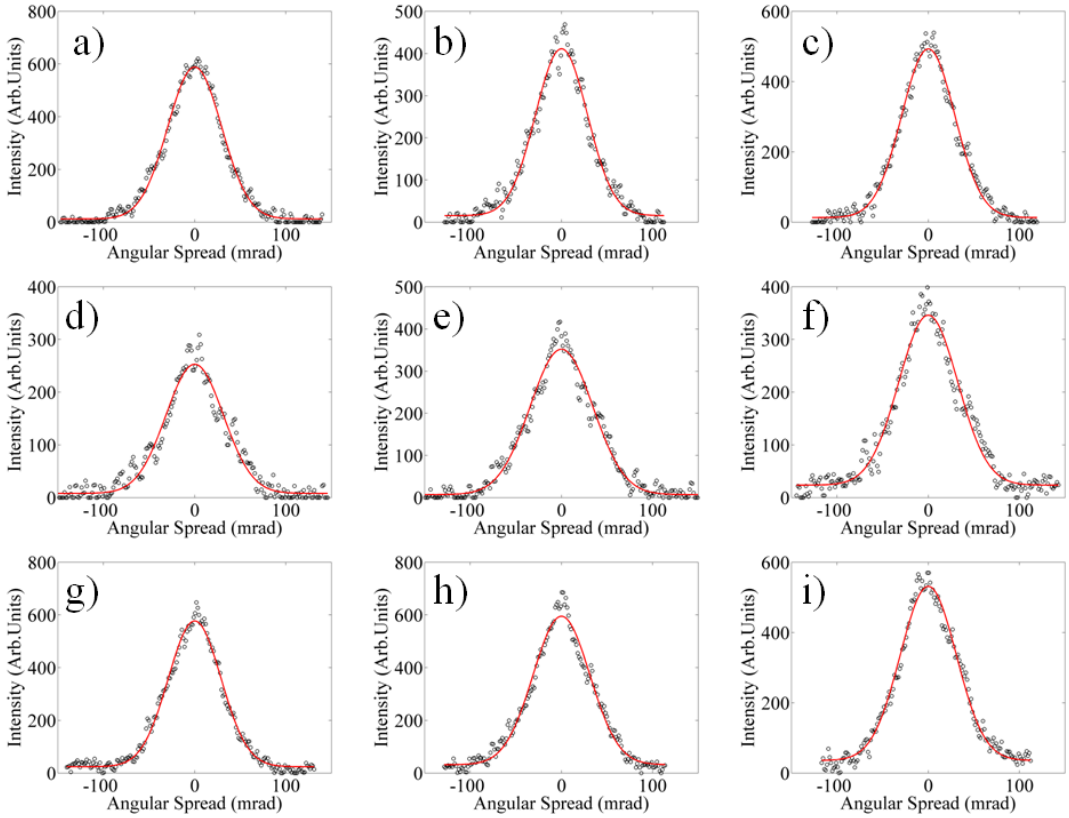

Figure 4.7: Far field profiles of the 9 spots. a)-i) Near field profiles (dots) with Gaussian fit (red line) of the spots in numbered order (See Fig. 4.3 for numbering).

Table 4.1: Near and far field width of each spot at the $1/e^2$ radius point, just above their respective thresholds.

Spot	Near Field Width (μm)	Far Field Width (mrad)
1	5.30	59.03
2	5.58	56.91
3	5.84	58.25
4	4.88	62.98
5	4.76	68.78
6	4.82	64.72
7	5.10	57.81
8	5.12	62.14
9	5.04	61.41

between extended patterns and spots. The width of the spots' hysteresis loops are also significantly larger in the VBG system.

4.3 Spatial Evolution with Current

The evolution of lasing intensity with current as seen in Fig. 4.5 shows that there are many sudden jumps in intensity for the lower currents and a smoother transition at high currents, but remaining bistable for the majority of currents. The upper smooth transitions are attributed to the spots 'dissolving' to an extended lasing state. This can be interpreted as a self-localised, bistable state becoming disfavored and a spatially extended lasing mode becoming favoured.

At lower currents the sudden jumps in intensity can be attributed to two phenomena. The first is the appearance of a new spot, separate from all other spots and patterns. The second is the evolution of an already formed spot into a structure with multiple peaks, or from a multi-peak structure to another with more peaks.

4.3.1 Multiple Spots

Fig. 4.8 shows the evolution of intensity and spatial distribution of lasing. For increasing current below 415 mA the dark state corresponds to the background state of purely spontaneous emission. At 415 mA there is a sudden transition to a higher intensity state and this corresponds to the appearance of a spot as seen in the inset images in Fig. 4.8. This intensity level remains constant with only a small increase attributed to the increase in spontaneous emission level until at approximately 416 mA there is another sharp increase corresponding to the appearance of a second spot, spatially separated from the first at a distance of some three soliton diameters ($\sim$30 μm) away (visible in the lower inset image for 420 mA in Fig. 4.8). This intensity level again remains constant until the next sudden jump at around 421 mA. At this current there is a small increase in intensity closely followed by a further large jump. The small increase corresponds to a spot appearing directly next to the rightmost spot and to differentiate this phenomena from the appearance of an additional spot which is spatially separated

from the other spots this shall be referred to as a 'splitting'. The character and properties if these splitting events will be discussed in the next section. The large increase in intensity directly after the splitting event corresponds to the appearance of a third spatially separated spot such that there are now two single spots and a 'split spot' as shown in the bottom rightmost inset image in Fig. 4.8.

When the current is decreased the spots remain stably in the on-state in current regions where they were previously in the off state until they destabilise and once again switch sharply to the background state. The order of the switching is however different, and this is manifest in the fact that the first state to switch down is the split spot. When the current was increased the righthand spot split, followed by the appearance of the third spot, however the bistable range of the splitting is smaller than the range of the third spot which leads to a state in which the three spots exist, single-peaked between approximately 414 mA and 416 mA, a state which was not possible for increasing current. Lowering the current results in each spot switching down in the order in which they appeared.

This appearance of new spots is one contribution to the bistability, as can be seen by the different intensity levels for the same current between increasing and decreasing currents. The second contribution is from the aforementioned splitting events and will be discussed in the next section.

4.3.2 Splitting

As indicated the spots are in general single-peaked at threshold and dissolve to a lasing pattern at high current as described previously. For intermediate currents however we see some interesting effects, which are analysed in Fig. 4.9 for the lowest threshold CS. It is single-peaked at threshold (385 mA) but at some higher current the CS 'splits' to form a double-peaked structure which is centred around the single-peak position (392 mA). For higher currents the structure gains an additional peak, forming a triangular arrangement (398 mA). However, this time the structure is not centred on the single-peak position, but there is a peak at this location. For higher currents still, the pattern gains a fourth (408 mA) and fifth peak (420 mA) but these are less well defined and the transition to a lasing pattern follows soon after. If the current is decreased again from this lasing

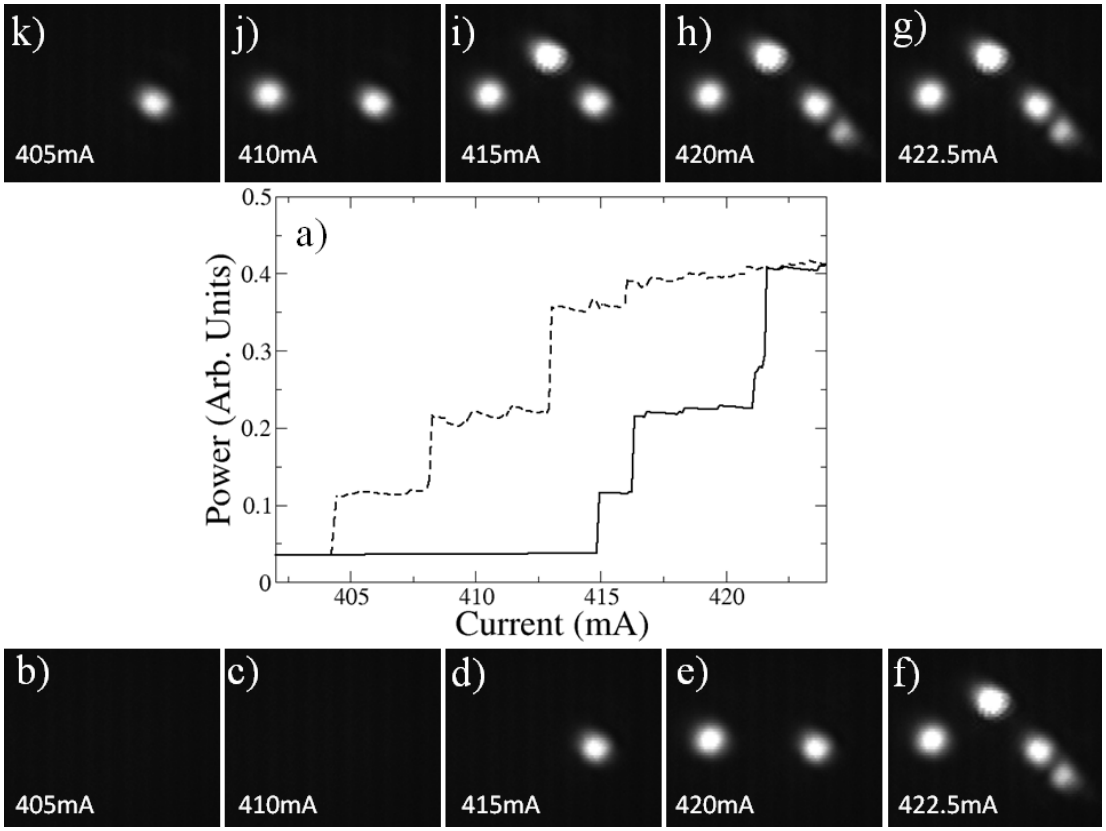

Figure 4.8: a) LI-curve for three spots. (b)-(f) Images taken for increasing current, (g)-(k) images taken for decreasing current. Produced and displayed in the same way as Fig. 4.5. The pictures are a spatially selected portion of the VCSEL aperture with size approximately 50 μm $\times$ 40 μm and the analysing polariser is set such that the shown spots were at maximum brightness.

pattern, we return to all previous patterns in reverse order. The LI-curve shows that it is not only the first, single-peaked state which is bistable but structures with multiple peaks are also bistable.

The majority of CS display some form of this splitting however in most cases it is not so ideal as previously shown. The CS evolution shown in Fig. 4.10 occurs on a defect line. When the VCSEL is lasing across the whole aperture, this defect line can be seen as bright and dark lines running parallel to one another and can be seen when the VCSEL is lasing over the entire aperture as seen in the upper left portion of Fig. 4.2p. It's origin is unclear but it seems to be an attractor for the spots. We can see from Fig. 4.10 that the splitting has a preference to

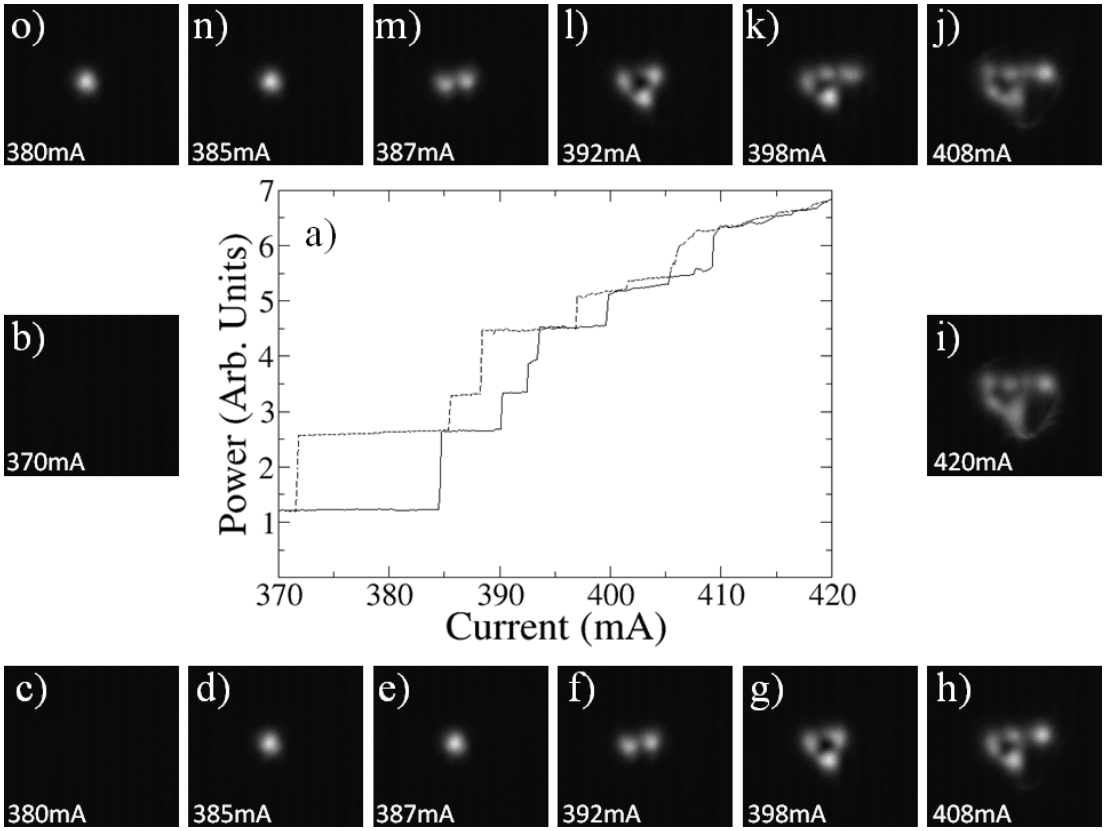

Figure 4.9: a) LI-curve for the CS with lowest threshold only. (b)-(h) Images taken for increasing current, (i)-(o) images taken for decreasing current. Produced and displayed in the same way as Fig. 4.5. The LI curve was created by spatially selecting only the area in the middle of the inset pictures and the extent of this spatial aperture can be seen in the inset picture (i). The analysing polariser is set such that the three-peak structure is at maximum intensity.

occur along the defect line. However, beyond the two-peaked state there are some weak structures off the line where we might expect the third peak of a triangular structure to appear.

4.4 Frequency

The optical linewidth of the spots can be measured using a Fabry-Perot interferometer (FPI). Measurements with an FPI with 10 GHz free spectra range produced resolution limited linewidths, and hence a confocal Fabry-Perot with

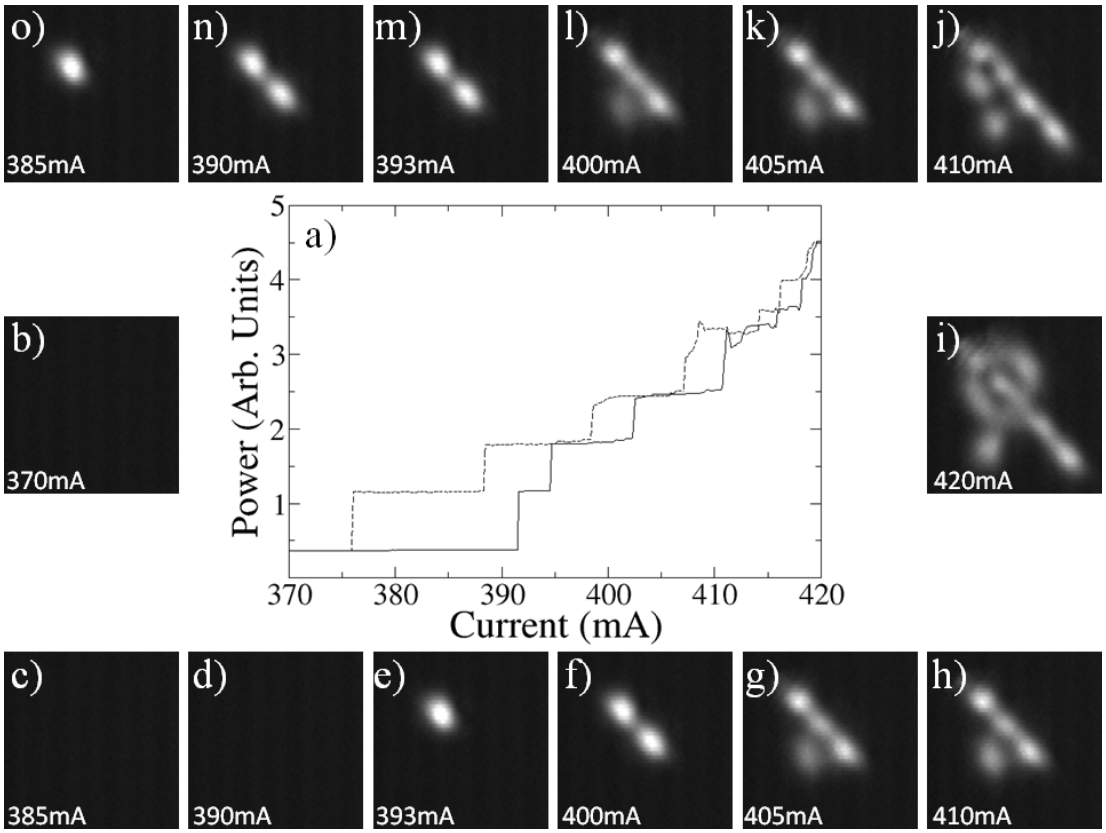

Figure 4.10: LI-curve for a CS known to lie on a line defect in the VCSEL. (b)-(h) Images taken for increasing current, (i)-(o) images taken for decreasing current. Produced and displayed in the same way as Fig. 4.5. The defect line runs from top left to bottom right in the inset pictures (see also the upper right corner of the full near field in Fig. 4.5). The LI-curve was created by spatially selecting an area only slightly smaller than that shown in the inset pictures. The analysing polariser is set such that the single-peak structure is at maximum intensity.

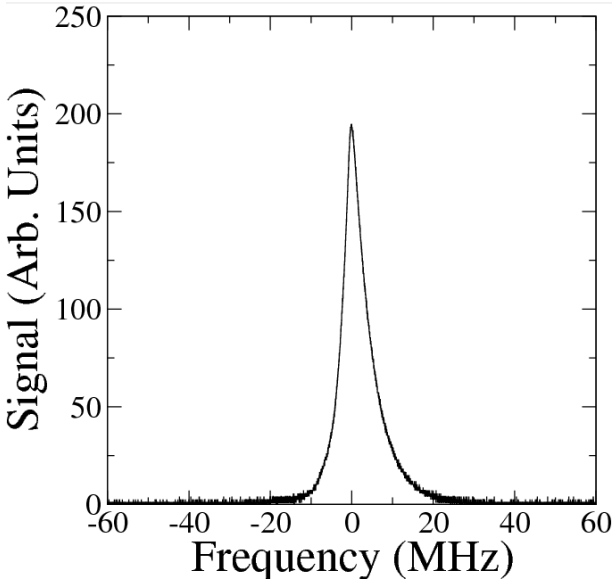

Figure 4.11: Frequency spectrum of a single spot just above threshold. Measurement taken with a high finesse Fabry-Perot interferometer with a free spectral range of 1 GHz.

1 GHz free spectral range (Toptica FPI-100) is used. The emission is found to be optically coherent with a typical linewidth of about 6 MHz when operating on a single longitudinal mode of the external cavity (see Fig. 4.11) which is comparable to typical linewidths found for grating controlled laser diodes. Hence the spots act like *micro-lasers*.

The spots are not limited to operating on a single longitudinal mode of the external cavity however, as multi-mode operation is also possible for specific values of the injection current. In general the spots are single mode, however tuning the current forces the spots to hop between external cavity modes and in the parameter region between these two modes there is a region of multi-mode operation. The phenomena and temporal dynamics arising from this multi-mode behaviour will be discussed in Sec. 6.

To obtain the absolute wavelengths of each spot an optical spectrum analyser (HP 86140) is used. The spectral resolution of peaks is only 0.07 nm, broadening the spectra of the spots however the absolute wavelength of the spots can be measured, making the measurement useful. The optical spectra of four spots just above their respective thresholds (Fig. 4.12) show that the frequency of spots at

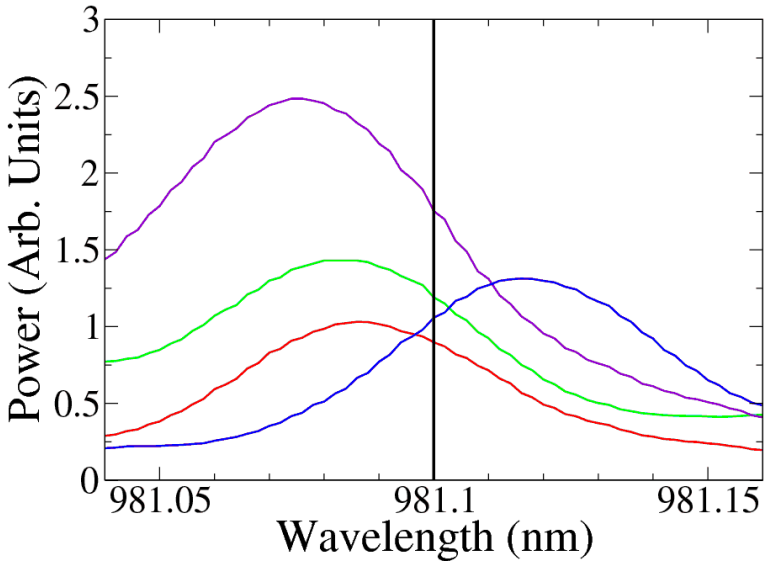

Figure 4.12: Optical spectra of four spots at threshold current. The vertical black line indicates the central reflection wavelength of the VBG. The spot denoted by the blue curve has the lowest threshold followed by red, green and finally purple. The resolution of the spectrum analyser is 0.07 nm, i.e. the width of the lines is an artefact.

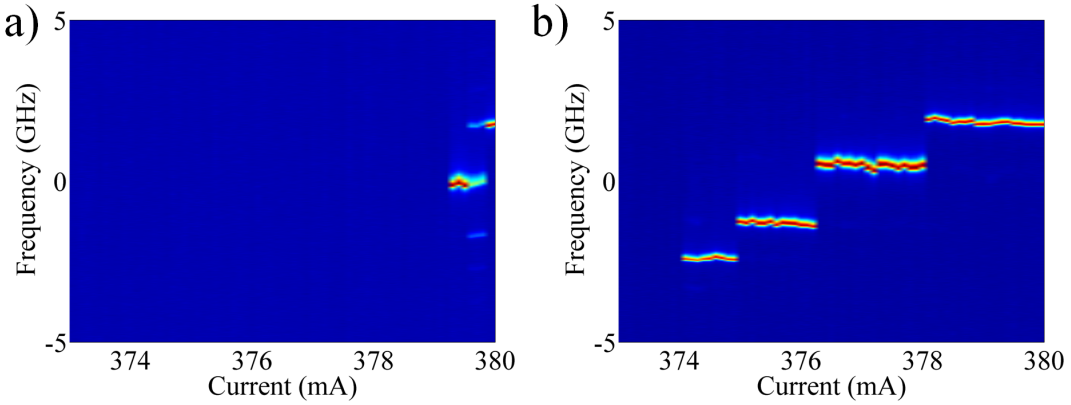

Figure 4.13: Frequency shift with a) increasing and b) decreasing current. Measurements taken at 0.1 mA intervals with a confocal FPI with a free spectral range of 10 GHz.

threshold is in general blue detuned to the grating frequency except for one of the spots.

The blue detuning to the grating wavelength is predicted by theoretical simu-

lations based on a model which takes into account all round trips in the external cavity and will be discussed in more detail in Sec. 4.6.

The frequency of the spots also shifts with increasing current, however the rate is much lower than the drift of the VCSEL cavity resonance (0.0003 nm/mA for the spots compared to 0.0035 nm/mA VCSEL cavity resonance). The decreased shift rate with current is consistent with experiments into grating controlled modes [56] and is also the key reason they utilise a VBG for high power laser stabilisation [44]. There is a continuous drift of the frequency as expected from Ohmic heating, but at some currents the external cavity mode which the spot is lasing on becomes unstable, and the frequency jumps to the adjacent external cavity mode. This behaviour is presented in Fig. 4.13. Two interesting effects arise from this hopping, there is a region close to the hop in which the spot becomes multi-mode (Fig. 4.13a) which causes temporal dynamics. The second effect is that for certain parameters, more than one spot can occupy the same external cavity mode and for narrow parameter bands this can lead to phase locking. Both phenomena will be explored at length, phase locking is explored in chapter 5 and temporal dynamics in chapter 6.

4.5 Classification as cavity solitons

Now that the basic properties of these spots have been established, we would now like to classify these spots as cavity solitons (CS). The criteria we impose is that they must be localised, bistable, independent and have a degree of mobility [2, 15, 119]. Locality is crucial to confirm that each spot is confined by nonlinearities and not boundary conditions. Likewise, independence ensures that these spots are not part of a larger pattern, and together with bistability make CS very desirable for applications. Mobility means that the spots are not fixed in place, and have some freedom to move in the transverse aperture. This property should exist for structures sustained by nonlinearities, and rules out the possibility that the spot is a transverse mode of the cavity. In an ideal system the spots can move to any position in the transverse aperture and have no preference for position. In reality the spots are somewhat pinned to their locations and this is believed to be due to a spatial variation of cavity parameters or 'disorder'. The CS are

attracted to the extremum of this disorder and hence we impose the somewhat relaxed condition that the spots are capable to move within the limits imposed by this disorder.

The spots used for CS classification are the subset of spots displayed in the insets of Fig. 4.8.

4.5.1 Locality and Bistability

The spots are clearly localised, circularly symmetric and – as stated above – of approximately equal size and shape indicating that their shape is dictated by nonlinearities rather than being imposed by boundary conditions or disorder. Bistability was demonstrated by increasing the current from below threshold to some upper limit, then decreasing it again until the intensity is at the level of spontaneous emission again, measuring the intensity in the system at each current value. The resulting LI-curve was shown in Fig. 4.8. At each point in the LI-curve between 404 mA and 422 mA the system has two distinct intensity levels for each current value, hence the system is bistable between states in which the spots are off, and states in which the spots are on.

4.5.2 Switching and Independence

The previous result that each spot has a unique threshold current for spontaneous switch-on is an early indication that they are independent since it rules out the possibility that they belong to some overarching patterned state as this state would switch as one. A more rigorous proof is demonstrated by switching individual spots on and off by application of the writing beam (WB, outlined in Sec.3.3) without altering the states of the other spots. The mechanism for writing will be discussed later, however it may be conjectured without prior knowledge that any process which switches a spot should be capable of lowering the switch-on threshold of that spot while the WB remains on. Thus if the WB is applied to the point at which the spot exists, and the threshold is shifted to lower currents then a study of the optimum frequency for switching may be undertaken.

The curve in Fig. 4.14 is created by measuring the threshold of a spot by plotting the LI curve. The WB is then switched on and placed on top of the

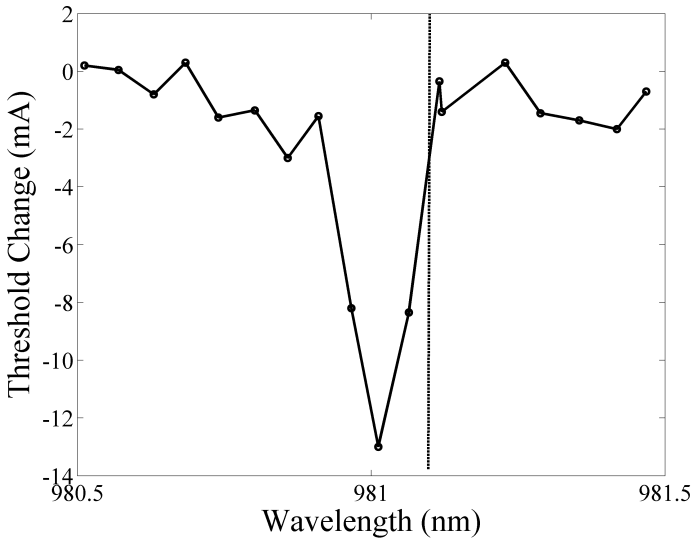

Figure 4.14: Curve showing the effective threshold reduction induced by a CW WB placed on top of a spot. The dotted line corresponds to the reflection peak of the VBG.

position where the spot forms and the LI curve is repeated. The WB is then turned off and the LI curve repeated for a third time. The thresholds of the two runs without WB are averaged to account for any drift incurred by macroscopic thermal fluctuations (See Fig. 4.4) and then compared to the threshold with the WB present. Fig. 4.14 illustrates the threshold reduction capabilities of the WB at frequencies in the range of the VBG reflection peak. Optimum threshold reduction is found for wavelengths which are 0.1 nm blue detuned to the grating wavelength. An offset can be explained since at the VBG reflection peak, essentially no light from the WB would pass the VBG. With this in mind one might expect that the threshold reduction would be equal on either side of the VBG reflection peak, however this is not the case and a preference for blue detuning is present. The reason for this preference will only become clear when the discussion of the switching mechanism is discussed in Sec 4.6. From this experiment it has been shown that threshold reduction and hence writing of spots is most efficient with the WB 0.1 nm blue detuned to the grating frequency, hence unless otherwise stated this is the wavelength at which all writing will be performed.

In order to prove independence of the spots, the WB should be used to switch

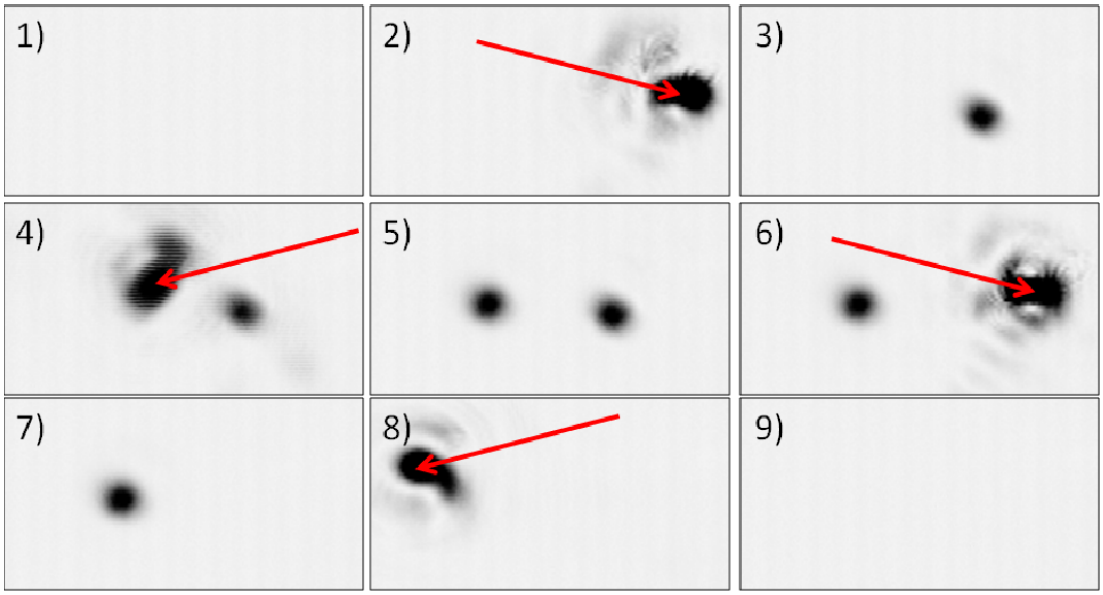

Figure 4.15: Near field intensity distribution in inverse grey scale, black denoting high intensity. The sequence shows the independent switch on, and then switch off of 2 spots using the WB. The arrows indicate the application of the WB. Time evolution follows the inset numbering.

the spots on and off. If this can be done to one spot, without effecting the other spots then this proves that they act independently. The system is biased at 410 mA, where the two spots with the lowest threshold in Fig. 4.8 are simultaneously bistable. Then the WB is applied in the sequence shown in Fig. 4.15. We see that we may switch one spot on by local application of the WB and that the spot remains on after the WB is removed. This is repeated for a second spot without affecting the state of the first spot. The spots are then switched off independently by placing the WB away from the peak of the spot.

If three spots are to be switched-on and off independently then three spots with overlapping bistability loops must be found and this is not typical. Therefore to achieve three spot switching the bistability loops of spots have to be shifted relative to one another. This is possible by inducing an external cavity misalignment by tilting the VBG. A typical result is illustrated in Fig. 4.16 for a VBG tilt of 1 mrad. In this way we can enter a situation where three CS are bistable for a fixed current, and thus may be switched independently. For three spots

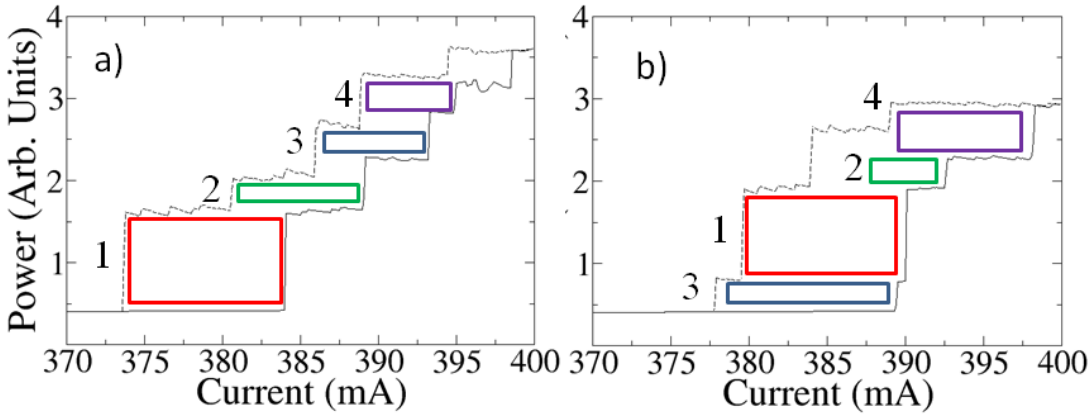

Figure 4.16: LI-curves with a)Optimum external cavity alignment and b) Misaligned external cavity. The numbered boxes represent the bistable loops for several spots.

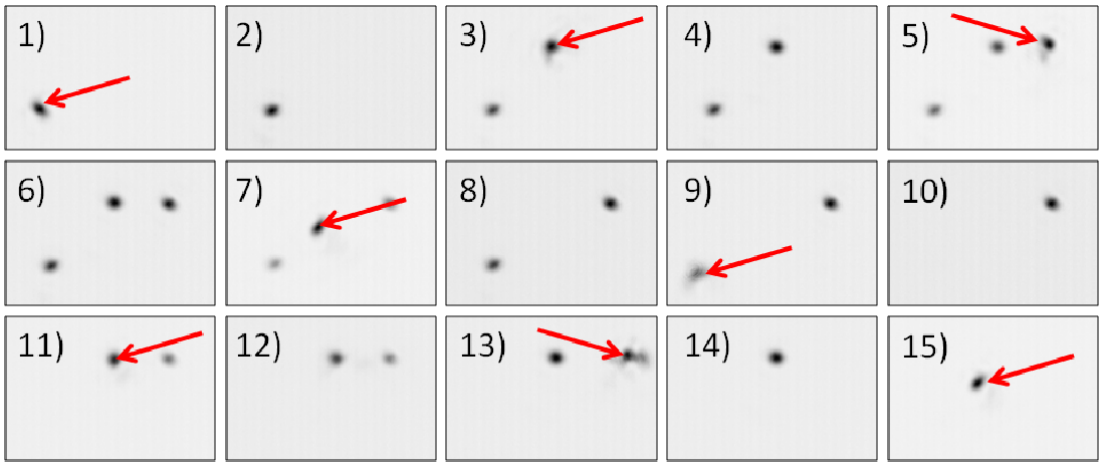

Figure 4.17: Near field intensity distribution in inverse grey scale, black denoting high intensity. Demonstration of the independent switch on, and then off of three spots using the WB. The arrows indicate the application of the WB. Time evolution follows the inset numbering. The preceding and following states are omitted but are the zero state.

there are now $2^3 = 8$ possible states we must demonstrate to rigorously prove independence and these are all shown in Fig. 4.17.

These demonstrations show that each spot can be switched on and off independently without affecting the state of the other spots. This is a strong indication that these spots are stabilised by nonlinearities, since a lasing spot or pattern

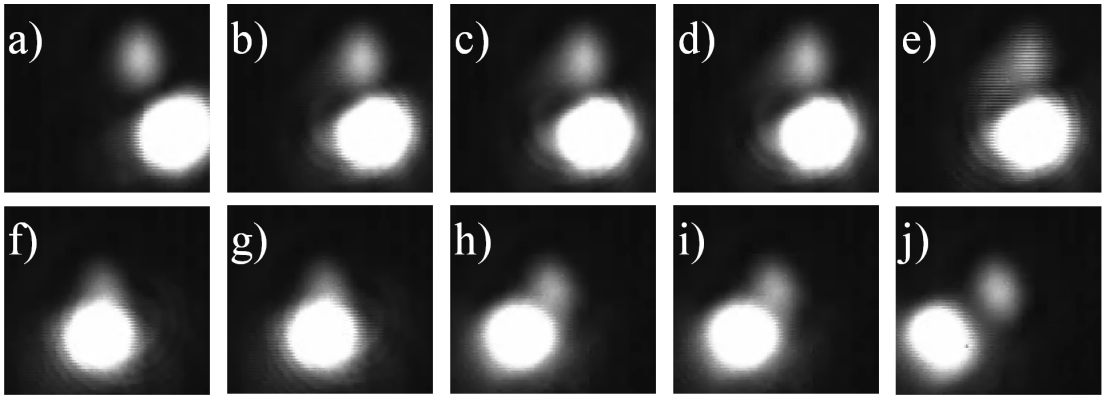

Figure 4.18: Storyboard showing the effect of passing the writing beam near spot number 4. The brightest spot is the WB and as the images progress it is translated to the left. The dimmer spot is spot number 4 and is shown to move under the influence of the WB.

which arises from boundary conditions (i.e. a cavity mode stabilised by the cavity mirrors) would be a global pattern and would switch on and off globally rather than locally.

4.5.3 Mobility

The final ingredient for a self-localised solution or soliton is that it can be positioned arbitrarily within a homogenous system, i.e. ideally anywhere within the pumped aperture [2, 36]. In other words, translation is a neutral mode of a CS. It is well known that real semiconductor devices contain spatial disorder [4, 15, 63, 89, 119], which lead to spatial variations of the cavity resonance across the device (gain variations also exist but are considered not to be so important). The CS couples to all these perturbations of the translational symmetry and drifts until it reaches a 'trap', i.e. a local extremum of the perturbation 'potential' in which the coupling to the odd neutral mode vanishes [36, 107]. This explains why in our – and all other known [12, 15, 119] – implementations of CS in semiconductor devices, the CS are pinned at certain positions. They can be dragged out of these traps to some extent by applying other perturbations, e.g. via the WB or modulations of the holding beam [89, 127], thus demonstrating some mobility.

Relocation of the spots by the WB works also in the scheme investigated here

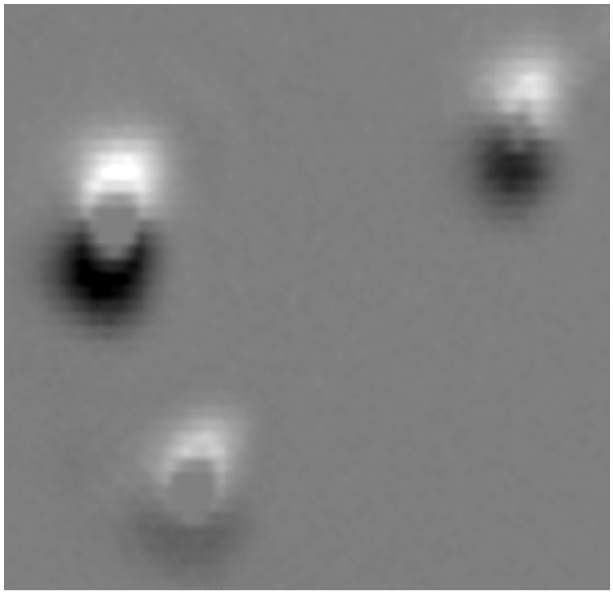

Figure 4.19: Shift of three spots with tilting of the VBG by 1 mrad. 'White' shows the position of the spots for optimum cavity alignment, 'black' for a misaligned cavity. The greyish parts denote overlap. The width of the black and white sections are given by the soliton width, i.e. approximately 10 μm.

and is demonstrated in Fig. 4.18. This figure is achieved by placing the WB to the right of the spot and slowly translating its position via a steering mirror tilt. When the WB comes close to the spot, the spot moves down towards the WB until it becomes hard to resolve the two beams. After the WB leaves the spot, they decouple and the spot is once more stable.

Another method to display the mobility of the spots is to show that the spots move under a tilt of the feedback. Investigation of the near field of the VCSEL while the VBG is tilted shows that the spots shift in response to the tilt. Fig. 4.19 illustrates the effect for the same conditions as the tilt induced to produce Fig. 4.16. In tendency, the spots are shifted in the direction of the tilt, but, as can be seen from the different displacements shown for each spot in Fig. 4.19, by a different amount. A straightforward interpretation is that the two upper spots reside in a 'shallow' trap, allowing them to move over a larger distance for a given perturbation than the one in the lower part, which seem to exist in a more 'strongly confining' trap.

The spots' ability to move means that they have a degree of mobility and

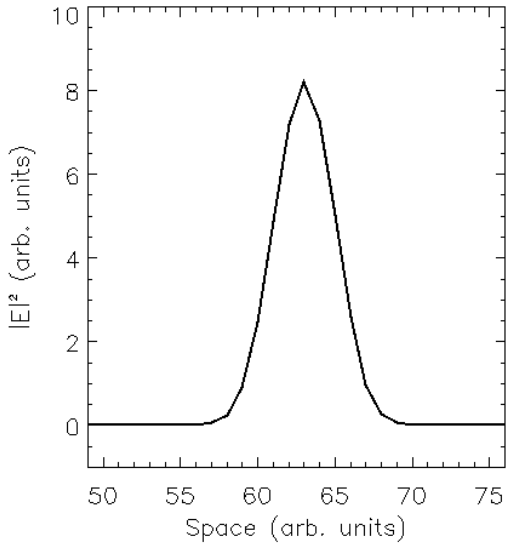

Figure 4.20: Intensity profile for a localised structure in the 2D numerical simulations. Figure courtesy of Craig McIntyre (University of Strathclyde)

therefore fulfil the final criteria to be classified as cavity solitons. Since they appear in a laser system and have properties unique to lasers, they will henceforth be referred to as laser cavity solitons (LCS).

4.6 Discussion

The spatial properties of the LCS found in this system are very similar to those seen previously in the CSL with feedback from a diffraction grating [127] in both size and shape. The widths of all LCS are very similar and should differ only due to the underlying spatial disorder on which each LCS lies. The shape is reasonable well fitted by a Gaussian, however it should be noted that this fit is not perfect and indeed there is no prior knowledge which would suggest a Gaussian shape.

Numerical simulations have also been performed for a VCSEL with feedback from a VBG using the model outlined in Sec. 3.5. Self-localised spots were found in both 1D and 2D [108] with lineshapes and sizes which match well to those found experimentally. One such profile created using the 2D model is shown in Fig. 4.20 however may appear more peak-like due to undersampling of the data.

The wings of this profile match very well to the experiment however in contrast to experiment, come to a sharp point at the peak. Structures with multiple peaks have not yet been investigated in this model however.

Though the splitting behaviour for each LCS is unique for each LCS, certain similarities can be noted. In Fig 4.9 and Fig. 4.10 both cases show that the CS has a tendency to split from a single peak via a linear double-peaked structure to a triangular triple-peaked structure. A phenomenologically very similar sequence is found in an optically pumped vertical-cavity amplifier [13]. Similar structures are also found in a CSL based on two face-to-face VCSELs [40, 42] and the behaviour in this system is very similar indeed. There, the first structure to cross threshold is the three-peaked structure which is not seen in the VBG system, however for decreasing current this three-peaked structure transitions through the double-peaked and single-peaked structure in a way which closely resembles the behaviour seen in Fig. 4.9. Ring-like structures are also found in the system with face-to-face VCSELs which are found to act as a phase vortex via an interferometric measurement [43]. Ring-like structures are also possible in the VBG system, however no interferometric measurements have yet been undertaken, and thus should be the focus of future investigations.

When considering the origin of multi-peaked structures it is tempting to speak of high-order solitons or clusters of solitons. Indeed the powerful theory of 'homoclinic snaking' predicts that clusters of closely packed CS with different numbers of peaks should coexist with the single-peaked solution [21, 29] and all solution branches are interconnected in a complex way. However, there are several problems with this interpretation. First, the mathematical argument for homoclinic snaking is formally only valid in one spatial dimension [21, 29] though simulations show that this is not an issue in reality [72]. Second, if all clusters are essentially simultaneously bistable, one should not see the spontaneous formation of a sequence of spots with increasing order if the pumping parameter is increased, but the system should stay in the non-lasing state until the threshold for pattern formation is encountered. Nonlocal coupling, e.g. via temperature fields, was recently suggested [38] as a possible mechanism for 'slanting' the snakes and producing the interwoven but displaced hysteresis loops observed in [13] (and here). Finally, and very importantly, there are theoretical arguments to expect that the

conditions for homoclinic snaking, in the formal sense [29], do not apply to lasers due to the phase symmetry.

Indeed a simplified model of a VCSEL with FSF [85], reports a bifurcation diagram for a 1D laser CS which begins and ends at the 'off' state, with no direct connections to multi-peaked structures. In view of this result it is surprising that the hysteresis loops of single laser CS to clusters observed here are quite similar to the ones observed in amplifier systems, which are expected to show snaking [13]. One possible explanation is disorder, possibly in both cases, i.e. these clusters are manifestations of higher-order solitons or soliton interactions, modified by the inhomogeneous background they reside in.

The spots were found to be bistable for certain parameters and the range of parameters over which this bistability exists (bistable range) is typically higher than in the diffraction grating system and similar to that seen in the face-to-face VCSEL system. The bistability in the VBG system arises from the ability for the VCSEL to remain lasing stably for two separate configurations of its carriers, made possible by the positive α-factor [55]. The α-factor (or alternatively linewidth-enhancement factor) was first introduced to account for linewidth enhancement in semiconductor lasers, since the earlier analysis of Shawlow and Townes did not correctly predict the linewidth of semiconductor lasers. It relates the carrier density to the refractive index and the VCSEL which is used has a positive α-factor, i.e. higher carrier density leads to lower refractive index.

When the LCS is in the off-state and the VCSEL emits only spontaneous emission the carrier density is high leading to a low refractive index via the positive α-factor. However if this state is perturbed such that some carriers are removed the refractive index will increase, shifting the cavity resonance. If the cavity resonance is shifted towards the feedback frequency then more carriers will be removed as stimulated emission due to increased feedback. This causes a positive feedback loop which cascades towards a lasing state which is supported by feedback. This state is not stable over the entire aperture of the laser however and is confined to a self-localised lasing spot i.e. an LCS. Crucially however, when this stable lasing condition is met, the low amplitude background state is still stable and this gives the LCS their bistable nature. The mechanism of localisation is not explicitly established in theory but the most convincing mechanism is that

self-focussing leads to a lensing effect within the non-linear medium and this lens creates a stable cavity within the plano-planar VCSEL resonator (see Fig. 2.3b) [1].

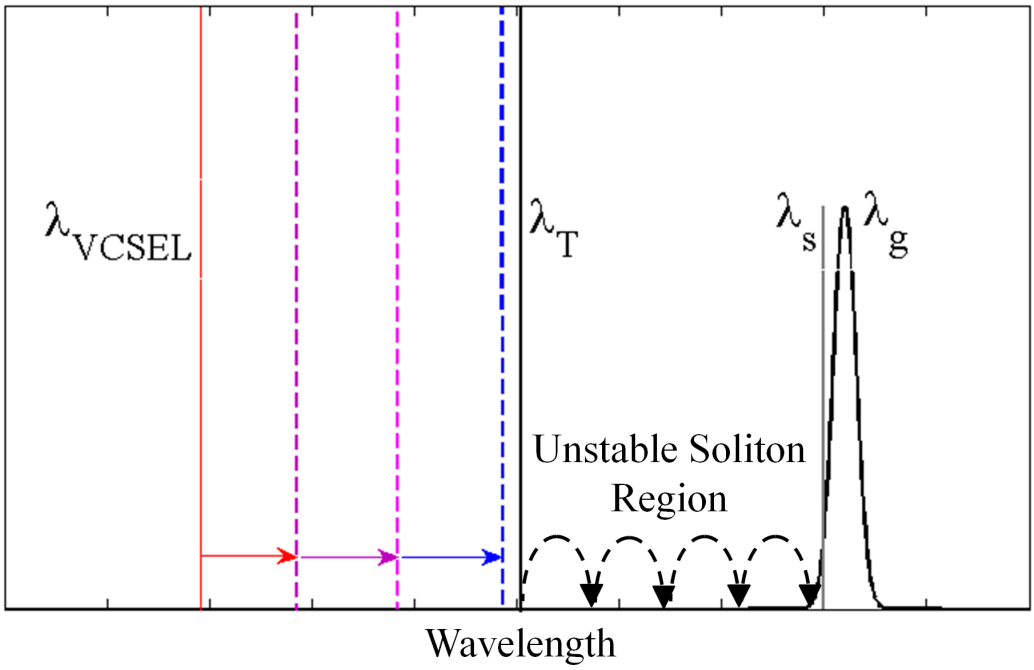

Figure 4.21: Schematic diagram of the proposed CS switching mechanism. λ_g is the central reflection wavelength of the volume Bragg grating, λ_s is the final wavelength of the stable CS, λ_T is the threshold wavelength and λ_{VCSEL} are the cavity modes of the VCSEL. Wavelengths are only included for rough visualisation and are not accurate.

This mechanism to support bistability also gives an indication of the mechanism for switching, and the conditions for switch-on threshold. The current interpretation of the mechanism which dictates the threshold of the LCS is schematically outlined in Fig. 4.21. In the sketch the grating wavelength λ_g is fixed. The so-called 'cold-cavity' VCSEL resonance is initially situated at the leftmost solid line. Applying current to the VCSEL heats the cavity via Joule heating. This results in the cavity resonance wavelength red shifting, along the straight arrow in Fig. 4.21. The red shift brings the VCSEL modes closer to the grating wavelength, hence increasing feedback, lowering the losses. When the resonance reaches a critical point, marked λ_T on Fig. 4.21, the VCSEL attempts to begin

lasing. Lasing across the whole aperture is not stable in this regime however, and filaments are formed which self-localise via nonlinearities to an LCS. The blue most wavelengths are not stable solitons either however and in this region (marked unstable soliton region on Fig. 4.21) the wavelength cascades through multiple unstable modes until the LCS finally reaches a stable mode which is slightly blue detuned to the grating wavelength.

The LCS were indeed found to have a spread in emission wavelengths which were in general blue detuned to the grating reflection peak. This blue detuning matches the behavior of the previous scheme in [119]. The fact that the spots are not fixed to a certain wavelength can be partially attributed to the fact that operation on different longitudinal modes of the external cavity is possible within the bandwidth of the VBG. In addition, the spatial disorder mentioned earlier is expected to play a strong role. These spatial inhomogeneities are thought to cause the local resonance of the VCSEL cavity to vary across the aperture of the device, forming traps or ridges [15, 88, 119] and producing a spatially varying wavelength distribution for the spots. Systems which rely on injection of an external, large area holding beam (HB) to stabilise bistability [12, 15, 122] do not display this freedom of frequency as all CS are frequency locked to the holding beam. It is perhaps not surprising that the spots can choose their own frequency in this system since it is a laser system, and the frequency, and also phase, are decided not by external parameters but rather by local parameters of the laser itself.

The mobility of the LCS leads to some interesting questions since in the ideally homogeneous system, any tilt should lead to a drift until the spot is swept to the perimeter of the device. For spatially extended patterns, a detailed investigation of the locking or pinning of the self-organised pattern in a potential minimum in spite of a tilt was performed in a nonlinear feedback scheme [3, 111]. There it was found that above a certain threshold tilt the patterns unlock and start to drift. Here, we observe that the spots seem to disappear at some critical tilt angle (using temporally integrated detection over ms as typical for normal CCD-cameras). It would be extremely interesting to explore by spatio-temporally resolved detection whether there is a regime of drift [88, 127] or whether the spots really cease to exist immediately after unlocking.

It should also be noted that the above model also explains why spots can be switched off by injection beside their location. The likely scenario is that the WB perturbs the trap and attracts the spots. If the 'landscape' of the perturbing frozen disorder is shaped suitably, the spots can't return to the trap after the switch-off of the WB. Indeed, the direction of the side with the easiest switch-off relative to the location of the spots varies between different spots. This is expected for a system in which some random disorder is added onto a situation with, in principle, rotational symmetry. By 'stirring' the WB across the aperture of the VCSEL, several spots can be switched on, switched off and dragged around in an irregular manner illustrating this reasoning. As far as information is available [41, 42], the main regularities of these findings are matched by the ones in face-to-face coupled VCSELs, which are also quite isotropic. In contrast, with frequency-selective feedback from a diffraction grating the orientation of the grating breaks parity and a well-defined preference for up/down-switching is established [119, 127].

Chapter 5

Consequences of phase freedom

As stated earlier each LCS has the freedom to choose its frequency, and therefore phase, independently. Since the LCS are essentially independent micro-lasers it is interesting to consider whether these oscillators may lock in phase through non-linearities. The complexity of the situation is enhanced by spatial disorder, i.e. small variations of parameters, most importantly cavity length, over the aperture due to device imperfections. In a completely homogenous system one would expect their frequencies to be the same (being given by the longitudinal cavity mode with the highest net gain) or at least confined to a few discrete frequencies defined by the comb of longitudinal modes. The spatial disorder leads to a pinning of the LCS at certain locations within the transverse aperture (a self-localised state in a homogeneous system could exist anywhere) and to a spread in frequencies (see Sec. 4.4)[119, 129]. These results are in line with findings in a CSL based on a VCSEL with saturable absorption, where independent LCS were found to be incoherent [40]. It seems to be a very interesting question to ask whether this is indeed a fundamental feature or whether self-localised states can show frequency and phase locking behavior even in spite of this spatial disorder which seems to conspire against such effects. If locking were found it would be advantageous for overcoming the aforementioned spatial disorder in LCS arrays as it would provide a mechanism to synchronise all of the spots to the same frequency and phase parameters allowing for easier methods of control.

Furthermore, the previous setup with the diffraction grating [119], the polarisation direction of the CS was fixed due to the strong anisotropy of the diffraction

grating. The diffraction efficiency of the VBG is in principle isotropic, except for a small effect arising from a small tilt of the grating planes to the normal of the substrate. The intra-cavity beam splitter provides another source of a small anisotropy. These two factors provide only weak polarisation control however and thus it is interesting to study the polarisation behaviour of the LCS.

A demonstration of frequency and phase locking is presented in the next section and the effects arising from the freedom of polarisation are presented in Sec. 5.2

5.1 Phase Locking

The cavity soliton laser setup used for the locking investigation is the setup shown in Fig. 3.9 with the addition of the Fabry-Perot interferometer outlined in Sec. 3.4.3. The cavity length used is the 'long cavity' (see Sec. 3.2.2 for details), without intra-cavity polariser.

As indicated previously, the LCS typically have different frequencies and can operate on single or multiple external cavity modes (Sec. 4.4) [119, 129]. Previous investigations on locking established that there are two main parameters: coupling strength and detuning [58, 75]. In the current stage, there is no explicit handle on the former in this system but the detuning can be influenced by minute tilts of the VBG, similar to the micro-chip laser experiments [58, 75] (see below for details). One other influence on the frequencies is the injection current via Joule heating.

By a suitable adjustment of these parameters, the situation illustrated in Fig. 5.1 can be created. The two LCS have the same peak frequency (Fig. 5.1), within the accuracy of the measurement. Taken in isolation, both LCS have Gaussian-like profiles in both near and far field.

However, if the aperture is enlarged such that both are simultaneously detected, we obtain the results shown in Fig. 5.2. The frequency spectrum and near field image are simply combinations of each individual LCS. However the far field image in Fig. 5.2b shows fringes with a visibility of 1. It should be noted here that these fringes occur only for specific parameters and in general there are no fringes. The spacing of the fringes in far field, 9.9 mrad, should correspond to the

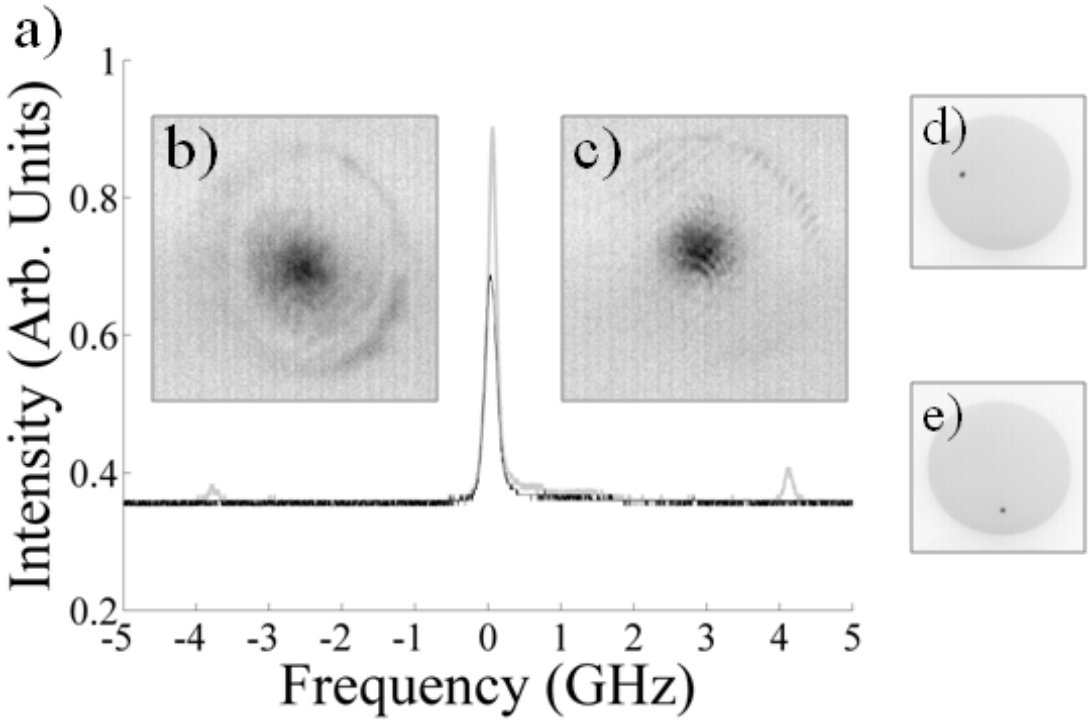

Figure 5.1: a) FPI spectra for two LCS when taken in isolation. The black trace corresponds to the images in (b) and (d) and the grey trace corresponds to the images in (c) and (e). Images (d) and (e) are near field (real space) images of the two LCS taken in isolation. In order to emphasise the device boundaries, an image of the spontaneous emission of VCSEL below threshold is superimposed. (b) and (c) are far field (Fourier space) images of the LCS taken in isolation. Black corresponds to high intensity. I= 405 mA. T=80 °C.

interference of two sources which are spatially separated in near field according to;

$$a = \frac{\lambda k_0}{k} = \frac{\lambda}{\theta}, \tag{5.1}$$

where a is the separation of the interference sources in near field, θ is the angle between the interference fringes and k and k_0 are the wavevector of the fringes and fundamental optical wavevector respectively. This calculation yields a near field separation of 99 μm for a 9.9 mrad fringe separation which agrees well with the measured LCS separation of 95 μm, and hence the fringes are interpreted to be due to the interference of the two LCS. Observation of interference fringes

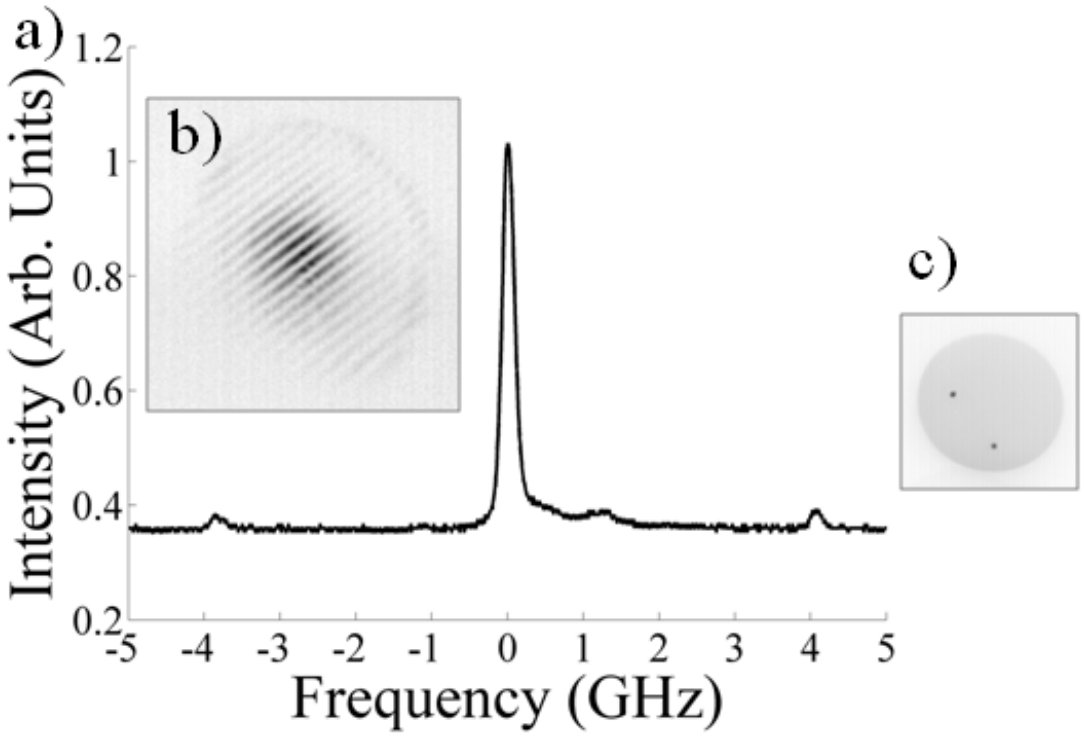

Figure 5.2: a) FPI spectra for two LCS, (b) far field intensity distribution, (c) near field intensity distribution. All data treatment like in Fig. 5.1.

requires the phases of the two LCS to be in synchronisation at least for the duration of the exposure of a CCD image (20 ms; it is actually stable over minutes and hours), however, the system is known to show small frequency shifts due to some temperature drifts on the time scale of seconds to minutes. Hence we conclude that there must be a phase locking mechanism ensuring a constant phase relationship.

5.1.1 Locking Dynamics

The characterisation of the locking behavior of two other LCS during an upward scan of the current are shown in Fig. 5.3. The modulation depth is calculated by fitting the data to a Gaussian envelope modulated by a sine wave, and takes the form;

$$y = y_0 + Aexp(\frac{-(x-x_0)^2}{2\omega^2}) \times \frac{(1 + Msin(F(x-x_0)+P))}{1+M} \tag{5.2}$$

where y_0 is the y-offset, A is amplitude, x_0 is the peak centre, ω is the width, M is the modulation depth, F is the frequency of the sine modulation and P is its phase. The centre can be known by inspection of the two separate far field peaks, so is fixed. So too is the frequency since this only depends on the distance between the LCS in near field, which is essentially constant over the course of the fitting.

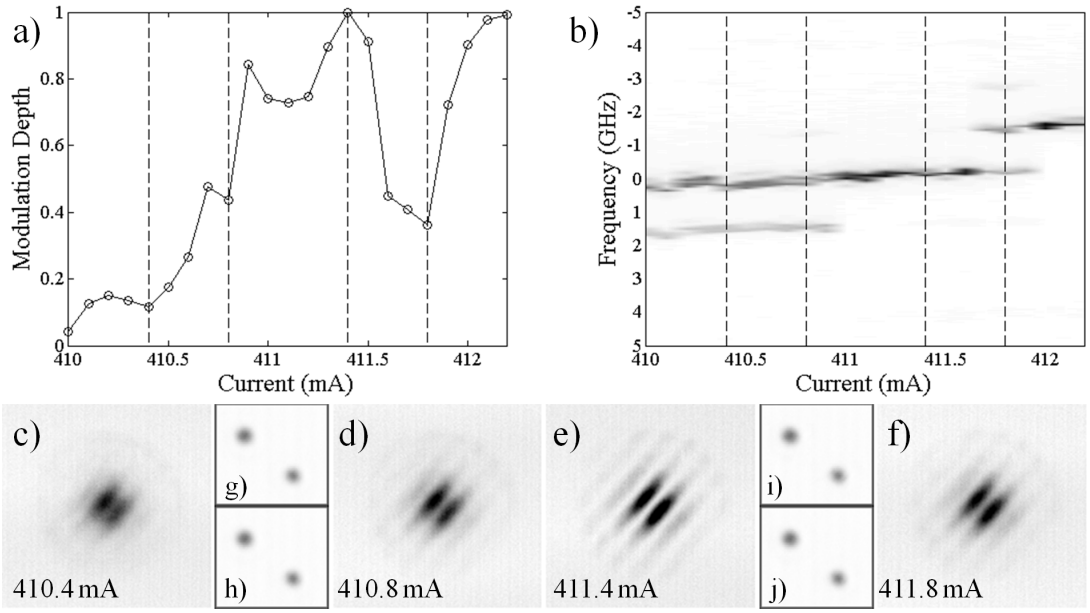

Figure 5.3: a) Evolution of the modulation depth (visibility) of the interference fringes seen in the far field plane of two LCS. b) Evolution of frequencies with increasing current for two LCS, measured with the FPI. c) - f) Far field intensity distributions for two LCS at different currents (values indicated in the inset and also indicated by dotted lines in (a) and (b)). g) - j) Near field intensity distributions of the far field intensity distributions shown in (c) - (f).

At low currents ($I \leq 410.4$ mA) the LCS occupy different external cavity modes (Fig. 5.3b) and there is very weak modulation of the far field. As the current is increased fringe visibility in far field increases sharply (Fig. 5.3d) as the phases of the LCS lock via their overlapping frequency side-modes. Note that the near field images are not affected in a discernable way (Fig. 5.3g - j).

Increasing the current causes one of the LCS to destabilise, inducing a jump to an adjacent external cavity mode. The two LCS now occupy the same external cavity mode which allows complete locking, leading to full intensity modulation at 411.4 mA (Fig. 5.3e). Increasing the current still further induces another LCS destabilisation, resulting in the weakening of far field fringes once again (Fig. 5.3f) as the locking is via the weaker side-modes. A similar scenario with a transition to complete locking occurs then at the next external cavity mode (Fig. 5.3a, b, 411.8 mA - 412.2 mA).

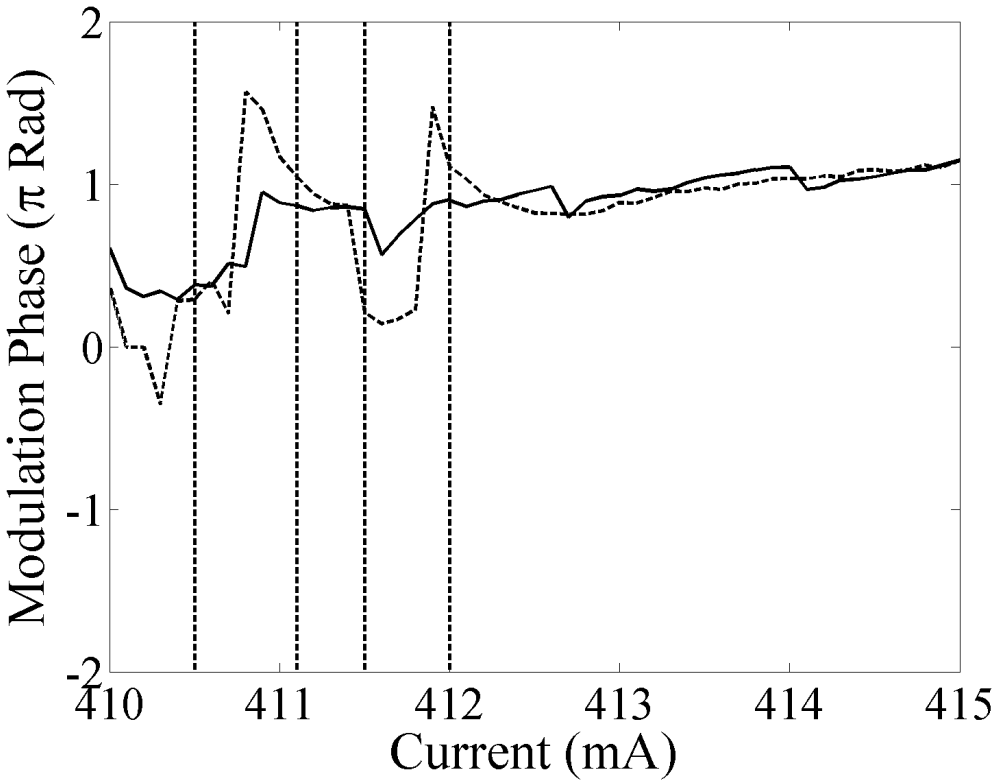

Figure 5.4: Evolution of the phase parameter with current which is obtained using Eq. 5.2. Solid line represents increasing current, dashed line represents decreasing current. Dotted vertical lines correspond to the same points as is in Fig. 5.3

The fitting procedure also produces the dynamics of the phase between the two LCS. Fig. 5.4 shows how this phase varies with current, for the same realisation as Fig. 5.3 but for a greater range of currents. It should be noted that the

modulation depth associated with currents above 412 mA is essentially 1, and that this corresponds to a constant phase difference of π between the LCS, i.e. they lock out-of-phase. The phase is less well defined when the modulation depth is low however and many phases are possible for low modulation depths. There is however a strong correlation between high modulation depth and a π phase shift, which suggests that these two particular LCS in tendency lock out-of-phase.

It should be noted here that if the same procedure is followed as that in Fig. 5.3 but for decreasing current, the dynamics are slightly different, i.e. there is hysteresis in the modulation depth. This should be related to the hysteresis seen in the frequency as the mode jumps appear for different currents. This is noted here, but was not investigated in depth and should be the studied in more detail in future work.

5.1.2 Discussion

The behavior described can be understood qualitatively by the fact that each LCS can operate on a comb of several longitudinal modes but these combs are usually displaced with respect to each other due to the disorder in the VCSEL cavity. This displacement can be tuned by a tilt of the VBG. The minimal threshold mode within the comb will also be different between different LCS due to disorder. Changing the current tunes the frequency of each LCS via Joule heating (within our measurement accuracy all LCS shift at the same rate of 0.00045 nm/mA). The tuning is continuous as long as the LCS stays on the same external cavity mode. At some point, this mode is destabilised and there is a frequency hop to another external cavity mode [77, 108]. If this mode is sufficiently close to the main operating mode of the other LCS, they can lock. This is expected to occur only in small parameter range. Indeed a tilt of the VBG of the order of a degree - corresponding to a frequency shift of about 3% of the free spectral range of the external cavity (for LCS 95 μm apart like in Fig. 5.2) is sufficient to go from complete locking to partial locking. This corresponds to an angular tilt of about 0.14 mrad, i.e. only some 10^{-3} of the angular width of an LCS. Indeed no change of the structure in near and far field is discernible for the single LCS

and the only effect seems to be on the frequency. This is in line with the microchip laser experiments, where the tilt of the cavity end mirror is used to control the detuning [58, 75]. Following this argument, it is probably not surprising that locking of three LCS is rare but possible leading to the beautiful rhombic interference pattern seen in Fig. 5.5.

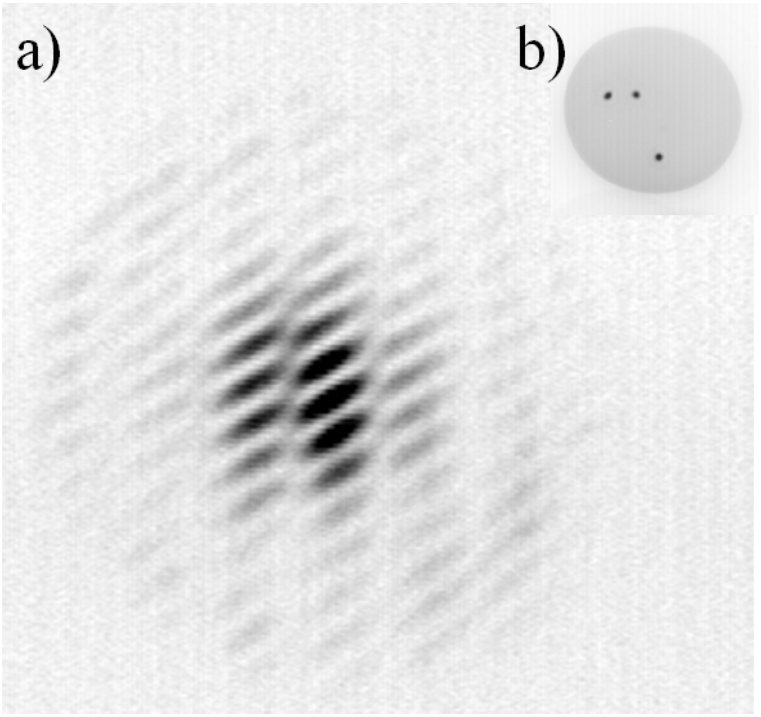

Figure 5.5: Near (b) and far (a) field intensity distributions for three LCS which are locked in phase. The VCSEL aperture (200 μm diameter) in (b) is superimposed for clarity of position and separation. Black corresponds to high intensity.

It should be stressed that the behavior illustrated in Fig. 5.3 is only a particular example. It is equally possible that the LCS are completely incoherent (visibility 0) as can be expected if disorder plays a role. Nevertheless, the locking is robust and reproducible (within one experimental campaign) if the correct combination of parameters is found. Scanning the current up and down, indications for hysteretic behavior in frequency as well as visibility are obtained. An exploration of these – expected – phenomena is interesting, but demands further systematic and detailed investigations. We mention a profound difference to the microchip laser experiments [58] which is that out-of phase locking is not the only

option but in-phase locking is also possible as in Fig. 5.6. The tendency to out-of-phase locking is normally due to the fact that there is no inversion in between the microchip lasers and hence a nodal line minimises losses, a restriction which does not apply to the CSL where the whole aperture is pumped homogenously.

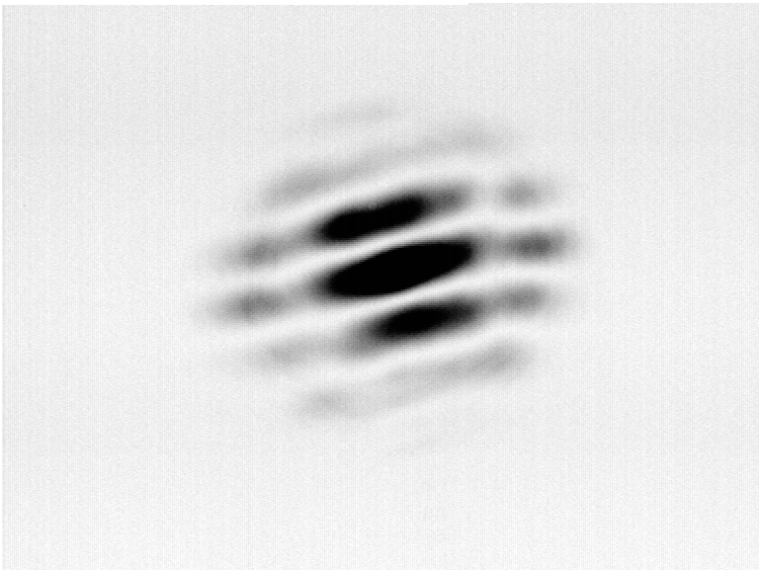

Figure 5.6: Far field intensity distributions for two LCS which are locked in phase. Black corresponds to high intensity.

The mechanism for locking of parameters between two cavity solitons is not well established. The main candidate appears to be that there is some interaction between the LCS through their evanescent tails. The appearance of weak near field fringes between two LCS has been observed in several cases to corroborate this and one such example is shown in Fig. 5.7. Most of the LCS where phase locking is observed are also at a mutual distance of a few beam radii, where phase locking is observed also in micro-chip setups [58, 75]. The LCS in Fig. 5.2 demonstrate though that phase locking can occur also at larger separations (about 18 beam radii) although it is found to be very sensitive and demands a precise alignment to assure a small detuning, as indicated above. A second explanation may be due to long range coupling of LCS arising from cavity length misalignment away from the self-imaging point, however, initial studies suggest that for such long range coupling, the cavity length would have to be grossly misjudged, which

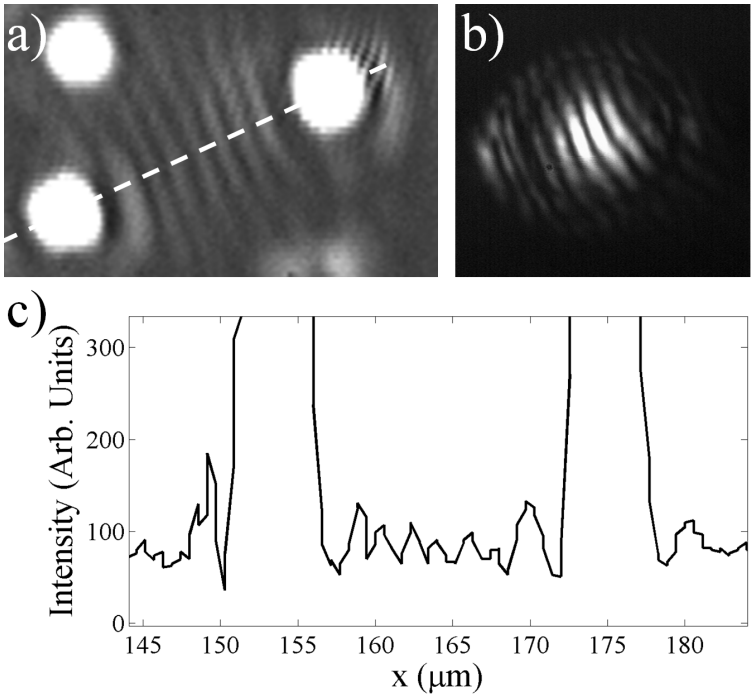

Figure 5.7: Near (a) and Far (b) field intensity distributions for two LCS which are locked in phase. White corresponds to high intensity. The image in (a) has been digitally enhanced to increase the contrast of the fringes. c) Intensity profile along the white dotted line in (a).

is not the case.

Since the spatial disorder fixes the initial detunings, we currently do not have a recipe to induce full phase locking at will except the global handle of alignment, instead we need to search parameter space to find a suitable situation. However partial locking is common. First results on homogenisation of the device response by spatially modulated injection of an external beam leading to a change the refractive index via the carrier density [130] is discussed in Sec. 7.2 and might pave the way for an at least partial control of disorder.

The interaction of propagating spatial solitons in conservative systems is known to be phase-sensitive and at the origin of a wealth of intriguing phenomena of spatial dynamics [115]. However, the phases are fixed by the launching conditions. The long term vision of the research on CSL is the realisation and the study of the interaction of a complex network of self-sustained oscillators which

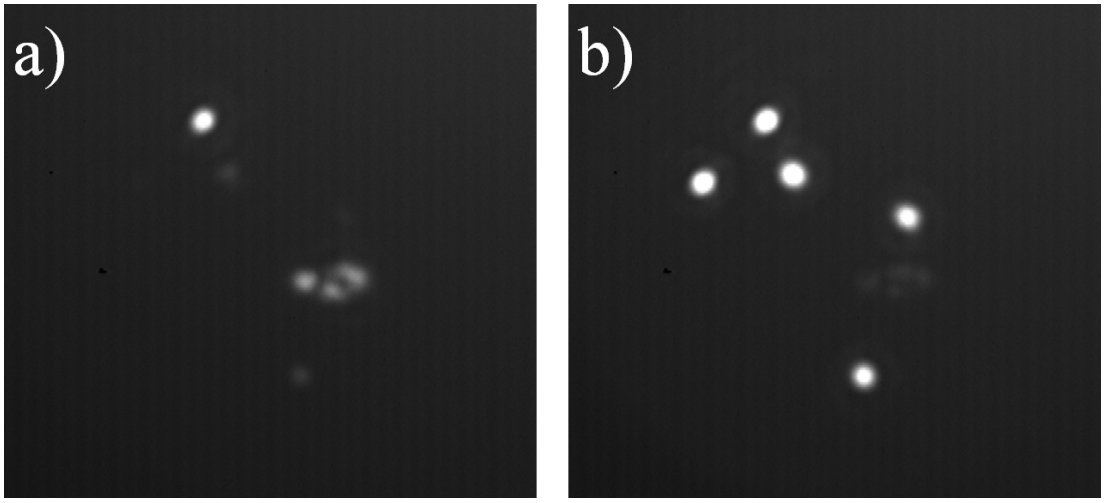

Figure 5.8: Pictures illustrating the effect of rotating the detected polarisation. a) Near field image of several LCS where the detected polarisation minimises the intensity of the upper LCS. b) Same system and parameters as in (a), however the detected polarisation has been turned to maximise the upper LCS.

have freedom of choosing frequency, phase (possibly polarisation) and location simultaneously [123, 125].

5.2 Polarisation Properties

The first indication of interesting polarisation effects came when the different polarisation components were analysed via adjustment of the half wave-plate before the optical isolator (see Fig. 3.9). If all LCS were identically linearly polarised then the effect of the half wave-plate rotation would be to alter the detected intensities of all spots by an equal amount. It was observed however that upon rotating the detected polarisation state, each LCS reached maximum transmitted intensity for a different angle of rotation. This is displayed in Fig. 5.8, where the same system and parameters are shown twice for different rotations of the half-wave plate controlling the detected polarisation.

The effect looks very drastic in Fig. 5.8 however the difference in polarisation angles is exaggerated by the anisotropic Fresnel reflection of the uncoated glass plate used to couple light out of the cavity. The nature of the reflection

results in approximately 1% of light polarised parallel to the table (referred to as horizontal polarisation) being outcoupled, while approximately 10% of light polarised perpendicular to the table (referred to as vertical polarisation) is outcoupled. This effect will act to amplify any polarisation differences, however the difference is still there, and in this section the polarisation states of the LCS will be investigated.

5.2.1 Polarisation Properties of LCS

The first investigation was to measure the polarisation angle of each LCS without additional intra-cavity polarising elements using the method outlined in Sec. 3.4.4 with $\theta = 0$ corresponding to polarisation parallel to the table and positive angles following the anti-clockwise convention. The first column of Table 5.1 shows the polarisation angle θ at threshold and it is clear that each LCS has a unique polarisation angle. The angles of the LCS are all within 12 ° of each other except for the first LCS, which has a significantly different angle. Fig. 5.9 shows how the average polarisation angle of the whole system (i.e. the polarisation angle calculated using spatially averaged I_x and I_y) changes as the current is scanned up and then down. It can be seen that after the first LCS switches on there is a small polarisation angle around 20 ° followed by a drop at 395 mA, at the splitting of the LCS. There is then a sharp increase to 32 °, followed soon after by another jump to 38 ° which coincide with the appearance of a further two LCS. These findings are expected from Table 5.1, since if the principle polarisation axis of the second LCS has a larger angle than the first, the result would be a sharp increase in the average polarisation angle, which is seen. Although the system has a large range of polarisation angles (32.5 °), the polarisation angle for an LCS while it is in one of the 'splitting states' as described earlier, is relatively stable. This can be seen from the flat portions of Fig. 5.9 between 386 mA and 397 mA and was verified by examining the evolution of the polarisation angle for a single LCS. For high currents there is considerably less variation in polarisation angle and the system eventually settles to a stable polarisation angle of 40 ° when the spatially extended lasing states are dominant.

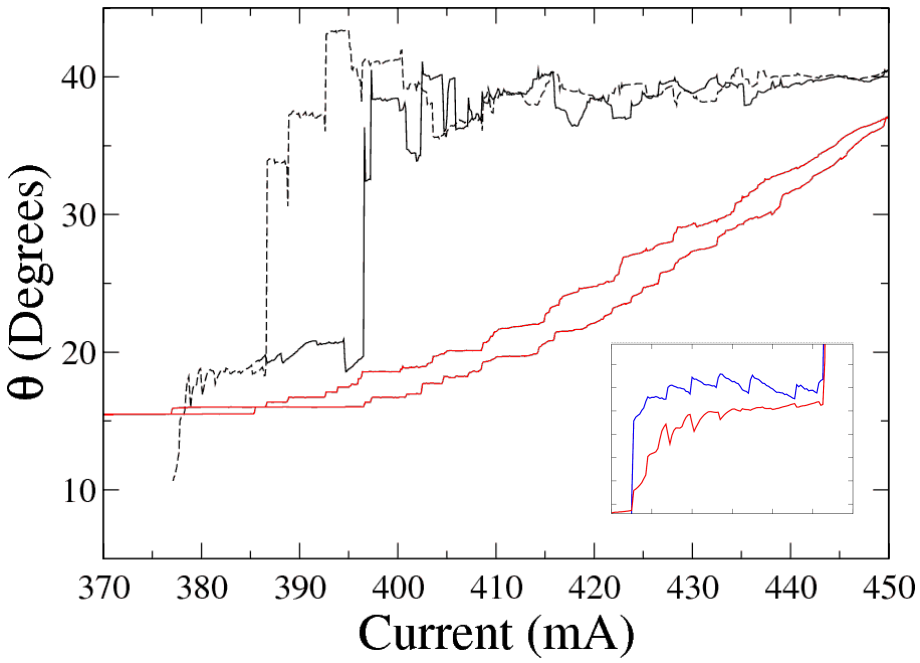

Figure 5.9: Polarisation angle averaged over the whole aperture of the VCSEL with varying current. Solid line for increasing current, dashed line for decreasing current. The kinks appearing between transitions are an artefact and result from non-simultaneous scans for the separate polarisations. The grey lines are a re-scaled LI-curve of total power in both polarisations included to illustrate where the switching points occur. The inset is a zoom between 376 mA and 388 mA, the blue line shows the evolution of the horizontal component of the total intensity shown in the main figure, and the red line shows the evolution of the vertical component. Their amplitudes have been normalised such that the vertical component has a similar amplitude to the horizontal component for clarity.

Table 5.1: Polarisation angles for each LCS just above their respective thresholds. Numbering corresponding to the standard set in Fig. 4.3.

Soliton	θ	θ with HWP
1	19°	37°
2	58°	14°
3	52°	5°
4	46°	3°
5	52°	4°
6	48°	1°
7	39°	15°

For low currents (< 385 mA) a sawtooth-like evolution of the polarisation angle is seen which is the product of a rise in one polarisation component coinciding with a fall in the other (see inset of Fig. 5.9). These 'teeth' grow in amplitude until just before switch off the polarisation angle drops drastically until the LCS can no longer be sustained and switches off.

These 'sawtooth' modulations are known to exist in systems with frequency-selective feedback [77] and are related to external cavity mode switching. When the current is decreased the frequency of the VCSEL is indirectly tuned via Joule heating, increasing the detuning between the CS and the external cavity. When this detuning becomes too large to sustain the LCS, the LCS must adapt to a new external cavity mode. If the VCSEL is birefringent each polarisation component would come in and out of resonance with the external cavity at different rates, causing an increased intensity in the resonant polarisation component while decreasing the intensity of the orthogonal component, resulting in a change of polarisation angle. When the LCS switches external cavity mode, the detuning 'resets' and gives rise to a 'sawtooth' modulation of the polarisation angle .

When the spatially averaged polarisation of the free running VCSEL is measured, a polarisation anisotropy is found with one principal axis of polarisation is found to be weakly dominant. In an attempt to simplify the polarisation characteristics, a half-wave plate is placed after the VCSEL to turn this preferred axis to be parallel to the table thus matching it to the low-loss axis of the beamsplitter. With the half-wave plate installed, the polarisation angle for each LCS is remeasured and the results are noted in the second column of Table 5.1. The

polarisation angles of the 'well behaved' LCS are turned towards the horizontal, which should correspond to the situation of lowest losses. The first LCS however produces the opposite behavior. Importantly, all polarisation angles are still different. This might indicate that the orientation of the principal polarisation axes across the aperture is not homogeneous, possibly due to inhomogeneous strain incurred in the very delicate mounting of these broad-area devices. In small-area VCSELs, uncontrolled variations in growth or contacting are known to lead to stress changing the linear polarisation anisotropies [83, 124]. In particular, it was found that the principal axes of polarisation in arrays of small-area lasers are close to each other but different [124]. This seems to be similar to the situation seen here.

5.2.2 Polarisation Control

It should be noted that by turning the half-wave plate the polarisation angle of the LCS can be dragged, seemingly choosing a compromise between the different principal axes of anisotropic elements in the system.

Polarisation control is achieved by adding a linear polariser to the external cavity. For the simplest possible case the cavity is forced to have horizontal (parallel to table) polarisation. In this case all of the polarisation elements are forcing the horizontal polarisation and all of the CS are measured to be near the horizontal polarisation as expected. If the polariser is turned then the CS polarisation angles adjust to be close to the angle of the polariser. We note however that each CS still has a unique angle and that it is not possible to reach completely vertically polarised CS, most probably due to competing intra-cavity polarising elements.

If the polariser is turned select vertical polarisation then the polarisation angles which result are shown in Fig. 5.10. The polarisation angle of the lasing pattern occurring at the highest currents seems to settle on a certain value, which is expected to be 90 °, however it eventually settles around 73 °. This may be the effect of the beamsplitter forcing it's own polarisation preference on the system however modeling using a ray transfer matrix approach (ABCD matrix, see [112]) for both a single pass system and a multiple round trip approach did not allow

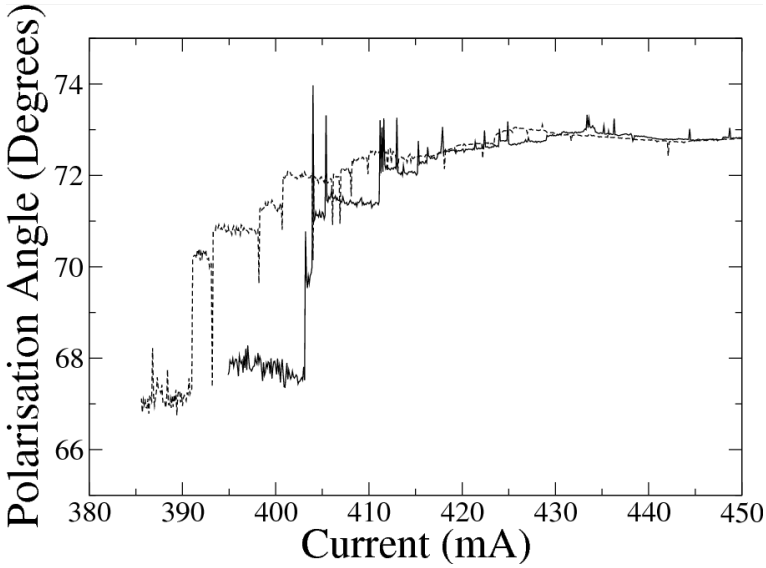

Figure 5.10: Polarisation angle averaged over the whole aperture of the VCSEL with varying current. The intra-cavity half wave-plate is set to turn the principle polarisation axis of the VCSEL to be parallel to the table and the intra-cavity polariser is set to transmit vertical polarisation. Solid line for increasing current, dashed line for decreasing current.

this. Another possibility is that there is an inherent limitation imposed by the measurement method, and indeed parasitic polarisation leakage from the polariser does not allow measurements of 90° however tests indicate that angles of 88° should be measurable.

It is therefore conjectured that there must be some inherent polarisation preference induced by either the whole VCSEL, or the LCS itself. This unintuitive behaviour turns out to be the defining feature of the system with half wave-plate and intra cavity polariser. The useful result that the polarisation may be controlled by an intra-cavity half wave-plate are noted and the further analysis of these extremely complex and unintuitive polarisation behaviours are left for further study.

Chapter 6

Temporal Dynamics

6.1 Switching Dynamics

In this section the transient behavior at switch-on of a CSL is addressed, investigating threshold powers and switching delays because of the obvious relevance for applications. The transient involves strong oscillations due to multi-mode dynamics in the external cavity. Although the involvement of unstable separatrix states in soliton dynamics is not new, the fact that a CSL has frequency freedom means that multiple separatrix states exist, generally having different frequencies from the final stable LCS state. This substantially changes the dynamics and phenomenology of switching behavior of LCS.

6.1.1 Experimental Setup

A schematic of the experimental setup used to monitor switching dynamics is shown in Fig. 6.1. The cavity length used is the 'long cavity' arrangement giving an external cavity longitudinal mode spacing of 1.65 GHz corresponding to a round trip time of 0.606 ns.

In most realisations there are two additional polarising elements in the cavity. A half-wave plate and a linear polariser are adjusted to enforce linear polarisation close to the vertical axis in order to suppress polarisation instabilities (see Sec. 5.2 and [129]) and optimise out-coupling. The latter is essential for time resolved measurements at high frequency due to the relatively low sensitivity of

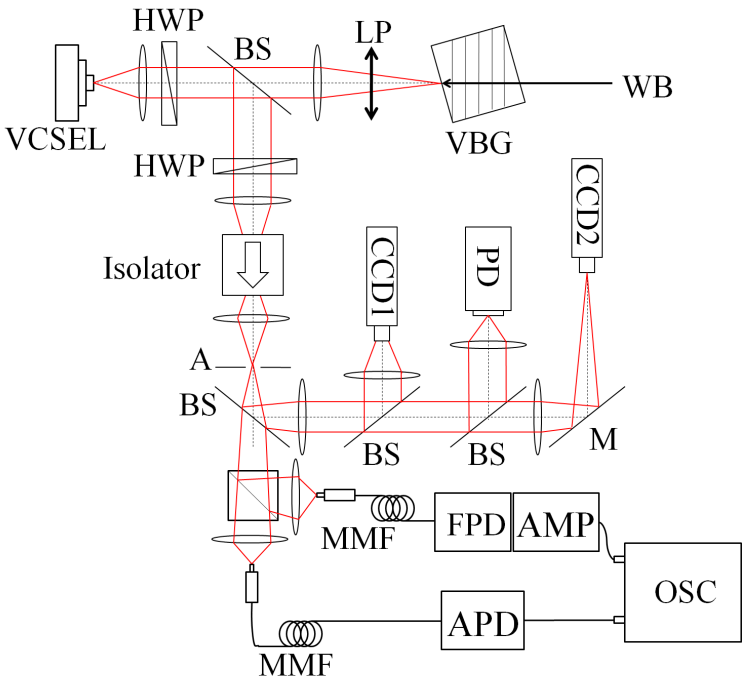

Figure 6.1: Experimental setup. VBG: Volume Bragg grating, BS: Beamsplitter, HWP: Half-wave plate, LP: Linear polariser, M: Mirror, A: Near field aperture, MMF: Multi-mode fibre, CCD1(2): CCD camera in far (near) field image plane of VCSEL, PD: Photodiode, FPD: 12 GHz fast photodetector, WB: Writing Beam, APD: Avalanche photodiode, AMP: RF Amplifier, OSC: 16 GHz Oscilloscope.

fast photodetectors and the low intrinsic power of the LCS. With the intra-cavity polariser set to transmit vertically polarised light 15 μW of optical is outcoupled per detector for a single LCS after all losses in the beam path e.g. lens losses, isolator losses and beam splitting. Two fast detectors are used for time resolved measurements and their specifications can be found in Sec. 3.4.5. The writing beam (WB) is once again required to switch the LCS and the details of it's operation can be found in Sec. 3.3.

6.1.2 Switch-on Behavior

6.1.2.1 Experimental Results

The LCS may be switched to the 'on' state with an external writing beam (WB). Here the WB is about 0.1 nm blue detuned to the feedback wavelength as this was found to produce the largest reduction in threshold (see. Sec. 4.5.2). The system is biased in the bistable range of the LCS, so that it is stably in the off state, but there is a simultaneously stable on state. A laser pulse is then fired from the WB at the location where the LCS should be ignited. In an ideal system this could be any position on the VCSEL aperture, but in practice there are preferred LCS locations, and the WB is aimed at that with lowest current threshold. Similar behavior, at least qualitatively, is obtained for other LCS, although no systematic comparison was undertaken.

The effect of different pulse parameters on the switch-on is characterised first. The peak power and hence energy required to create an LCS is sensitive to where the current is biased with respect to the spontaneous switch-on threshold. An experimental uncertainty arises from a drift of this threshold (see Fig. 4.4), probably due to thermal fluctuations. To account for these effects the VCSEL is biased 3 mA below the spontaneous switch-on threshold by slowly increasing the current until the LCS appears, then the current is reduced by 3 mA and the LCS erased by interrupting the feedback. The switch-on is then induced with the WB and afterwards the spontaneous switch-on threshold is found again. A correction for the actual difference between the bias current and threshold is then performed via the normalisation curve shown in Fig. 6.2.

Fig. 6.3 shows the minimum peak power required for switch-on vs. the pulse length. As expected, shorter pulses require higher peak pulse power, with the shortest pulse (experimentally limited to 15 ns) still able to achieve switch-on. The curve seems to follow a quasi-hyperbolic trajectory for pulses shorter than 100 ns, but flattens off for pulses longer than 100 ns, suggesting that a minimum peak pulse power is required to switch on a LCS.

It is also instructive to look at the required pulse energies which turn out to be in the hundreds of fJ range (see Fig. 6.4). Two distinct regions are apparent. In the region above 100 ns a quasi-linear increase in energy with pulse length is seen,

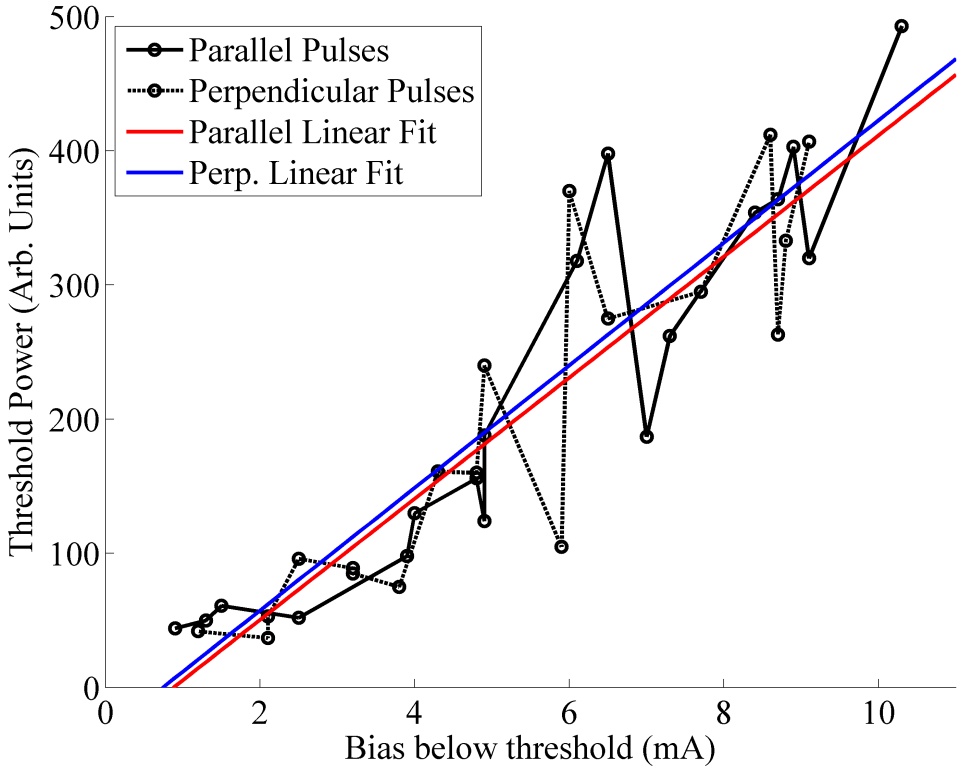

Figure 6.2: Peak pulse power required to switch an LCS on for varying bias currents relative to threshold. The horizontal axis is defined as the difference between the bias current and the spontaneous switch-on threshold. The solid black curve corresponds to pulses injected with the same linear polarisation as the LCS, the dotted for injected pulses which are polarisationally orthogonal to the LCS.

the linear fit to which intercepts at zero. A threshold pulse energy proportional to the pulse duration indicates a constant threshold power supporting the conclusion reached earlier from Fig. 6.3.

For a pulse length below 100 ns there is a slow increase in the required energy with increasing pulse length. A horizontal line would correspond to an area-law, in which only pulse energy is decisive, i.e. the peak power is inversely related to the pulse length. An area law can be derived, and indeed observed, in driven bistable systems, for cases where the excitation pulse is shorter than the characteristic relaxation time of the system [19, 74, 101, 102, 109]. Here, the addressing pulse is

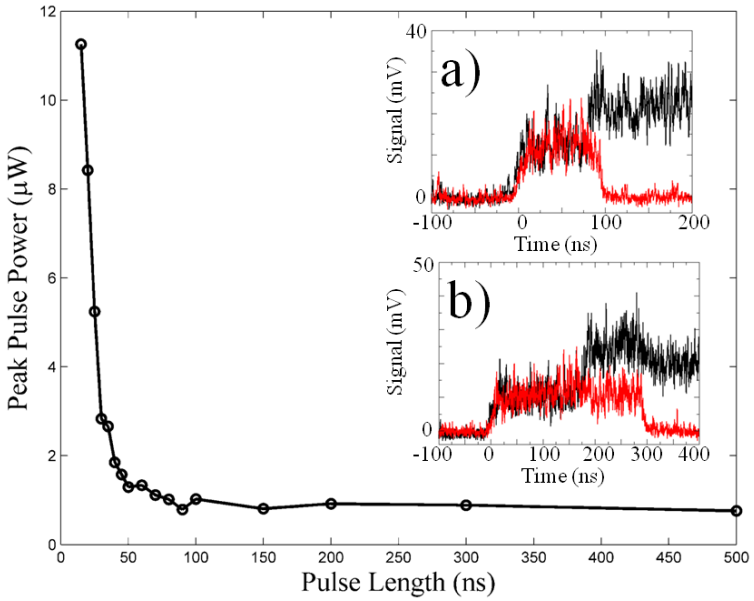

Figure 6.3: Minimum peak pulse power required to switch on an LCS for varying pulse lengths at a fixed difference between bias current and spontaneous switch-on threshold. Inset: Time trace of switch-on events for a) 100 ns pulse, b) 300 ns pulse. The red line corresponds to the WB pulse and the black line shows the response of the LCS. The LCS always switches to the same power. Data taken without the intra-cavity polariser shown in Fig. 6.1. Cavity round trip time 0.606 ns.

neither short compared to the carrier lifetime nor to the external cavity round-trip time (both being in the range of 1 ns), hence an area law is not expected. Since no theoretical investigation in the appropriate limit of very short addressing pulses are known, it is actually not clear whether an area law holds at all in the laser case (this will be commented on later in the theoretical section). Nevertheless, one might speculate that the decrease in threshold pulse energy with decreasing pulse length (without intercepting to zero threshold energy) might indicate a transition to an area-law behavior.

In most applications, one is not only interested in the threshold values but also in the details of the LCS response in the time domain. The insets in Fig. 6.3 give a first overview for close to threshold pulses. For pulses longer than 100 ns, the LCS switches on during the pulse (see in Fig. 6.3b), i.e. there is no benefit from the extra energy put in afterwards. For shorter pulse durations, the LCS

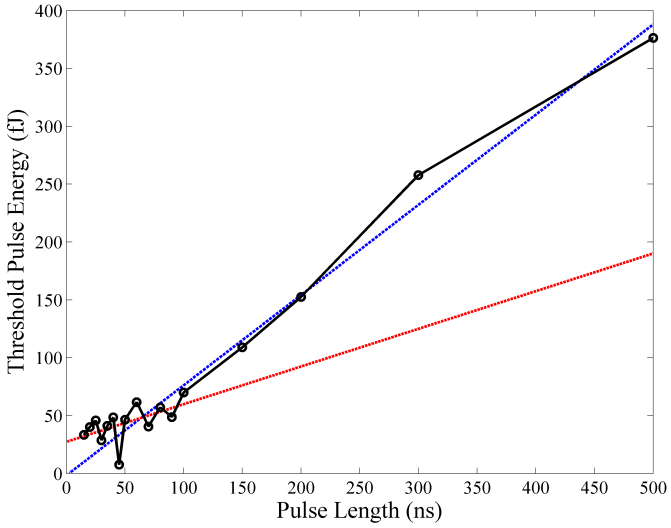

Figure 6.4: Minimum energy required to switch a LCS on for varying pulse lengths and fixed difference between bias current and spontaneous switch on threshold. The lower red linear fit is for all pulses shorter than and including 100 ns, the upper blue linear fit is for all pulses longer than and including 100 ns.

rises at the end of the pulse (100 ns, Fig. 6.3a).

For 15 ns pulses, a detailed investigation is shown in Fig. 6.5, which shows time traces of three switch-on events for different pulse amplitudes. For threshold power there is some delay between the rise of the pulse and the rise of the LCS in response. The delay becomes smaller for larger peak powers, and disappears, within experimental resolution, for peak powers only 1.6 times threshold power. Evolution to the on-state involves some transient dynamics, which will be discussed in section 6.2.

Increasing the pulse length – hence decreasing the threshold peak power – increases the threshold delay significantly. Fig. 6.6 shows the pulse and LCS responses for three increasingly powerful 50 ns pulses. At threshold the LCS is only fully switched after the pulse has finished, which can be interpreted as a consequence of the requirement to reach the separatrix for switch-on. In bistable systems, the separatrix is the unstable state between the two stable ones (see [6] for a review in the context of LCS). If that is crossed by the finite-amplitude ('hard') perturbation, the system relaxes to the on-state, otherwise it decays back

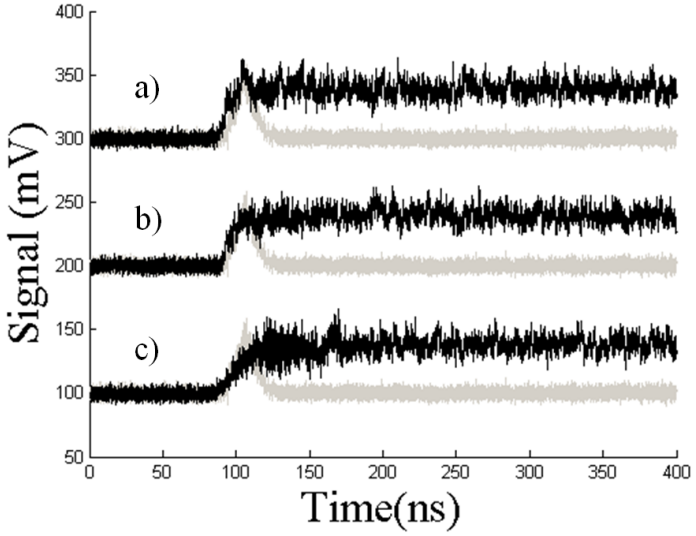

Figure 6.5: Time series of pulse (grey) and LCS response (black) for three 15 ns long pulses with power a) 3.4, b) 1.6, c) 1 (normalised to threshold power). Curves are offset by 200 mV for clarity. WB pulse traces are indicative of position and length but not amplitude. Traces taken using the 1.1 GHz bandwidth APD for increased signal to noise ratio. Cavity round trip time 1.05 ns.

to the off-state. Directly on the separatrix, the system is marginally stable and hence the decay is very slow leading to a long switch-on delay. Note that our system is not designed to permit close approach to the exact separatrix state, and very long delays are neither expected nor observed. Above threshold, the separatrix is crossed already during the perturbation and the resulting dynamics occur faster leading to a reduction of delay.

Fig. 6.7 presents a summary of the switch-on delays for different pulse lengths. It indicates that for pulses close to threshold power the delay of the on-switch is increasing with the length of the pulse. The delay then decreases as the peak pulse power is increased. For high powers, typically above seven times the threshold power, the LCS rises at the same time as the pulse (within resolution). The reduction of the delay time with increasing power is in qualitative agreement with the findings for non-critical slowing down [19, 74, 101, 102, 109] but it should be stressed that the simple analytical relationships obtained in these references cannot be applied to our case. Ref. [50] analyses the switch-on of LCS in an

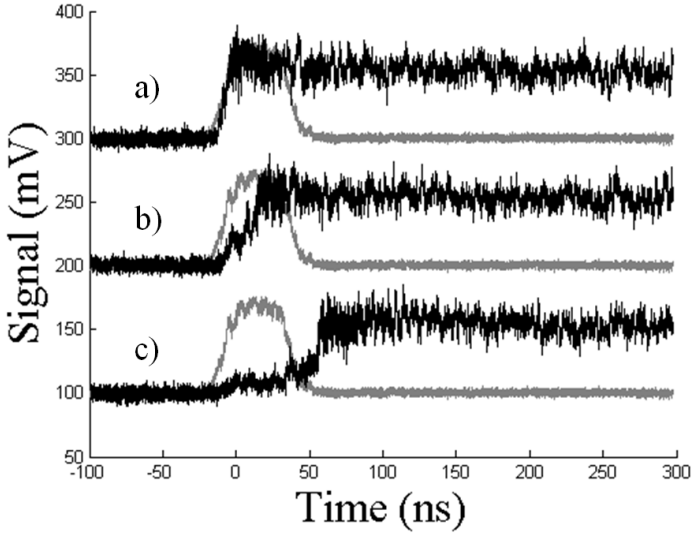

Figure 6.6: Time series of pulse (grey) and LCS response (black) for three 50 ns long pulses with power a) 11.8, b) 4.2, c) 1 (normalised to threshold power). Curves are offset by 200 mV for clarity. Pulse traces are indicative of position and length but not amplitude. Traces taken using the 1.1 GHz bandwidth APD for increased signal to noise ratio. Cavity round trip time 1.05 ns.

amplifier system and does not report simple area-law relationships either. Numerical simulations on a CSL with saturable absorption indicate the validity of an approximate area law for high pulse amplitudes, i.e. low pulse durations [68].

It should be noted that the data in Figs. 6.3, 6.4 and in Figs. 6.5, 6.6 and 6.7 were obtained in different cavity configurations (without and with intra-cavity polariser, different cavity length). With polariser, the width of the hysteresis loop was significantly reduced, which is likely to be responsible for an increased sensitivity to fluctuations, explaining some of the scatter of the data points in Fig. 6.7. It proved to be impossible to map reliably the threshold curve for pulses longer than 150 ns where the cross-over to a minimum threshold power seems to occur in that scheme.

6.1.2.2 Numerical Simulations

The soliton writing process has been investigated in detail in the model (Eqs. 3.1, details of which can be found in Sec. 3.5), mimicking the experimental procedure

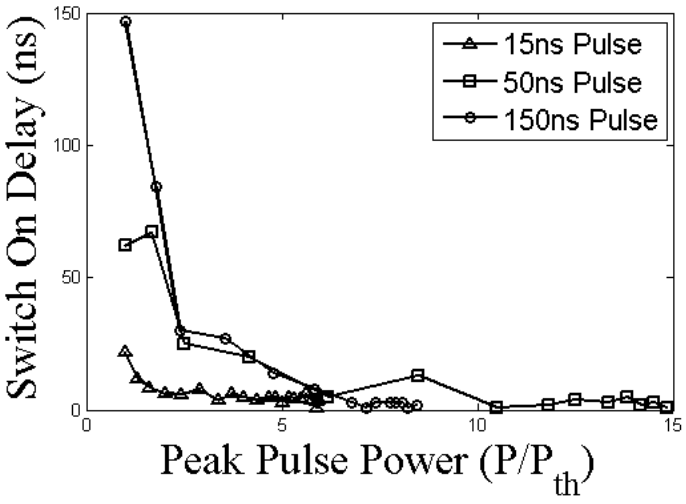

Figure 6.7: Delay between WB reaching peak power and the LCS reaching peak power for varying peak pulse powers. The curves correspond to different pulse lengths as indicated in the legend. All curves normalised to threshold peak pulse power. Delay time measured by digitally frequency filtering of the LCS response data with a low-pass filter to highlight the upper and lower levels and the transition. The delay is then taken to be the time difference between the pulse peak and the response reaching the upper level.

described in Section 6.1.2.1. The LCS is initiated through the application of a spatially–localised rectangular WB pulse $A(x,t)$ of the form

$$A(x,t) = A_0 \exp\left(-\frac{x^2}{\eta^2} - i\omega_p t\right) \mathrm{rect}\left(\frac{t}{\tau_p}\right). \tag{6.1}$$

Computationally, the WB is added to the first of Eqs. (3.1) while the amplitude A_0, width η, duration τ_p and frequency ω_p of the address pulse can all be varied. In the simulations these quantities are dimensionless. In order to make a qualitative comparison with the experiment, however, a typical cavity decay time of 10 ps is used. In [108] the width and frequency of the address pulse was fixed to map a region of successful LCS initiation in the plane of amplitude and duration. Here, instead, the effect of the frequency ω_p on the minimum amplitude A_0 necessary for the initiation of a LCS is investigated first. The value of the address pulse duration is fixed at around 50 round trips of the external cavity (i.e. around

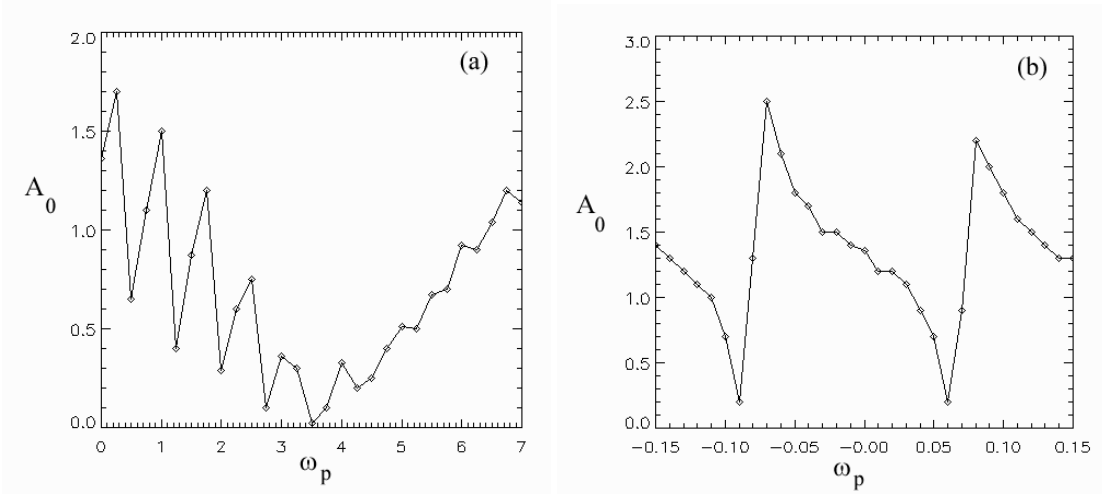

Figure 6.8: Minimum value of the address beam amplitude A_0 versus its frequency shift ω_p. Parameters are: $\alpha = 9$, $\theta = -1$, $\sigma = 0.9$, $\gamma = 0.01$, $T_1 = 0.008$, $T_2 = 0.0002$, $\beta = 0.6$, $r_g = 0.8$, $\delta = 0$, $\tau_f = 41$, $\eta = 5$, and $\tau_p = 2000$. Panel (b) is a continuation and magnification of panel (a) to show the details of the resonances with the cavity mode frequencies. Figure from [131].

20 ns). Fig. 6.8a shows that there is an optimal frequency shift of around 3.5 (corresponding to around 55 GHz or 0.18 nm in experimental values) for which the lowest-amplitude address pulses can generate a LCS. This detuning value is in qualitative agreement with the experimental finding. The envelope of the threshold characteristic presented in Fig. 6.8a is quite jagged. Although this figure is affected by under-sampling of the frequency scale, the existence of peaks and troughs is due to the external mode structure. For example, Fig. 6.8b, obtained with a higher frequency resolution, shows that when scanning ω_p there are clear resonances with the frequencies of the external cavity modes which affect the optimal operation of the switching-on process.

Next the frequency is fixed to this optimal value and the minimum value of the amplitude A_0 as a function of the duration τ_p is determined. Fig. 6.9 shows that there are two distinct regions: for pulse lengths below 15 ns, the minimum address amplitude increases as the address pulse shortens, while above 15 ns the minimum amplitude remains constant. The constant minimum address power for long address pulses translates into a direct proportionality between the pulse energy Q and its duration τ_p as shown in the inset of Fig. 6.9. When comparing the

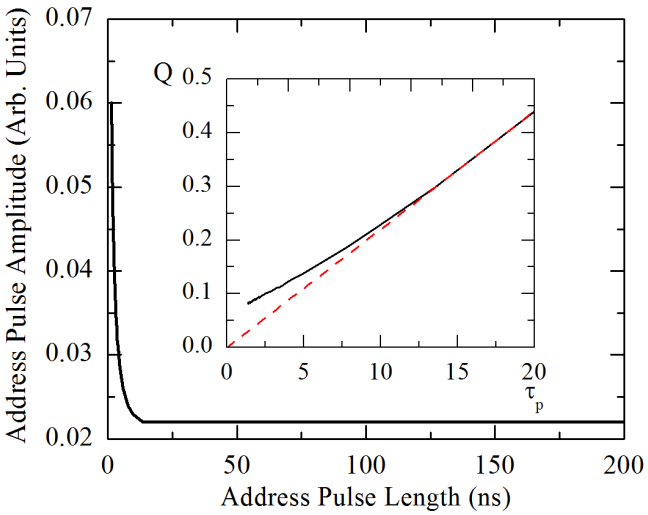

Figure 6.9: Minimum address beam amplitude A_0 for successful switching versus its duration τ_p. Parameters as in Fig. 6.8 apart from $\omega_p = 3.5$. The inset displays the threshold energy Q of the address beam versus the address pulse length τ_p. Figure from [131].

results of Fig. 6.9 with those of Figs. 6.3 and 6.4, there is an excellent qualitative agreement between the numerical simulations and the data from the experimental setup of Fig. 6.1. Since the numerical simulations were performed at the optimum frequency for high efficiency of the writing of LCS, the exact value of the pulse duration at the cross-over between the two regimes differs between the simulations and the experiments. Better agreement is, however, found for other values of the pulse frequency ω_p. For example, in the simulations of Ref. [108], the cross-over occurred at pulse durations of around 70 ns for $\omega_p = 0$.

Typical behaviors of the LCS switching in the two regions identified in Fig. 6.9 are shown in Fig. 6.10 (a) and (b), respectively. For short pulse durations τ_p of the WB, the address amplitude A_0 required to reach threshold is higher than the case of longer τ_p. Away from threshold (upper traces in Fig. 6.10 (a) and (b)), delays between the switch on of the LCS and the WB pulse are strongly reduced. There is again a good agreement with the experimental observations of Figs. 6.5, 6.6 and 6.7 where the delay reduction is most noticeable at longer WB durations.

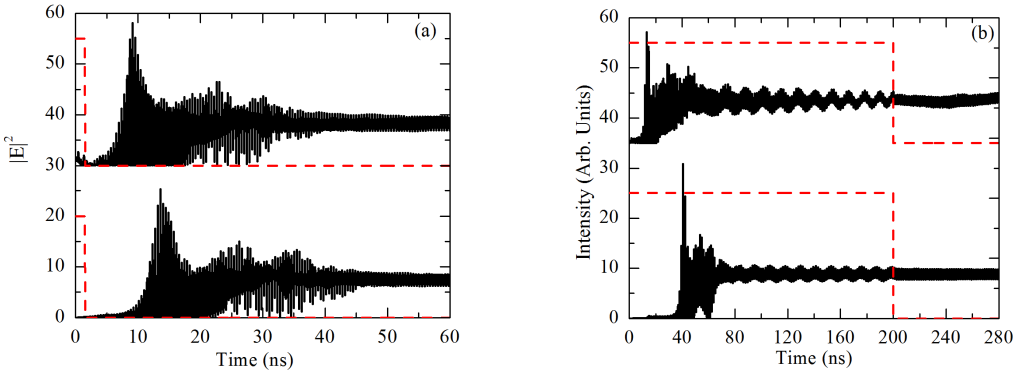

Figure 6.10: Time evolution of the peak output intensity of the LCS for (a) τ_p =1.5 ns, $A_0 = 0.06$ (lower trace) and $A_0 = 0.6$ (upper trace); (b) τ_p =200 ns, $A_0 = 0.022$ (lower trace) and $A_0 = 0.22$ (upper trace). The other parameters as in Fig. 6.8 apart from $\omega_p = 3.5$. The red dashed lines display the length of the address WB but the amplitude is scaled for clarity. Figure from [131].

6.1.3 Transient Spectral Dynamics

The successful addressing of LCS in VCSELs with frequency selective feedback appears to be accompanied by transient oscillations. This was first experimentally observed in [118] and later confirmed in numerical simulations [108]. Here experimental evidence is presented in the spectral domain, demonstrating that a considerable number of external cavity modes are involved during these transient oscillations. Typically only a single mode, perhaps with sidebands, remains in the final LCS state.

6.1.3.1 Experimental Results

Experimental investigation of the transient temporal dynamics of a LCS requires a very high temporal resolution. For this investigation the time traces are obtained via the same procedure as in Fig. 6.5-6.6 but using the 12 GHz detector. This fast detection limits the signal to noise ratio, making direct time trace analysis difficult. For a clearer analysis, a time-frequency spectrogram is used. This is simply a time evolving Fourier transform of the time series with overlapping time windows and is outlined in Sec. 3.4.6.

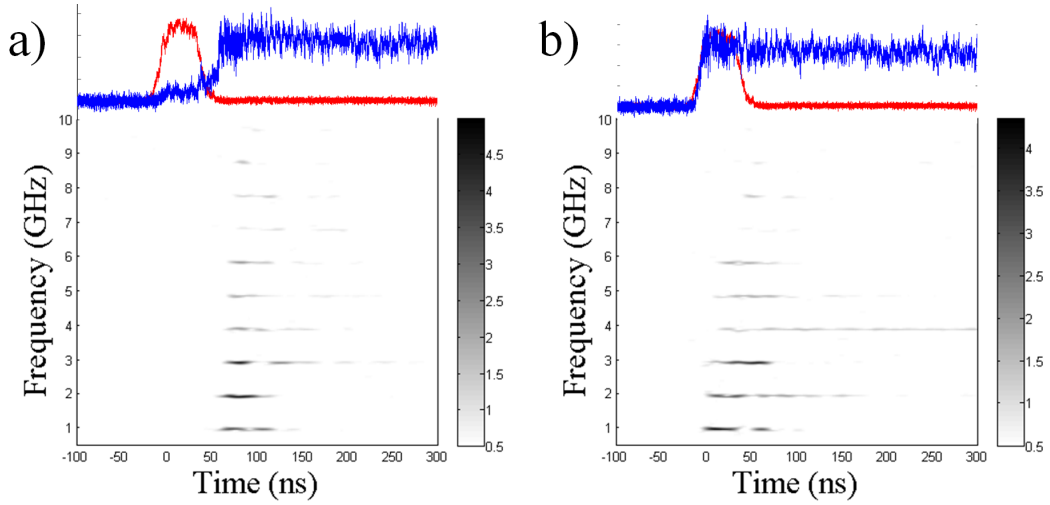

Figure 6.11: Time-frequency spectrograms showing the time evolution of intensity modulation frequency for a switch-on event initiated by a 50 ns and pulse of a) minimum threshold power and b) 11.8 times threshold power. The corresponding time-series to which the spectrogram corresponds is shown above the plots, with the red trace corresponding to the pulse and the blue trace corresponding to the response of the LCS. Negative times correspond to the off state, before the pulse is applied. The pulse reaches peak intensity at time 0. Fourier window of 25.6 ns without peak size renormalisation.

The first time-frequency analysis presented is for a 50 ns pulse with threshold peak power, shown in Fig. 6.11a. Low frequencies are not shown since at switch-on the DC contribution dominates and would swamp the oscillation peaks. The main oscillation frequencies are the external cavity round trip frequency (950 MHz) and its harmonics. The delay associated with low peak power is present, followed by the excitation of many frequencies. The strongest frequencies are the second and third harmonic at 1.9 GHz and 2.85 GHz but all harmonics up to 10 GHz are excited and sustained for approx 50 ns. After this initial burst of oscillatory action the system begins to fluctuate between frequencies. Its behaviour then simplifies, until the system has relaxed to a non-oscillatory steady on-state.

Fig. 6.11b shows the transient dynamics for a 50 ns pulse far above threshold peak pulse power. It shows similar behavior to that of a threshold pulse, but there is now a strong oscillation from the beginning of the WB pulse. When the pulse ends the dominant harmonic shifts, and the intensities of the peaks

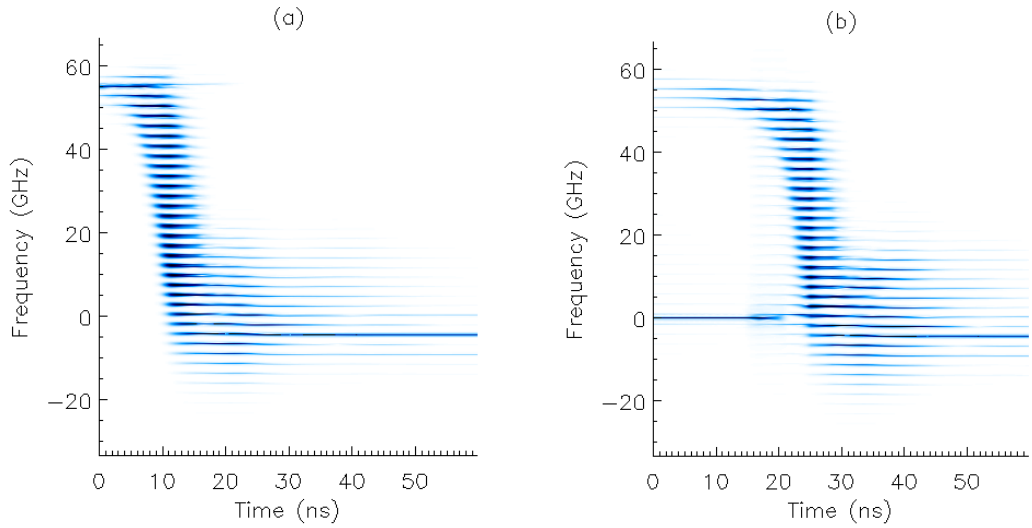

Figure 6.12: Time evolution of the frequency spectrum evaluated every round trip. Parameters are the same as in Fig. 6.8 but with $\tau_p = 20$ ns and $\omega_p = 55$ GHz (a) and $\omega_p = 0$ GHz (b). Each frequency spectrum is normalized such that the highest intensity corresponds to dark blue (black), to avoid the dominance of the final peak. Figure from [131].

reduce. The evolution again shows the reduction of oscillating harmonics until the system simplifies into one or two frequencies. The system does not relax to a non-oscillating state in this case, however, as the component at 3.8 GHz remains. These states may show long-term stable oscillations, whose properties are discussed in detail in Sec. 6.2. Alternatively, a macroscopic fluctuation can cause the oscillating state to decay to a non-oscillatory LCS state (vice versa, a steady state can 'spontaneously' convert to an oscillating state).

6.1.3.2 Numerical Simulations

The numerical integration of the model (3.1) provides temporal data on the dynamics of the LCS switching. From this data the frequency spectra have been evaluated and are displayed in Fig. 6.12. The spectra of $E(x = 0, t)$ are then computed for each round-trip and the evolution of such spectra over a slower time scale are plotted.

Fig. 6.12a shows the transient spectral dynamics when the writing beam has

a duration of 20 ns and is blue-shifted from the grating frequency by around 55 GHz (corresponding to the minimum writing beam amplitude as determined in Section 6.1.2.2). Already before the end of the address pulse, multi-mode operation sets in. At 10 ns from the beginning of the simulation, around 30 external cavity modes are present. This regime of frequency spreading is followed by a fast (around 5 ns) sweeping of the frequency spectrum, accompanied by a narrowing to only about 15 modes. Then slower spectral evolution leads to a further narrowing of the spectrum and to the final state of the LCS, which has one strong mode and a few weak side-modes.

Surprisingly, very similar spectral dynamics take place when the writing beam frequency is close to that of the final LCS (Fig. 6.12 (b)). In this case, the writing beam corresponds to $\omega_p = 0$ and yet one still observes the same three distinct dynamical regimes: creation of a band of modes close to 55 GHz, followed by a fast spectral broadening and frequency sweep, and finally a slower spectral narrowing to a quasi-single-mode LCS emission state. Apart from a longer duration of the first phase, this spectral evolution is remarkably similar to that observed in Fig. 6.12 (a). This suggests the existence of a globally attractive, yet unstable, oscillatory state that is initially approached, independently of the frequency of the writing beam. Note that this state still corresponds to spatial localisation, since the LCS is well defined during the entire duration of the transient. Another interesting feature of Fig. 6.12 is that the first frequency response of the system takes place around the blue-detuned position of the minimum determined in Fig. 6.8 (a) independently of the frequency shift ω_p of the addressing beam. This seems to correspond to the unstable low-amplitude LCS state typically found in CSL models [84, 85, 108], which is likely to behave like a separatrix in LCS switch-on.

It is important to note that the spectral features presented in Fig. 6.12 are intrinsically related to the use of an external cavity for the frequency selective feedback. The frequency sweeping, in particular, has no counterpart in VCSELs with optical injection such as, for example, [51, 70]. More generally, a CSL without holding beam has the freedom to change frequency. Similar phenomena might exist in the schemes relying on saturable absorption [41, 42] due to phase-amplitude coupling.

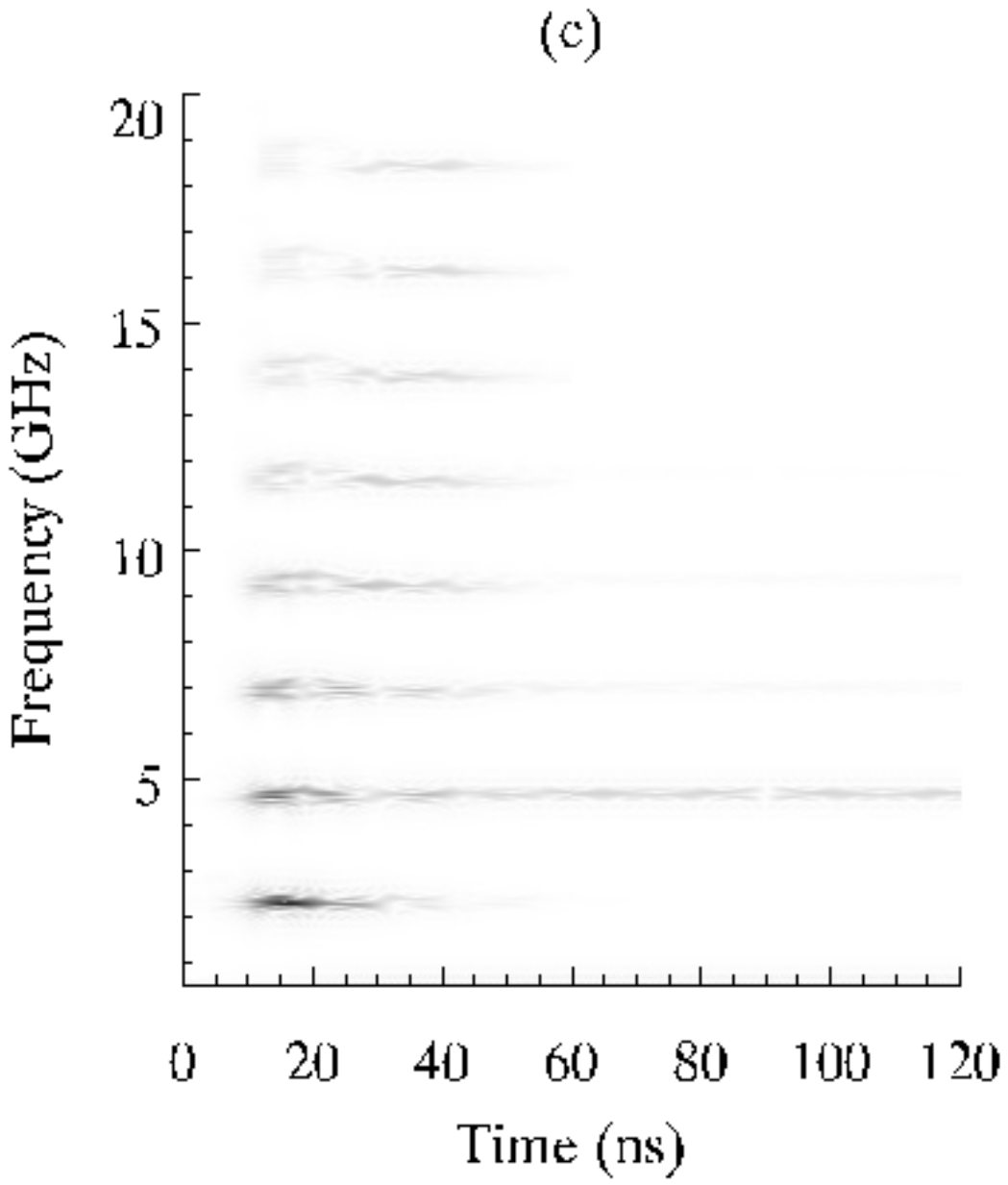

Figure 6.13: Numerical simulation of a switch-on transient of a CS initiated by a 20 ns pulse of 2.3 times minimum threshold power. Time-frequency spectrogram of intensity time series (Fourier window of 8 ns). Figure from [131].

While the ability to access directly the optical spectrum for an LCS in the numerical simulations is very useful to probe their behaviour, it is not possible to compare such measurements to the experiment. With this in mind, the RF spectrum for the optical spectrum presented in Fig. 6.12a is computed. This is shown in Fig. 6.13 and shows strong excitation of the fundamental round-trip frequency and harmonics (cut at 20 GHz to mimic the experimental cut-off at about 10 harmonics). The dynamics then simplify with the components around 5 GHz becoming dominant. If this is compared to the experimental data shown in Fig. 6.11b then it can be seen that there is excellent qualitative agreement between theory and experiment. Both show the excitation of many modes shortly after the application of the pulse, and the numbers of modes compare well. They both also show the simplification of the dynamics, i.e., a reduction in mode numbers with time.

6.1.4 Conclusion

We have shown that in this experimental realisation of a cavity soliton laser based on a VCSEL with FSF, there is a constant threshold power for switch-on pulses from a WB for sufficiently long pulses length (longer than about 100 ns). This implies proportionality between threshold energy and pulse length. For shorter pulse durations (15-100 ns), the required pulse energy does not follow this trend, but levels off towards a finite value. This might be an indication of a transition towards an area (energy) law, which might be expected in the limit of WB pulses which are short compared to all characteristic time and relaxation constants of the system, but modified by losses occurring during the pulse in the transition region.

Numerical simulations based on a model which accounts for all external cavity round trips confirm these behaviors. The pulse length at which this transition occurs differs between experiment and simulations and this is believed to be due to non-optimal WB parameters in the experiment. Switch-on is found to be possible for considerably shorter pulses than in the experiment and further systematic simulations are necessary to establish the minimum possible pulses duration and delay times important for applications. The preliminary established

limit is about 1 ns, which is of the order of, but still not short, compared to the carrier relaxation time and hence the question of the possible existence of an area law in the short pulses limit is open.

Numerical simulations show that during the switch-on of a CS, there is always a frequency excursion through a sequence of discrete modes which is attributed to the existence of multiple unstable solitons. It has been shown that minimum threshold power occurs when the WB is injected at a particular unstable soliton frequency. More surprisingly it has been shown that this excursion still occurs even if injection is at the frequency of the stable soliton. This frequency excursion to the unstable soliton with minimum threshold is followed by a cascade of frequency via the external cavity modes towards the stable soliton frequency. Many external cavity modes are excited around the steady soliton frequency for a short time then these modes decay until only a single mode, or one mode with side-modes are left. The experiment also shows the same qualitative behavior, with the main deviation being that the oscillations do not start within the pulse for threshold powers. This is believed to be due to non-optimal WB parameters in the experiment. One other aspect, which might play a role in the transient after switch-on with the WB as well as for spontaneous switching is that temperature is actually a dynamical variable [16, 106, 114] and the local radiative cooling due to the CS might influence the detuning conditions and hence mode selection.

In some realisations, a transition to an asymptotically stable oscillating state is observed. This is a very exciting observation because it indicates the possibility of achieving simultaneous spatial and temporal self-localisation via mode-locking of spatial solitons at different external cavity modes. This feature is investigated in the next section.

6.2 Steady State Dynamics

Self-confinement of light and the control of light by light are both major thrusts of modern photonics, with the ultimate goal of producing all-optical processing and high speed photonic networks [28, 110]. Similarly, mode-locked lasers are an important tool in achieving high-bit rates in optical-time-division multiplexing (OTDM). If the concepts of spatial solitons and mode-locking are combined to

create optically controllable trains of pulses which are self-confined in all three dimensions this can have several applications for all-optical networking, such as multiplexing, de-multiplexing, routing and regeneration in all-optical parallel networks.

As discussed previously, the LCS in the current CSL system have freedom of frequency and phase. Multi-frequency operation is also possible through operation on multiple external cavity modes. If the LCS would operate in multi-frequency operation and lock in phase then this should result in self-pulsing solitons which when combined with the intrinsic bistability of dissipative solitons could be used as optically-controllable pulse trains in communication systems.

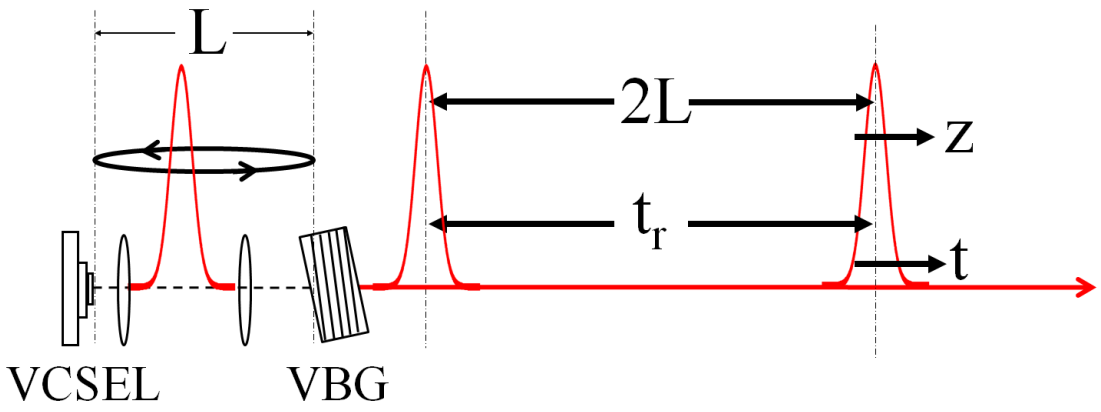

Figure 6.14: Scheme of a cavity soliton laser supporting cavity light bullets. Within the cavity, a pulse significantly shorter than the cavity round trip time and the cavity length is circulating. At the output coupler, it produces a train of pulses separated by the cavity round-trip time in time and by two times the cavity length in space.

The basic idea is illustrated in Fig. 6.14. The scheme depicted shows a laser source with a self-imaging external cavity closed by a volume Bragg grating (VBG). The cavity should be long enough to allow for multi-longitudinally mode operation and is only marginally stable for Gaussian transverse modes. If a spatial (transverse) soliton operates on multiple, phase-locked cavity modes, a pulse is formed which has a duration shorter than the cavity round-trip time and is hence also spatially localised along the longitudinal (cavity) axis. This would constitute a ball or bullet of light traveling back and forth within the cavity, a

spatio-temporal or three-dimensional cavity soliton or *cavity light bullet (CLB).* Outside the cavity, it manifests itself as a train of short pulses with the repetition frequency of the cavity round-trip time that is usual for mode-locked lasers. Indeed, the pulses in many mode-locked lasers can be understood as dissipative temporal cavity solitons, at least in many operating regimes [7].

6.2.1 Setup and Initial Investigation

The experimental setup used to investigate the existence of fast temporal dynamics is shown in Fig. 6.15, which is essentially the same as all previous realisations with the addition of a fast detector and amplifier and a Fabry-Perot interferometer (all outlined in Sec. 3.4.3 and Sec. 3.4.5).

From the outset of the setup of the CSL one of the main goals was to achieve pulsed operation of LCS. Saturable absorption is the common approach to achieve passive mode-locking of lasers, however this would require additional intra-cavity elements. Recent work in diode lasers with carefully chosen external cavity lengths lead to strong, and fairly regular temporal dynamics [117] and thus seems to be a promising approach to achieve pulsed operation. In these experiments it is found that if the external cavity round trip frequency was brought close to the twice the relaxation oscillation frequency of the laser, then there is a range of cavity lengths in which the system displays regular temporal dynamics. However this poses a problem for a CSL since it is difficult to know how to interpret the relaxation oscillation frequency for LCS. The standard rule of thumb to calculate the relaxation oscillation frequency says that it goes as $\sqrt{I - I_{\mathrm{th}}}$, however this is not determined everywhere in a CSL since the system is globally below lasing threshold, and the relaxation oscillation frequency is not defined below threshold. Furthermore, this is not defined at the abrupt jump in intensity corresponding to the switch-on of an LCS. The LCS themselves are above threshold however and should have a defined relaxation oscillation. Typical semiconductor devices have relaxation oscillation frequencies on the GHz scale and this should be a reasonably accurate starting point for the estimation of relaxation oscillation frequency. Therefore from this reasoning the external cavity should have a frequency of the order of 1–5 GHz, i.e. 1 ns–200 ps corresponding to cavity lengths

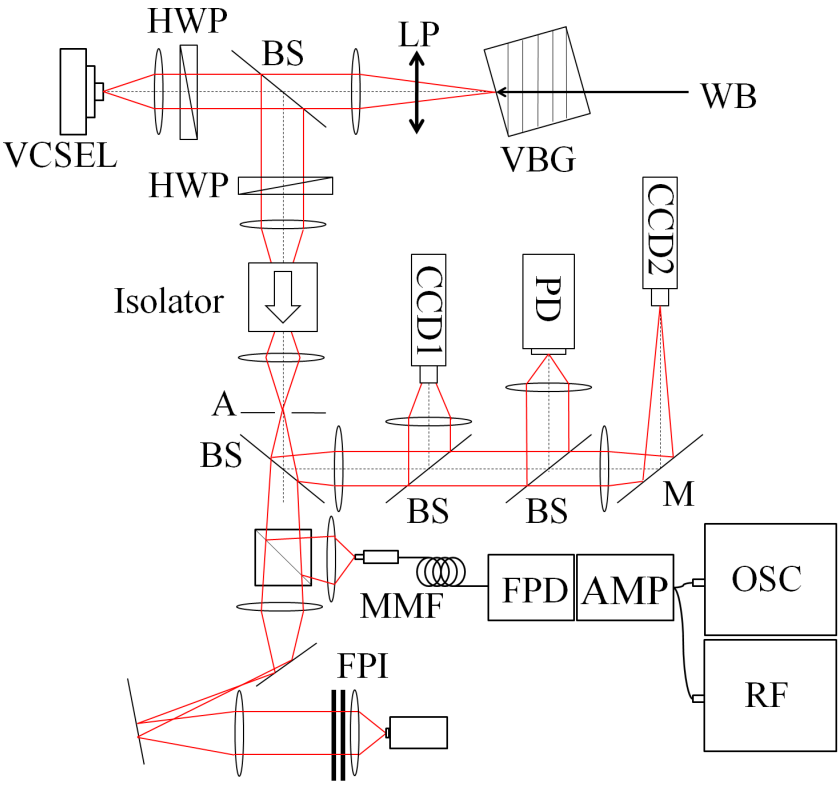

Figure 6.15: Experimental setup. VBG: Volume Bragg grating, BS: Beamsplitter, HWP: Half-wave plate, LP: Linear polariser, M: Mirror, A: Near field aperture, MMF: Multi-mode fibre, CCD1: CCD camera in far field image plane of VCSEL, CCD2: CCD camera in near field image plane of VCSEL, PD: Photodiode, AOM: Acousto-optic modulator, AMP: RF Amplifier, RF: Electrical spectrum analyser, FPI: Fabry-Perot Interferometer.

150 mm–30 mm.

Another consideration follows from a consideration of the energy storage time of the VCSEL [126]. One can imagine that if the VCSEL is operating with pulsed output then after each pulse there will be some recovery time. If the next pulse would then arrive directly as the gain recovers, the laser loses no inversion in this configuration. If the pulse would arrive too early then the gain is not present to support pulses, too late and energy is wasted which should then lead to the favouring of cw operation. It is therefore conjectured that if the external cavity length is chosen correctly, then any spontaneous pulse-like emission arising from

noise should cause the laser to switch into pulsed operation. The energy storage time in a VCSEL is essentially the carrier lifetime which is of the order 1 ns which, following this argument, would suggest that external cavity frequencies higher than 1 GHz (1 ns, 150 mm long cavity) will encourage oscillatory or pulsed temporal dynamics.

The last consideration is one which arises from the inherent difficulty of detecting fast dynamics directly and relates to the bandwidth limitation imposed by the detectors. During the stage in which the length of the external cavity was considered, the fastest oscilloscope available had a bandwidth limit of 2 GHz. Hence in order to directly investigate the temporal dynamics, the cavity should be kept below round trip frequencies of 2 GHz.

With all three considerations taken into account, a cavity length of 116 mm (1.3 GHz round-trip frequency, 0.77 ns round-trip time) was selected and is referred to as the 'long cavity' (outlined in Sec. 3.2.2). This is the cavity configuration which has been used throughout this thesis unless otherwise explicitly stated.

The first investigations attempted to look directly at the temporal dynamics using an oscilloscope. This however did not show any signs of regular temporal dynamics. To circumvent the 2 GHz bandwidth limit of the scope an RF-spectrum analyser (27 GHz bandwidth) is employed. Direct detection of the time series would not be possible though it would give insight to the frequencies involved, if any.

All LCS were investigated and the tendency was to produce no notable peaks in the RF spectrum. However, upon scanning the current in the range of the single-peaked LCS, intermittent peaks were detected. A full investigation revealed that there were specific current values in which the RF peaks were stable and sustained for seconds or minutes.

Three examples of the RF spectra which can be seen are shown in Fig. 6.16. Fig. 6.16a shows that there are many wide peaks excited, and each peak is situated on a harmonic of the cavity round trip frequency (1.3 GHz). This preference for operation on the harmonic frequencies is typical, however in general fewer frequencies are excited at one time, as in Fig. 6.16b. Here only one frequency is excited at 3.9 GHz corresponding to three times the cavity round trip frequency.

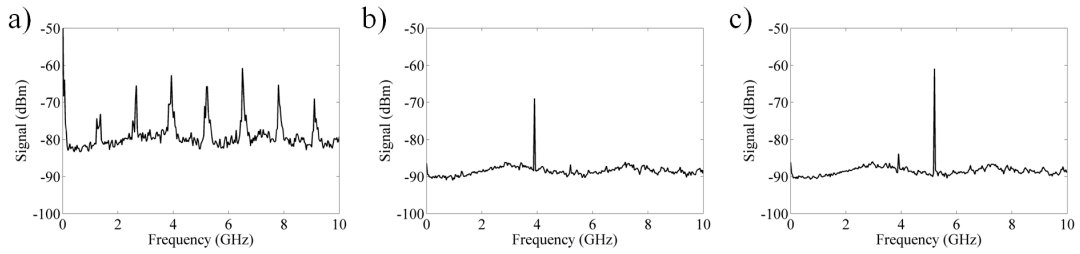

Figure 6.16: Three RF spectra taken for the same LCS in the long cavity regime with no intra-cavity polarising elements for different drive currents.

A strong peak can also be found at 5.2 GHz as seen in Fig. 6.16c. The only difference between all three of these examples is the drive current. As stated before, these LCS typically do not display peaks in the RF spectrum, i.e. they are lasing cw, however by tuning current many different peaks in the RF spectrum can be excited, of which the three shown in Fig. 6.16 are only a sample of the plethora of available behaviour.

Though the behaviour of the LCS in the RF domain is extremely varied, certain tendencies can be established. There is a preference for the LCS to favour oscillating on the third and fourth harmonics of the cavity round trip time, disfavouring the fundamental frequency. This is perhaps the manifestation of the relaxation oscillation frequency imposing it's will upon the oscillation frequency. This is supported by studying the envelopes of the spectra when many peaks are present, as this envelope in tendency has its peak around the 4–5 GHz range.

To obtain time-traces for these LCS, in addition to a fast oscilloscope, more optical power was required to obtain a signal from the photodetector. To this end a linear polariser was inserted into the external cavity before the VBG. This was oriented such that it transmits only linear polarisation perpendicular to the table. The CSL is still able to support LCS in this configuration due to the freedom of polarisation that this system enjoys. The purpose of forcing this vertical polarisation is to obtain more outcoupled power which is possible since the reflection of an uncoated glass plate (such as the outcoupling beam splitter which is used here) is polarisation dependent, reflecting roughly 1 % of horizontally polarised light and roughly 10 % of vertically polarised light when placed at 45° to the incoming beam. In this way the outcoupled power can be increased by a

factor 10. A side-effect of the intra-cavity polariser is the increase in optical path-length of the external cavity, shifting the external cavity frequency to 950 MHz.

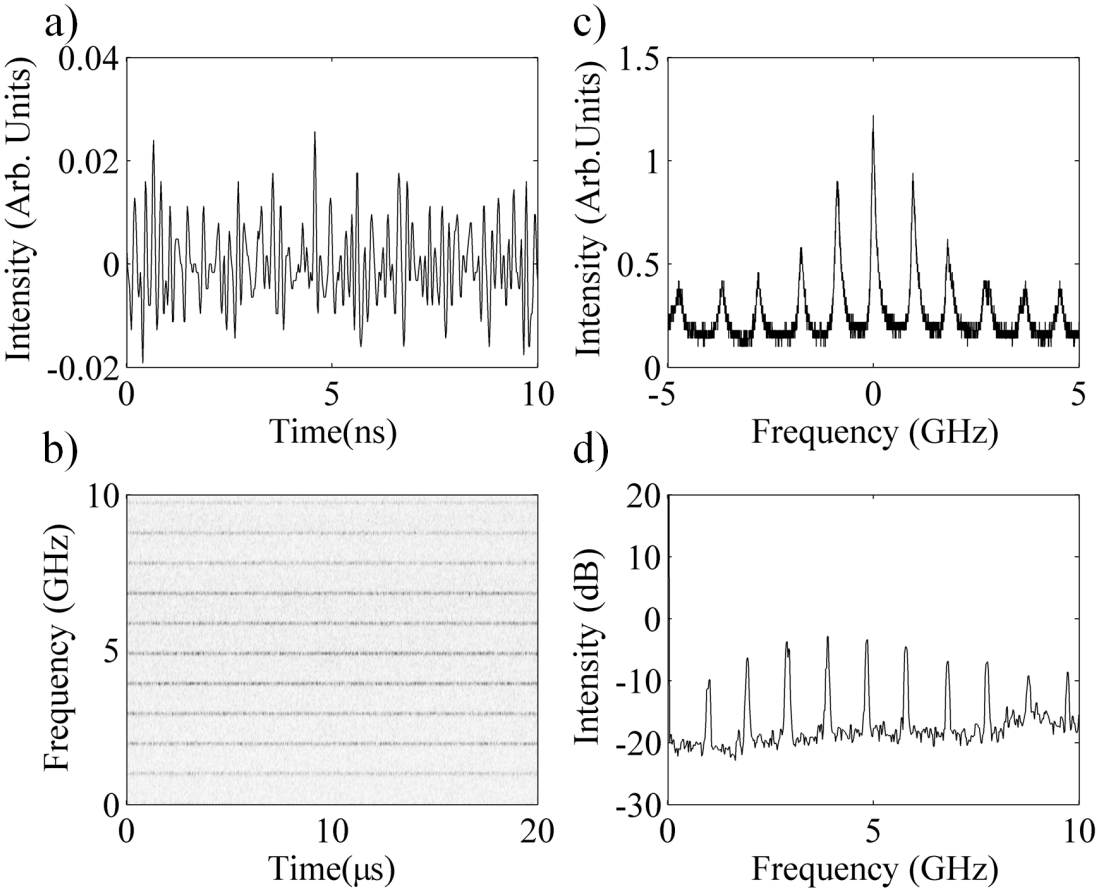

Figure 6.17: a) Zoom view of temporal dynamics. b) Time-averaged optical spectra taken on a 10 GHz free spectral range Fabry-Perot interferometer. c) Time-frequency spectrogram of the intensity oscillation frequency. d) Time-averaged RF spectrum.

This cavity configuration with intra-cavity polariser was found to display strong peaks in the RF spectra. The time-series, optical spectra, RF spectra and a time-frequency analysis (method outlined in Sec. 3.4.6) for an oscillating state in this cavity are shown in Fig. 6.17. The time-trace in Fig. 6.17a shows some irregular oscillatory peaks which are the result of many optical modes being excited (Fig. 6.17c) and accompanied by many RF peaks, at each harmonic of the external cavity round trip frequency. The RF-spectrum in Fig. 6.17 shows

that these dynamics are stable over at least some 20 μs and are in fact stable for seconds to minutes, limited only by the thermal stability of the system.

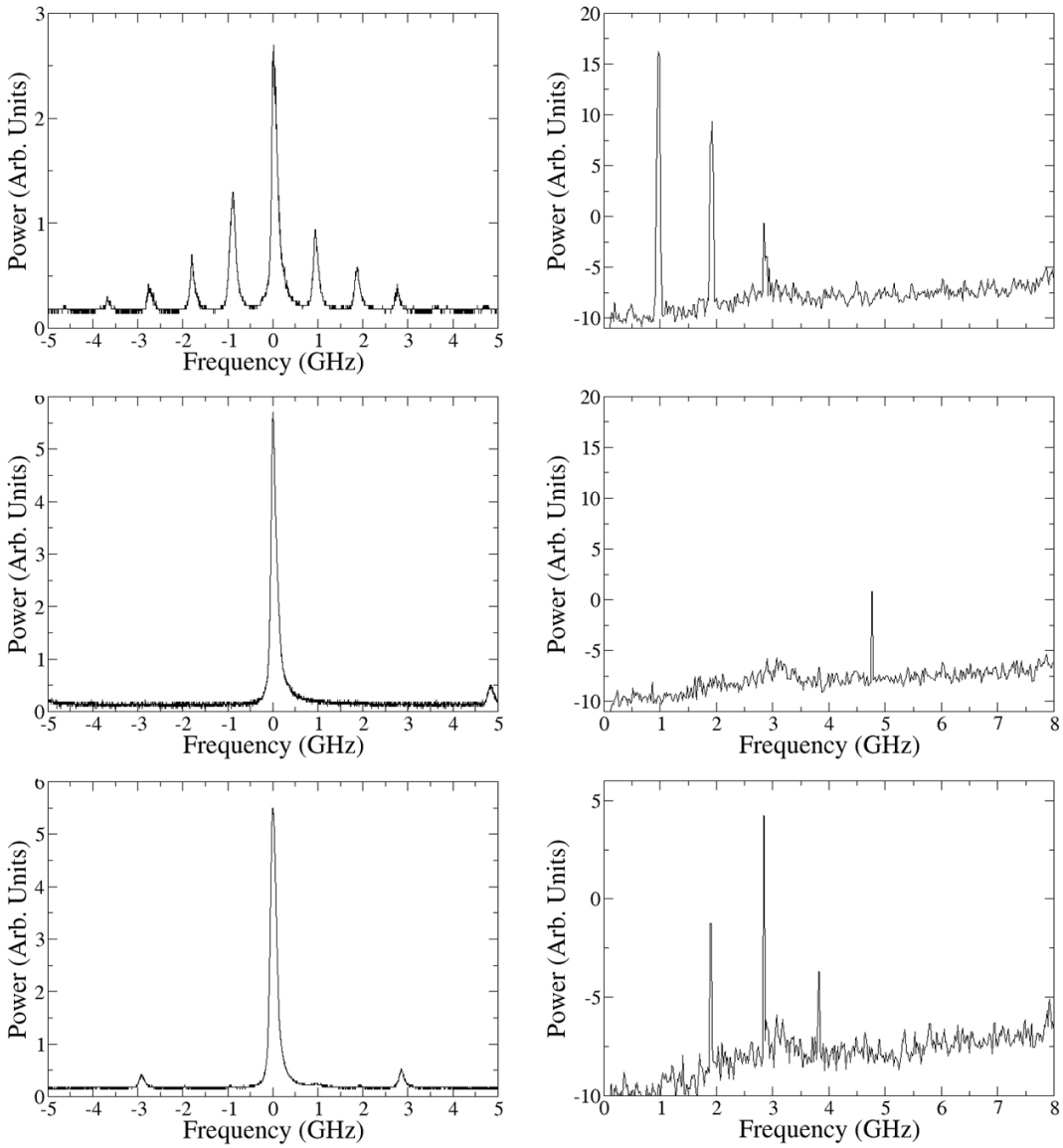

Figure 6.18: Comparison between optical modes (left column) and RF spectra (right column) for three different LCS and currents.

While the temporal dynamics are irregular, peaks are still present. This is accompanied by many optical modes and it seems interesting to investigate whether

there is a direct correlation between the excitation of optical modes and temporal oscillations. Any oscillatory behaviour would produce peaks in the RF-spectrum and hence rather than directly comparing the time-series with the optical spectrum, the RF-spectrum shall be used. The first result is that there are never any temporal dynamics if the LCS is operating on a single external cavity mode. Figure 6.18 shows the correlation between multiple optical modes and the corresponding RF-spectra. These few examples provide an almost 1:1 correspondence between optical modes and RF modes and provides the mechanism for the temporal dynamics; mode-beating. This is promising since if this phenomena can be promoted, this could lead to full mode-locking, providing the pulsed operation which is desired.

The tendency for the LCS to favour oscillating on harmonics of the fundamental cavity round trip frequency on the order 3–4 GHz suggests that shorter cavities may be more favourable for achieving pulse-like temporal dynamics. To this end, the 'long cavity' arrangement was replaced by the 'short cavity' (full details in Sec. 3.2.2) with intra-cavity polariser. This shifts the external cavity round trip frequency to 1.65 GHz.

6.2.2 Temporally Resolved Measurements

Once again, there was a rich variety of dynamics which could be produced by altering the current. The prevalence of the third and fourth harmonics were once again witnessed. Fig. 6.19 shows one of the more regular set of temporal dynamics albeit with a modulated envelope. Smaller timescales such as that shown in Fig. 6.19b reveal quite regular pulse-like dynamics. The separation of the peaks is 0.54 ns corresponding to a frequency at the fundamental of the external cavity round trip time. The width of the peaks however is much narrower, typically of the order 100 ps. To confirm that these dynamics are not a transient but persist through the entire length of the trace a time-frequency analysis was performed and is shown in Fig. 6.19c. From this it is clear that the second harmonic of the cavity round trip frequency at 3.7 GHz is the dominant frequency. Additional frequencies are also excited at the fundamental and higher harmonics. The time-frequency analysis reveals that the modulation of the envelope is due to the

modulation of the third and fifth harmonics and possibly higher harmonics which are not detected in this scheme. Over this timescale the oscillation is stable. Furthermore, the oscillation confirmed to be stable even beyond the 500 ns shown, and remains for timescales on the order seconds to minutes, limited by the thermal stability of the experiment.

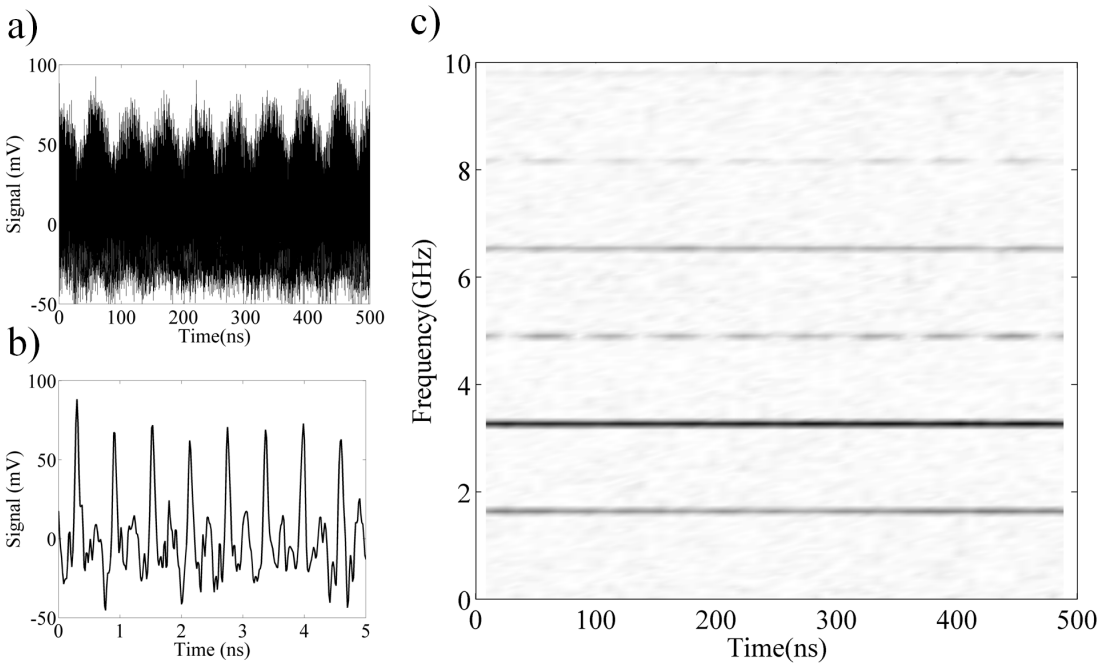

Figure 6.19: Time series obtained in a self-pulsing regime for a cavity round-trip frequency of 1.85 GHz. a) envelope, b) zoom on pulses, c) time-frequency spectrogram of intensity dynamics with 17.1 ns FFT window.

For a different current the dynamics shown previously change, and the low-frequency envelope disappears, shown in Fig. 6.20a. Short timescales still show the regular-pulse like dynamics and the corresponding frequencies are once again similar, with the second harmonic dominating. The time-series shows quite regular, pronounced pulse-like intensity spikes. The separation of the pulses has decreased to 0.27 ns corresponding to the second harmonic of the external cavity round trip frequency and the width of the pulses is once again of the order 100 ps. The AC-coupled nature of the detection does not allow a direct measurement of the modulation depth of these pulses, since all DC information is lost. An estimate can be made however by switching the LCS on and noting the jump in

DC level before it is rejected by the detector. These measurements, while not conclusive suggest that large modulation depths of >80% are possible. As before, this pulse-like behaviour is stable over seconds to minutes and therefore should not be considered to be a transient oscillation.

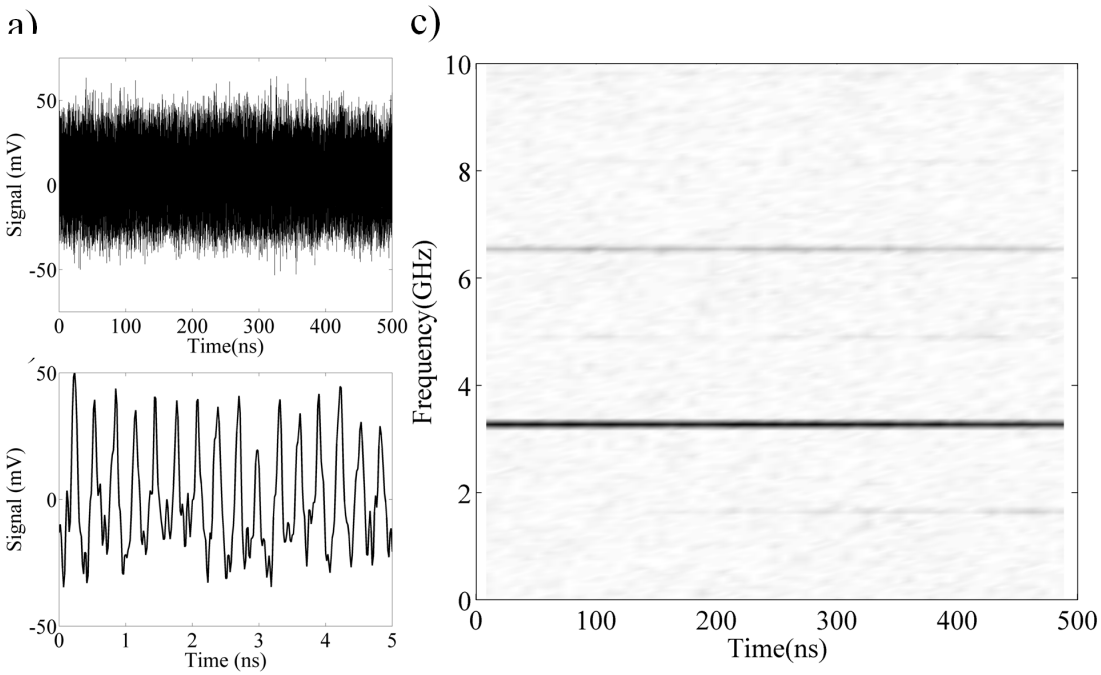

Figure 6.20: Time series obtained in a self-pulsing regime for a cavity round-trip frequency of 1.85 GHz. a) envelope, b) zoom on pulses, c) time-frequency spectrogram of intensity dynamics with 17.1 ns FFT window.

The two previous examples are not typical and in general the dynamics are rather messy with weak RF peaks and no clear pulse-like oscillations. One such example is shown in Fig. 6.21. The envelope is rather noisy with no clear pattern. Closer inspection of the peaks reveals that there is some 'pulse-like' behaviour however there are also intra-pulse peaks with a seemingly random distribution. The time-frequency analysis reveals that the frequency peaks are not well defined as before but have obtained side-peaks. The strength of the peaks also fluctuate greatly, revealing the non-stable nature of the dynamics.

It has been shown that this system is capable of producing strong, quite regular pulse-like dynamics which is attributed to mode-beating between several

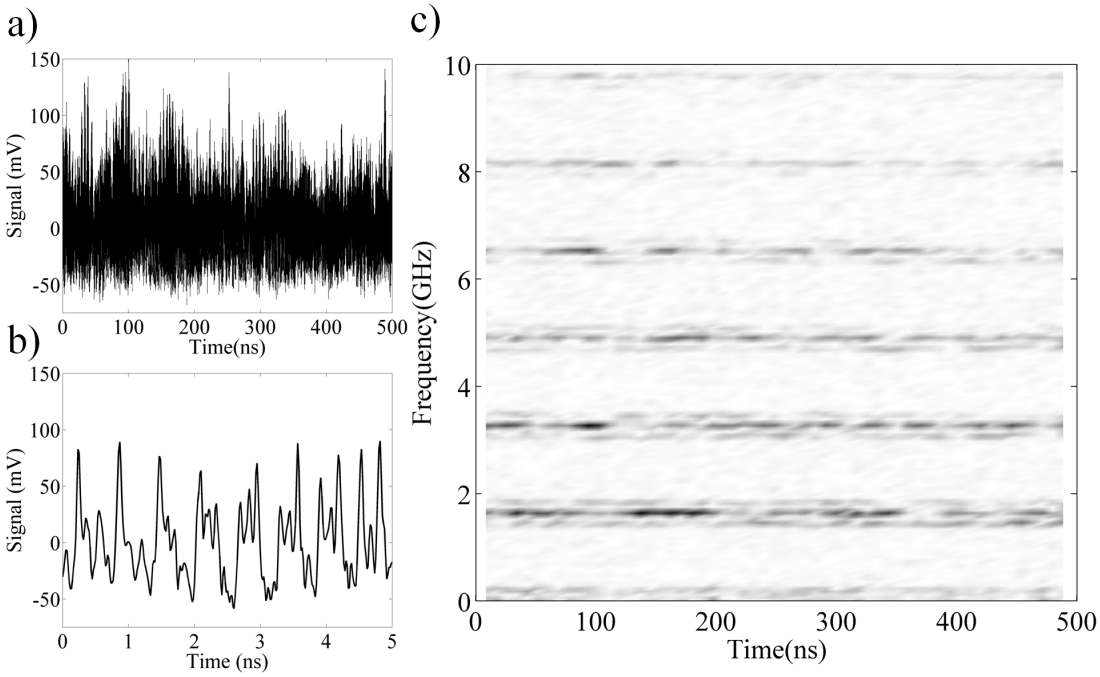

Figure 6.21: Time series obtained in a self-pulsing regime for a cavity round-trip frequency of 1.85 GHz. a) envelope, b) zoom on pulses, c) time-frequency spectrogram of intensity dynamics with 17.1 ns FFT window.

external cavity modes. These pulse-like dynamics are enhanced by a shorter external cavity and with the preference for oscillation on harmonics around 3–5 GHz it is believed that yet shorter cavities may yield even more regular, reproducible pulses. This behaviour is not common however, and by ramping the input current many diverse oscillatory states are possible with varying regularity, stability and frequency.

Temporal dynamics have also been investigated in numerical simulations based on the model outlined in Sec. 3.5 and while investigations are in the early stages, promising results are already being produced. In particular, time-traces which are qualitatively very similar to those seen in Fig. 6.21 have been produced and thus these simulations show great promise in being an ideal system in which to test external cavity parameters, bringing mode-locked, regularly pulsed LCS closer to realisation.

The key obstacle which this system faces is the ability to support multiple LCS

which are not only simultaneously bistable, but also simultaneously oscillating. A method in which to compensate for the inherent disorder such that several LCS may become simultaneously bistable is presented in a future section and is a clear step towards applications. The problem of multiple LCS which are simultaneously oscillating is still very real however. Currently the recipe to achieve oscillation is to probe the parameter space for a current which is seen to produce oscillations and achieving two simultaneously oscillating LCS should be a matter of cavity parameter distribution. If the spatial distribution of cavity resonance can be controlled there is hope however. If gain were only very weakly varying over the aperture of the device then a cavity which was approaching homogeneous in cavity resonance should be able to support multiple oscillating bistable LCS since the transition between external cavity modes should occur for the same nominal current for each LCS. Furthermore if the gain was not weakly varying, it may be possible to account for this by the compensation scheme through altering the effective cavity length. Such a compensation scheme shall be outlined and demonstrated in Sec. 7.2.

6.2.3 Perturbation Induced Transient Mode-Locking

During an attempt to switch an LCS to the off-state, an interesting effect was noticed. If the WB is shone directly on top of the LCS while in the on-state the LCS does not switch to the off-state, instead it displays strong, pulse-like dynamics. Fig. 6.22a displays the time-resolved measurements for one such event. The WB is set to produce two 30 ns long pulses separated by 40 ns and are shown in grey in Fig. 6.22a. The LCS (black trace in Fig. 6.22a) is on at the start of the trace and is in a non-oscillating steady state. Upon the application of the first pulse however the LCS begins to show strong intensity fluctuations which have an irregular envelope. This remains until the second pulse arrives, which has the initial effect of quenching the intensity fluctuations however when the pulse has ended the intensity fluctuations resume, with a similar irregular envelope. The LCS remains on at the end of the trace and it once again returns to the non-oscillating steady state at the end of the trace, or shortly after.

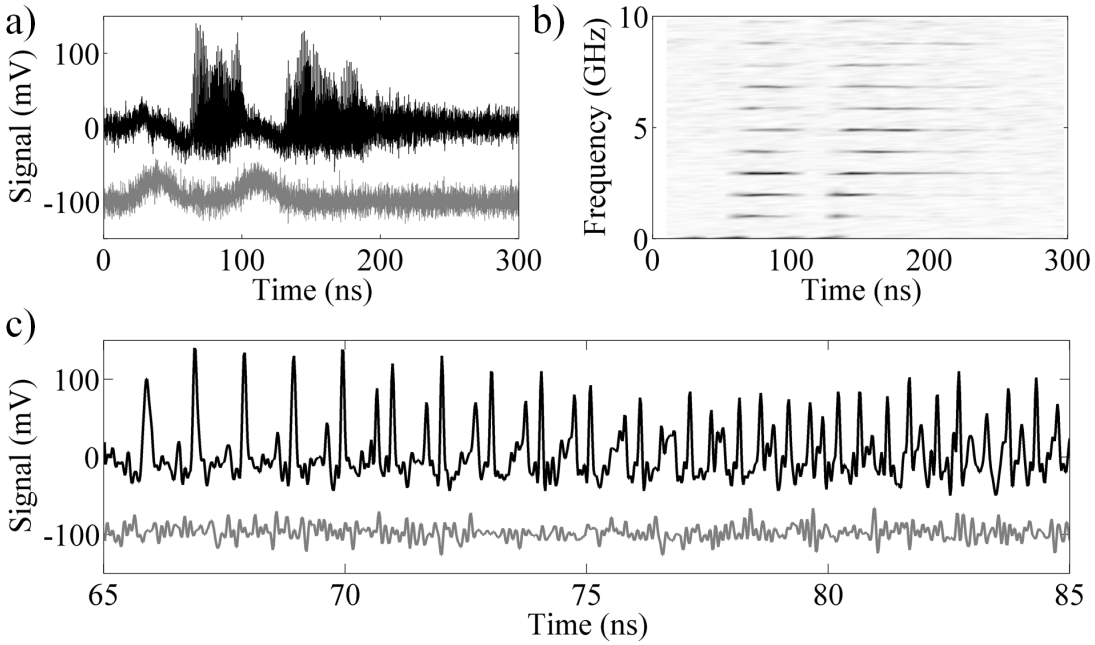

Figure 6.22: a) Time trace of the injected pulses (grey) and LCS response (black). The injected pulse is offset by 100 mV for clarity. b) Time-frequency spectrogram of the intensity oscillation frequency of the LCS response. c) Zoom of the temporal response of the LCS (black) to the injected pulse (grey). The injected pulse is offset by 100 mV for clarity.

Taking a closer look at the intensity fluctuations (Fig. 6.22c) it can be observed that quite well-defined pulse-like oscillations are excited. At the beginning of the pulse-like dynamics the separation between pulses is approximately 1 ns, i.e. at the external cavity round-trip frequency. However in the middle and particularly towards the end of Fig. 6.22c there are peaks appearing between those separated by 1 ns. This should be an indication that the recovery time of the gain is slightly faster than the external cavity round trip time, and again indicates that a shorter cavity would be more conducive to pulse-like behaviour.

The time-frequency analysis in Fig 6.22b shows that the temporal dynamics are a result of many oscillating frequencies being excited which are situated at the external cavity round trip frequency and its harmonics. Following the previous analysis this can be attributed to the excitation of many external cavity modes, however this cannot be measured directly in the current realisation as current

frequency measurements are too slow to see variation on this short timescale.

A tentative explanation of this phenomenon may be linked to a frequency perturbation. When the WB is applied to the LCS, the frequency of the LCS will red shift due to the removal of carriers by the writing beam. When the pulse intensity declines, the LCS should return to its original stable frequency. It has been shown previously that during switch-on the LCS frequency transitions through a cascade of frequencies associated with a branch of unstable soliton solutions (see Sec. 6.1.3.2), leading to the excitation of many external cavity modes before relaxing to either the steady state or an oscillating state, depending on parameters. This behaviour seems to occur not only for switch-on but is also consistent with these observations of a perturbed LCS in the on-state. It is therefore thought that these pulse-like dynamics are the result of the LCS frequency being perturbed by the WB and returning to the stable LCS frequency via a branch of unstable soliton solutions. This hypothesis is corroborated by the effect of the second pulse. The oscillation induced by the first pulse is stopped by the application of the second pulse, when the LCS frequency is perturbed once again by the application of the WB. The removal of the WB once again leads to strong dynamics consistent with the behaviour of the first. The timescales of oscillation are also consistent between the switch-on dynamics and these pulse-like oscillations, both of the order 100 ns, making for a convincing mechanism.

There is a question however as to whether the LCS transitions through a branch of unstable soliton solutions (as shown in Fig. 4.21) on the red side of the grating peak, or the previously observed unstable soliton solutions on the blue side. In principle there should be another set of such solutions on the red side of the grating peak and since the removal of carriers shifts the LCS to the red, it seems most likely that the LCS transitions back through these solutions, causing similar dynamics to that seen from the switch-on by a WB. Another possibility exists however, and that is that the WB destabilises the LCS, effectively switching it off. Upon removal of the pulse the WB would act to write the LCS again, resulting in the previously documented switch-on transient dynamics.

6.2.4 Switching to Oscillation

While it has been shown that the LCS can show pulse-like temporal dynamics while varying the current parameter, it would be far more relevant for applications if the LCS could be switched on to this oscillating state, while also remaining independent. Indeed it is possible for an LCS to end in the oscillating state after a spontaneous switch-on. This is shown in Fig. 6.23 and is the result of increasing the current until an LCS spontaneously appears i.e. there is no application of the WB. At the switch-on point there is a large peak in intensity which is accompanied by many modes becoming excited in the time-frequency analysis. These modes then die out until 5 μs after the switch, there is only one dominant mode remaining, corresponding to an intensity oscillation at close to 5 GHz. It should be noted that the detector used here is AC-coupled, leading to the slow rejection of the DC component of the LCS which results in the slow attenuation back to zero DC and this is not an amplitude decay of the LCS. Thus the general behaviour of spontaneous switch-on seems to follow the dynamics outlined in Sec. 6.1.3.1 for a switch-on induced by an external pulse. There are however rather pronounced pulses during the initial switching, as seen in Fig. 6.23b which seem to be due to the locking of many modes excited at switch-on, however these are short lived due to the de-phasing or decaying of the modes. This pronounced pulsing during spontaneous switch-on is not new however and is found in the previous CSL utilising a diffraction grating [127] and also the face-to-face VCSEL configuration [42]. Here however after the initial transient oscillations there remains a strong frequency component at 5 GHz, indicating a stable oscillating LCS, and indeed if the end of the trace is inspected more closely oscillation can be observed (Fig. 6.23d) indicating a switch-on to an oscillating LCS.

This spontaneous switch to oscillation is however insufficient for applications since there is no opportunity to switch this LCS off again, owing to the fact that it is no longer within the bistable range. It is therefore important to outline the criteria which an LCS should adhere to for maximal use in applications. Ideally there should be multiple LCS which share a bistable range, such that they may be switched on and off without changing the VCSEL parameters. They should be able to be switched on to an oscillatory state which is stable and do so in such

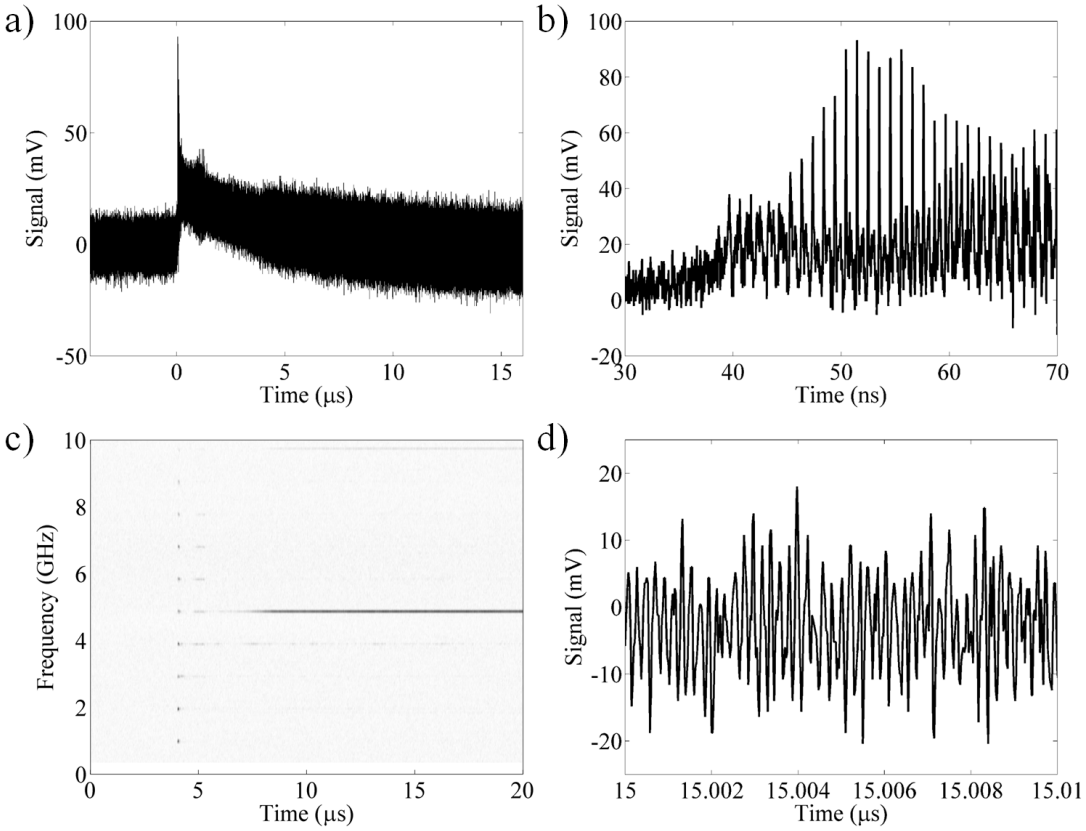

Figure 6.23: a) Time trace of an LCS during a spontaneous switch-on event. b) Zoom of the temporal dynamics in (a). c) Time-frequency analysis of the temporal dynamics in (a) with a 17.1 ns time window and 50% overlap between windows. d) Zoom of the temporal dynamics at the end of the trace.

a way that it does not alter the state or oscillation of the other LCS in the system and should be able to be switched off.

With these criteria in mind, two simultaneously bistable LCS are found and their independence is confirmed by the ability to switch each without effecting the state (on or off) of the other. To switch to an oscillating state the LCS is switched on by increasing current and then the current is reduced until several optical modes are excited and the LCS is found to be oscillating. This is necessarily in the bistable range of the LCS since the VCSEL is now biased below the spontaneous switch-on threshold. The LCS is then switched to the off state by interrupting feedback. The LCS is then switched on by injection of the WB in the normal

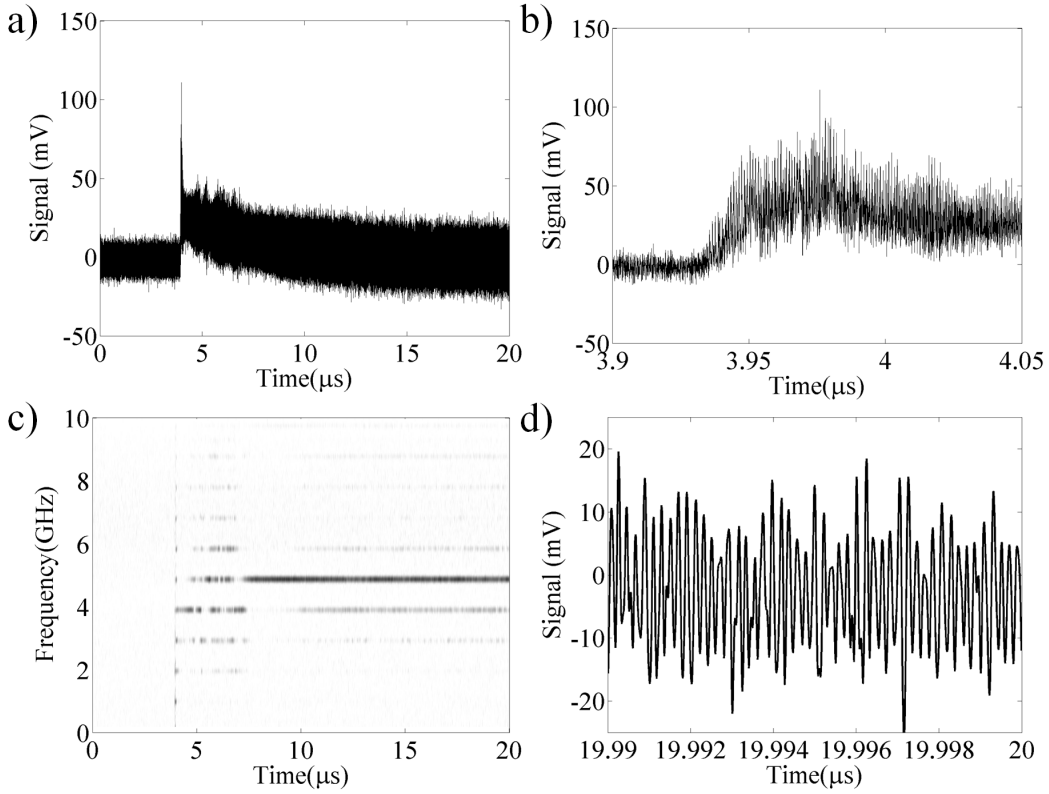

Figure 6.24: a) Time trace of an LCS during a switch-on event induced by the WB. b) Zoom of the temporal dynamics in (a) around the switching point. c) Time-frequency analysis of the temporal dynamics in (a) with a 17.1 ns time window and 50% overlap between windows. d) Zoom of the temporal dynamics at the end of the trace.

way and is hoped to return to its previously oscillating state. The result of such a switch is shown in Fig.6.24 and it can be seen that the switch is accompanied by the typical switching dynamics outlined previously, however here it can be seen that the LCS settles to a state with a dominant oscillation at around 5 GHz. Closer inspection of the temporal dynamics at the end of the trace (Fig. 6.24d) reveals a steady oscillation at this frequency. This demonstration means that this LCS satisfies the first criteria, that it may be switched to an oscillating state.

The independence of this switch to oscillation was proven rigorously by monitoring the location of a second LCS. This is achieved by using 2 fibre-coupled detectors. The alignment of the LCS to the fibre gives spatial resolution such that

each LCS is coupled to its own fibre, with a cross-talk between fibres lower than 1%. Both LCS were found to switch to an oscillating state, albeit for differing currents with the other remaining off. Next the LCS were shown to switch to the oscillating state (once again for differing currents) while the other was in the on state and was found to remain in the on state.

The most rigorous test would be to place an LCS in the oscillating state and have the other switch to an oscillating state without affecting the dynamics of the first, such that both end in the oscillating state. This proof is not possible in the current experimental setup however. Due to the fast nature of the dynamics, two detectors with temporal bandwidth of 5 GHz and upwards are required. The above experiments were conducted with one such 12 GHz bandwidth detector (outlined in Sec. 3.4.5) and a 1.2 GHz bandwidth APD (see again Sec. 3.4.5). It is therefore not possible to detect whether both are oscillating at the same time, unless one is oscillating at the fundamental cavity trip round time, and this is very rare. Although this result is not currently attainable, it is not foreseen to be impossible, however and should only rely on finding the appropriate parameter regime such that both LCS are oscillating for the same VCSEL bias current.

6.2.5 Conclusion

The occurrence of pronounced, fairly regular pulsing multi-frequency LCS indicates that the external cavity modes are at least partially phase-locked, i.e. there is mode-locking of spatial LCS. In the present stage quantitative information on the modulation depth cannot be given but the very existence of pulses indicates the existence of structures significantly shorter than the cavity round-trip time. Hence, the observation of cavity light bullets is concluded, probably on an irregular non-zero background. There is also the first demonstration of an LCS switching to an oscillating state, which is a step towards potential applications.

Oscillating or pulsing cavity solitons have been found in the face-to-face VCSEL system, however there the structures which are oscillating are no longer bistable and thus not cavity solitons. More promising results are found in more recent work on a monolithic semiconductor micro-cavity with saturable absorber [34].

The FSF does not have an obvious mechanism as saturable absorption to induce mode-locking, but, for example, four-wave mixing is known to support mode-locking in lasers [95]. A better understanding of their properties might enable further optimisation and stabilisation thus paving the way for carrier pulse trains on demand for the use in future all-optical networks.

Chapter 7

Laser Cavity Soliton Control

7.1 Disorder Mapping

Translation is a neutral mode of an LCS, i.e. the LCS in a CSL should have no preference for position and therefore should be able to exist anywhere within the laser aperture. Furthermore the CS should be able to be moved by externally applying phase or intensity gradients and can also be pinned or positioned by the same means. This is promising for future applications since the positioning and movement of the LCS has the potential to be dictated by external control.

Numerical simulations in an optically pumped amplifier system show that in the presence of a periodic phase modulation, such as a sine variation that the LCS are attracted towards the peaks, and are stabilised in position at this peak [70]. If more than one LCS is attracted then there is an annihilation at the point at which the LCS meet, leaving only one. If a 2D periodic modulation of phase is applied then the LCS would be pinned in a 2D array [70] which when combined with the bistable nature of LCS makes itself an ideal candidate for optical memory applications. If then a line trap was produced and then an phase gradient superimposed along the direction of the line, it is predicted that the LCS should be confined within the line and furthermore spontaneously drift along the line in the direction of the gradient. A potential application for this would be a so-called 'all-optical delay line' [88] in which LCS would be injected to one side of the device and then drift under the influence of the gradient to the other side

of the device where it would be read out again. In this way a data stream could be converted to a spatially separated line of drifting LCS which would travel at speeds significantly less than the speed of light, hence creating a delay between writing and reading, acting as a buffer, which is needed for all-optical networking applications. This scheme was implemented experimentally [88] but the drift distance was limited, and it will be seen that some sort of random disorder is responsible for this limitation.

These simulations however assume a homogeneous cavity (apart from the intentionally applied spatial variations) and this assumption breaks down in real devices. In a homogeneous cavity the CS are predicted to be able to exist anywhere within the transverse aperture of the system, however since translation is a neutral mode, any small perturbation would cause the LCS to drift until they are locked to or destroyed at the boundary. Real devices always contain imperfections in the form of a spatial distribution of cavity parameters which will cause the LCS to begin to drift. The imperfections are not uniform however and the LCS will drift until they reach a local minima of the perturbation and become trapped there. This is demonstrated in experiments as the CS always appearing in the same position. While small displacements from this initial position are possible, they have limited range and the range differs from LCS to LCS indicating that the size and strength of the traps are varying across the aperture of the system. Each CS also has a different threshold which is not predicted by the theory and should also be due to the spatial disorder. This spatial variation of cavity parameters will henceforth be referred to as 'disorder' or 'defects'.

Previous work performed in semiconductor micro-cavities reported micron-scale cavity parameter variations (disorder) which were shown to play a role in pattern selection in semiconductor micro-cavities [63]. Investigations into broad-area VCSELs also indicated that the spatial coherence of on-axis emission is limited by an uncontrolled spatial variation of cavity parameters [10, 105]. Disorder limits also the coherence of VCSEL arrays [90].

It is important to consider which parameter variation actually lead to the trapping of LCS. There seems to be two key candidates, gain (or absorption) variations and cavity resonance variations. If there were small gain variations across the aperture of the device then there should be a visible modulation of the

spontaneous emission distribution below threshold and this is not the case (see the background spontaneous emission in Fig. 4.3 for example). The gain is not totally homogeneous however, as the gain is increased near the boundary of the device due to current crowding (see Fig. 3.3a). The gain variations induced by current crowding are smooth variations over some 100 μm and hence too large to be responsible for the pinning of LCS. The gain variations induced by current crowding is responsible for the boundary lasing modes at threshold in the free-running laser (Fig. 3.3b-d) and similar behaviour is also found when feedback is provided to the VCSEL via a plane mirror, that is, lasing in the centre of the device does not occur at or around threshold.

The situation changes drastically however when frequency selective feedback is applied. Fig. 7.1 shows the evolution of lasing across threshold and for increasing currents. The first spots to lase (the LCS) do not appear at the boundary, and the boundary only begins to lase for very high currents. Following the argument for the switching mechanism outlined in Sec. 4.6 and Fig. 4.21 if the cavity had a homogeneous distribution of cavity resonance, then all LCS should reach threshold at the same current. What can be seen from Fig. 7.1 is that each LCS has a different threshold and this can be interpreted as a spatial variation of cavity resonance (or 'trap depth') which can be envisaged as the dotted curves in Fig. 4.21. Not only does this interpretation offer a mechanism for the separation of LCS thresholds but also for their frequency detuning and thus it is concluded that the 'spatial disorder' or 'defects' consist of a (effective) cavity resonance distribution (phase) defect, rather than a gain/absorption (amplitude) defect.

This spatial disorder has crucial implications for applications which require positioning and translation of CS since these properties would be controlled by the random disorder induced during growth, rather than being controllable. It is therefore crucial to obtain an understanding of the mechanism of this disorder, measure it, and then try to compensate for it in some way in order to return to a more ideal situation, more suitable for applications and these aspects will be explored in this chapter.

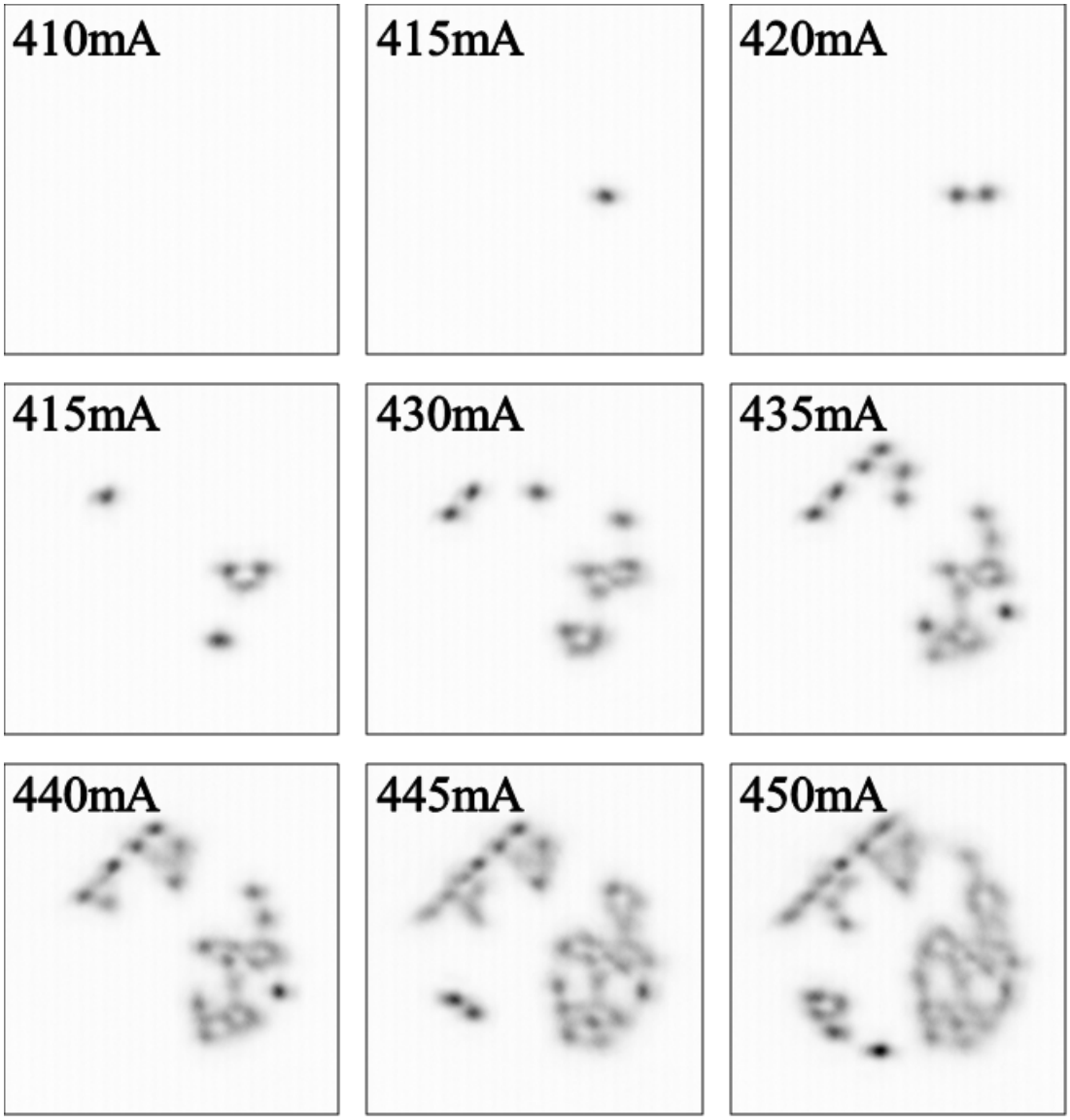

Figure 7.1: Negative intensity (black corresponds to high intensity) near field images of the VCSEL gain region. Pictures taken at the inset currents.

7.1.1 Cavity Resonance Scan

Since the effects of the spatial disorder seem to be consistent with a cavity resonance variation the most obvious measurement seems to be to measure the VCSEL cavity resonance with spatial resolution. This is achieved by injecting a spatially homogeneous (plane wave) external laser into the VCSEL cavity. From here,

two approaches are possible, either the laser cavity resonance can be scanned, by either temperature or current tuning, or the frequency of the external laser can be scanned, whichever method is most easily controllable, with sufficient resolution. At each detuning point during the scan an image of the near field of the VCSEL is taken, if the external beam is locally resonant with the VCSEL cavity then the external beam will experience a cavity enhancement and show as a brighter portion of the VCSEL in the near-field image. The images are then combined to create a map of the VCSEL cavity resonance.

There are two problems with this approach, the first is that the external beam can be approximated to be a plane wave if the beam is expanded sufficiently. The beam will never truly be homogeneous, however this may be corrected for of the beam shape is known. The second problem is that this system is extremely sensitive to alignment due to the Fabry-Perot cavity of the VCSEL. This means that similar measurements between two devices, or indeed repeatable measurements within the same device are difficult [14]. Though there are issues, this technique is still very powerful, and has been performed successfully in semiconductor microresonators [63].

Though powerful, the limitations of repeatability and requirement of an external tunable laser lead to the consideration of alternative methods. Perhaps one which probes directly the behaviour of LCS and which may be used in conjunction with the resonance scan to gain further insight into the factors which work to affect the LCS positioning and movement. This measurement is outlined in the next section.

7.1.2 Soliton Force Microscope

The principle of a soliton force microscope (SFM) measurement relies on the idea that when a CS is formed it is pinned at a local minimum or maximum of a spatially varying cavity parameter. One can then imagine that the CS is confined in a 'trap' and it sits in this trap until it is perturbed. If the CS is perturbed by small amounts such that it is still stably existing within it's trap, but moved by a small amount then a map of this trap could be made by perturbing the CS in all directions and noting how far the CS is able to move. Such experiments

were performed in the optically pumped amplifier systems [89] where the CS were dragged and perturbed by stripe like modulations and rotation of the HB. If a quantitative approach could be taken towards this, then a map could be produced where a small movement would be interpreted as a steep, more strongly confining trap, whereas a large movement would be interpreted as a weak trapping mechanism.

This system has the inherent advantage that no assumptions towards the mechanism for trapping need to be made since the LCS themselves are present and all trapping factors are acting. The downside is that the area which may be mapped is reduced due to the relatively small coverage of LCS in most CSL systems.

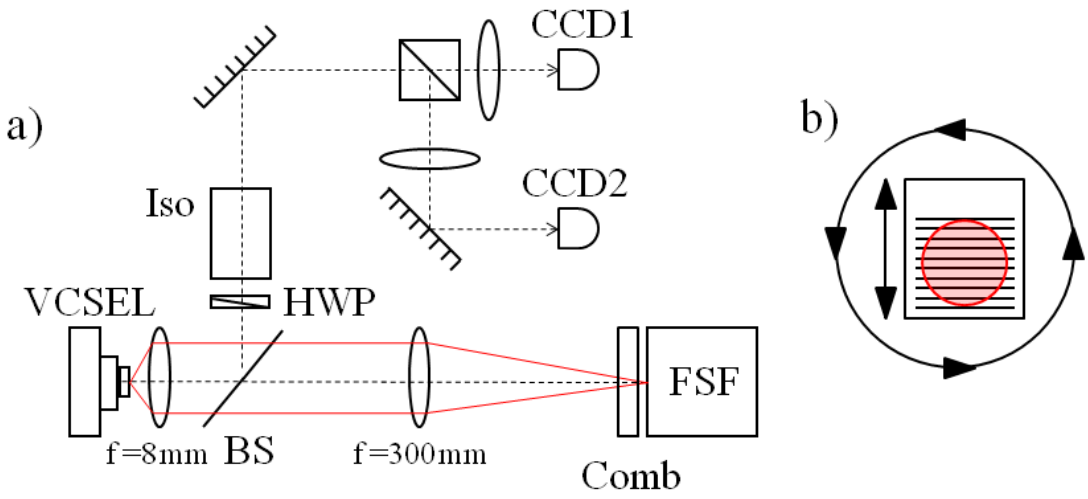

Figure 7.2: a) Experimental setup. VCSEL: Vertical-cavity surface-emitting laser, BS: Beamsplitter, Comb: Spatial comb filter, transverse view in Fig. 7.2(b), FSF: Frequency selective feedback, Iso: Optical isolator (Faraday rotator), HWP: Half-wave plate, CCD1: CCD camera in near field image plane of VCSEL, CCD2: CCD camera in far field image plane of VCSEL. b) Schematic view of the comb filter. The circle indicates the size of the re-imaged near field compared to the comb. The arrows indicate the degrees of freedom that the comb may be turned through. Comb lines are 600 μm wide and separated by 500 μm.

The experimental setup for an SFM measurement in s CSL is shown in Fig. 7.2. To perform the SFM measurement an external cavity and frequency selective feedback (FSF) element is added to the VCSEL which is to be measured such

that it forms a CSL. In the experiments in optical amplifiers with optical injection, the HB was modulated with a stripe pattern and passed over the CS, to perturb them in one direction. Since in the laser case there is no HB, another approach is required. The method used to perturb the position of the LCS is simply a 'comb', a metal plate with lines removed from it which may be translated and rotated. This should act similarly to the striped HB, by removing feedback in a stripe pattern, suppressing the formation of LCS along those lines. This apparatus is rather bulky however and requires the external cavity to be larger than previously and so a 71.6 cm external cavity is used.

To perform the measurement the CSL is first operated without the comb, and tuned to produce the maximum amount of LCS. The comb is then inserted as close to the FSF element as possible to place it in the re-imaged near field plane of the LCS. The comb obscures the feedback in stripe patterns, such that the LCS may only form on the stripes which are not obscured by the comb. Once the LCS are formed they may be perturbed in position by translating the comb perpendicular to the stripe direction. The LCS can either switch off due to lack of feedback or it can adjust to the perturbation by moving in position to a new location which is still receiving feedback. In this way it is possible to find the range of motion of each LCS to build a map of the disorder.

The whole experiment involves recording the position (i.e. taking a picture) of all lasing patterns and LCS for a position of the comb and then incrementally moving the comb while recording the lasing for each position. Then the comb is rotated by 10° and the pictures taken for each translation. This is repeated such that there is a picture for every possible translation and each rotation up to 180°. Once this is done the pictures are all superimposed upon each other and re-normalised. This produces a picture which shows the range of motion of all LCS and gives insight into the strength and shape of the defects pinning the motion of the LCS. Two such defect maps for the same VCSEL are shown in Fig. 7.3 and Fig. 7.4 for two different selections of frequency selective feedback element; a diffraction grating and a volume Bragg grating respectively.

The SFM map shown in Fig. 7.3 was formed by using a diffraction grating with 1800 g/mm (Newport plane-holographic grating) and shows that there are two strong straight traps present in this device, known as 'line defects'. In the

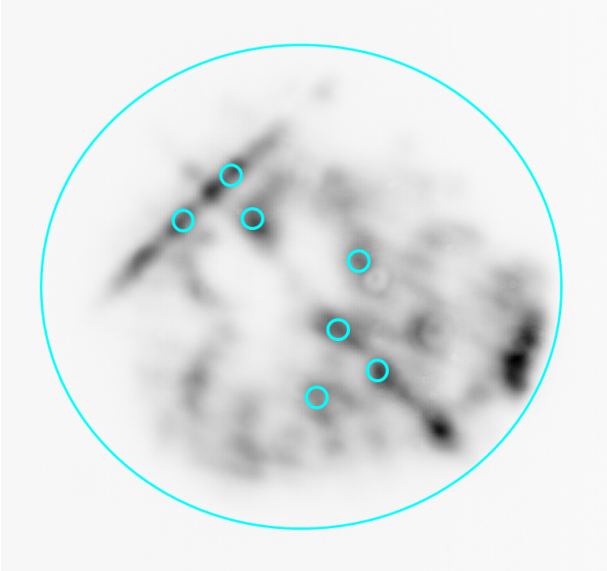

Figure 7.3: Final soliton force microscope image for the setup with diffraction grating as frequency selective feedback element. This image is the sum of all measured positions and rotations of the comb and then re-normalised to maximum intensity. The circles show the position at which several LCS are found.

top left portion of the device, there is one such line running lower left to upper right, and is shown to include the position of two LCS. The dark region along the line indicates that the LCS have some freedom to move and form along the line, however there is a strong pinning in the orthogonal direction, evidenced by the lack of pattern, particularly above the line. The second line runs top left to bottom right and is home to three LCS. This line appears less strongly confining however, as there are patterns on most sides of this line. It should be noted here also, that there are no patterns in the central portion of the laser, and a dark region which does not correspond to any LCS on the right hand boundary. This should be an effect of the anisotropy of the diffraction grating creating a wavefront tilt leading to a drift of the lasing pattern in one direction (In this case to the right).

The map produced while using a VBG as FSF element is shown in Fig. 7.4. It is immediately apparent that the spatial area mapped by this method is significantly smaller than the previous case, however the general shape remains rather similar with the existence of 'line defects' and the tendency to avoid the centre.

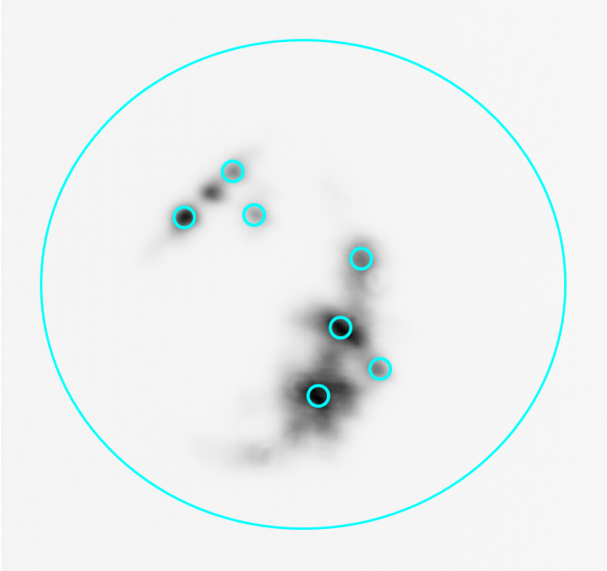

Figure 7.4: Final soliton force microscope image for the setup with volume Bragg grating as frequency selective feedback element. This image is the sum of all possible positions and rotations of the comb and then re-normalised to maximum intensity. The circles show the position at which several LCS are found.

The SFM map produced using a diffraction grating (Fig. 7.3) has a greater area of the VCSEL aperture mapped than the map taken while using a VBG and thus would seem to be the better choice for SFM mapping. It is certainly true that more of the aperture is lasing but a lesser proportion is actually producing LCS, instead the majority of lasing patterns are spatially extended, low amplitude, non-bistable lasing modes. While these serve to extend the range of the mapping spatially they do not shed any light on the factors influencing LCS formation.

This SFM technique is clearly an excellent technique to probe the limits of LCS existence and thus gives valuable information about the spatial variation of parameters, in particular the most reddish parts of the cavity. There are drawbacks to these methods however and both have their limitations. The diffraction grating case is contaminated by unwanted patterns and is sensitive to the angle of comb rotation. Likewise the VBG case produces very limited mapping due to the very strongly confined LCS. Both approaches also suffer from a lack of any quantitative results, as the grey-scale has essentially no real weight or meaning. Furthermore the experiment is rather long to record and quite manpower

heavy and also requires the laser to be tested in a separate system and with the future goal of making monolithic CSLs, this method would not be possible. Therefore yet another method is sought after, one which is capable of mapping the whole device and hopefully also providing some quantitative results on the cavity length variation while also reducing manpower requirements and allowing 'in experiment' testing.

7.1.3 Current Ramp with FSF

In Sec. 7.1 it was argued that the spatial distribution of parameters was responsible for the separation of thresholds of each LCS. It should therefore be possible to obtain an idea of the distribution of this disorder by measuring the spatial distribution of thresholds in the presence of FSF. The principle of this measurement is based on the switch-on mechanism outlined in Sec. 4.6. This states that the parts of the cavity which are more closely detuned to the grating will begin to lase first when the current is increased in the presence of FSF. As the current is increased new areas of the cavity will begin to lase until at some high current the whole aperture is lasing. If a picture is taken at each current then a map of the cavity can be produced by analysing at which currents each location starts to lase. This is simply an extension of Fig. 7.1, and if such a series of pictures were taken for every possible current then a spatial map of the thresholds, and thus cavity resonances could be produced.

The main advantage of this experiment is that it may be conducted very easily once the CSL is set up, it is fast and easily automated, and can be performed even for monolithic devices containing laser and feedback in one package. Furthermore the spatial coverage of the measurement is very high, and only limited by the upper safe operating current of the device, and the spatial coverage of lasing at this current.

The result of the mapping corresponding to the same realisation as in Fig. 7.1 is displayed in Fig. 7.5. The map is generated by biasing the VCSEL just below the threshold for the first LCS. The current is then increased in 1 mA increments and at each current the near field intensity distribution is recorded via the near field camera. When all images are taken they are analysed by a MATLAB program.

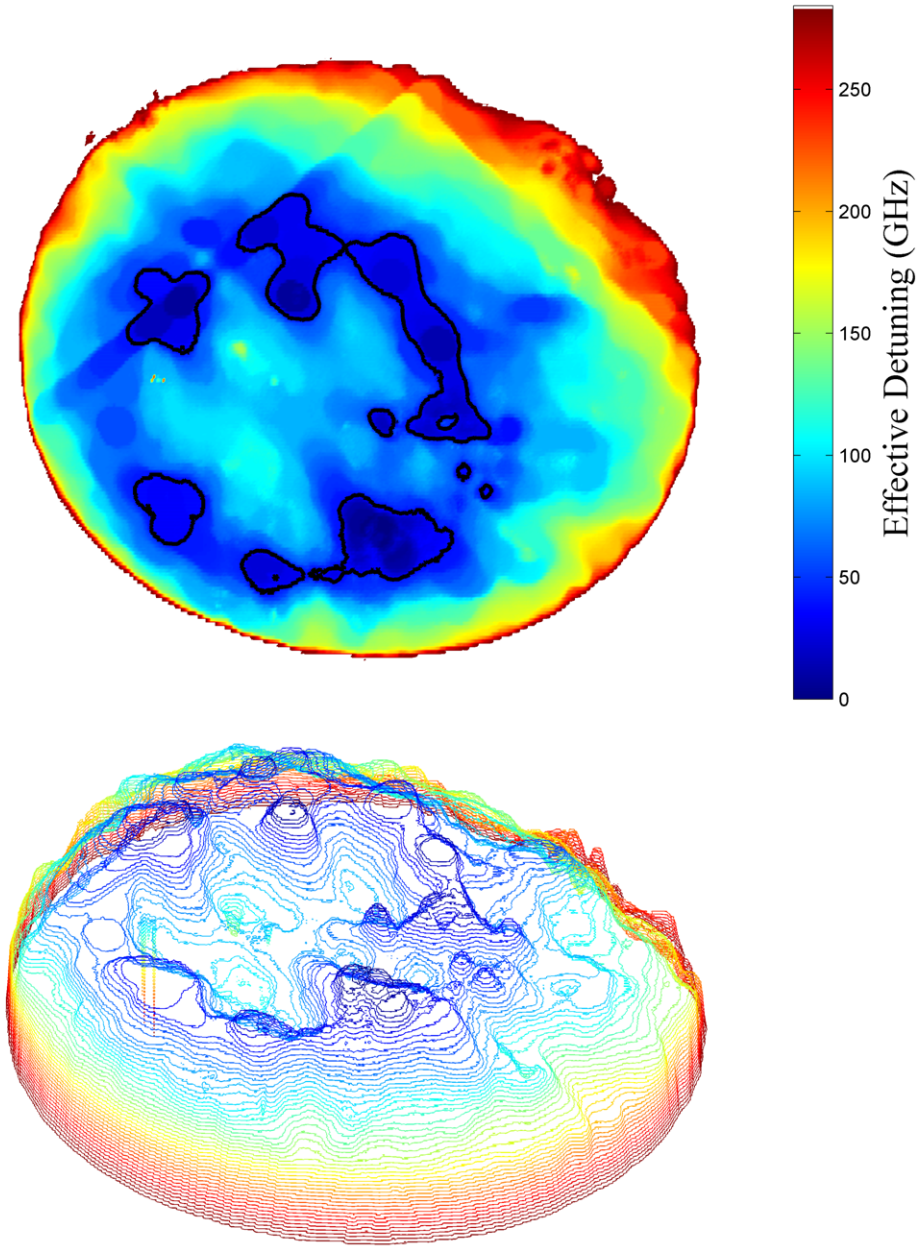

Figure 7.5: Map of how the effective cavity resonance varies spatially across the aperture of the main VCSEL used in the previously discussed CSL. The black contour corresponds to an effective detuning of 40 GHz and marks the limits of LCS formation. The blue circular extremes mark the laser aperture boundary and has a diameter of 200 μm. The contour plot is a 3D representation of the upper picture.

The purely spontaneous emission images are disregarded and starting from the threshold of the first LCS the images are converted from greyscale to a binary black and white image with the intensity cutoff at the $1/e^2$ point of intensity. All of these binary images are then added together to produce one image in which the parts of the cavity which begin to lase first have the highest value and vice-versa. This is then normalised to detuning using the known detuning rate of 0.0035 nm/mA. Note that this is actually effective detuning since other factors are in play such as gain variations and temperature gradients which also effect the threshold of each part of the cavity, not only cavity resonance though the main effect is believed to be cavity resonance fluctuations as indicated. The black contour in Fig. 7.5 shows the final frequency at which an LCS is formed and corresponds to a detuning of 40 GHz, still within the frequency selective feedback peak, but outside the full-width half-maximum value of approximately 30 GHz.

From this map it can be seen that the map follows the same trends as the previous SFM measurements. In all measurements (Figs. 7.3,7.4 and 7.5) there is a tendency to disfavour lasing in the centre portion of the VCSEL. There are three main factors which influence the cavity resonance variation over the aperture of the VCSEL; temperature gradients, carrier density fluctuations and a built-in decay which arises from manufacturing imperfections. Analysis of large-area bottom emitting VCSELs shows that there is a radial temperature distribution which decreases towards the boundary [73], which in this case should bring the centre of the device into resonance first, favouring lasing in the centre of the device. The carrier density should also be higher at the boundary due to current crowding (see /[73] lowering refractive index there and therefore shifting the boundary to higher frequencies, favouring low threshold operation at the centre once again. The built-in disorder should in theory be random therefore the tendency to lase in a ring around an disfavoured central portion is not expected. There are two possible explanations, the first is that the thermal effect of the current crowding dominates the carrier effect, shifting the cavity resonance to higher wavelengths, favouring boundary threshold lasing. The second is simply that the built-in variation is strong enough to dictate lasing on a ring rather than central lasing as expected. The carrier and thermal effects are however smooth variations and the

fine structure which is shown in the map is almost certainly due to the cavity resonance variation discussed previously.

Particularly notable in all three mapping experiments is the appearance of the two perpendicular line defects. They are shown to be an attractor for LCS, trapping LCS and confining them quite tightly, as demonstrated by the movement limitation shown in Fig. 7.4. The origin of these line defects is unclear but can be conjectured to be the result of either a shearing of the semiconductor layers during growth or due to damage induced during the mounting procedure.

The main differences between the three mapping measurements is the amount of spatial coverage of the map. The SFM measurement with VBG (Fig. 7.4) has the least overall coverage which is a disadvantage for a measurement of the entire VCSEL but has the advantage that unlike the other measurements it probes the factors influencing the LCS directly. The current ramp with FSF and SFM measurement with the diffraction grating have greater coverage of the VCSEL aperture but they have some key differences. The preference for lasing on one side manifests itself as a preference for lasing on the right hand side of the device, and is manifest as a dark spot on the right hand side of fig. 7.3. This is not present in Fig. 7.5 which supports the conclusion that it is an artefact of the parity-breaking of the diffraction grating. The current ramp with FSF has the greatest coverage of all, has isotropic feedback, is fastest, completely automated and could be performed in arbitrarily small external cavities and thus appears to be the best technique for mapping the distribution of spatial disorder in a CSL.

7.2 Compensation using a Spatial Light Modulator

The future applications of these systems are limited by this spatial disorder and it is therefore crucial to achieve an understanding of it and to attempt to compensate for it. It has been shown in the previous sections that the spatial disorder is primarily a spatial variation of cavity resonance and this acts to give each LCS different threshold and frequency, limiting the number of simultaneously bistable

CS, and pinning to specific locations, all of which severely limit potential applications.

7.2.1 Concept of Disorder Compensation by Induced Refractive Index Changes

The spatial disorder may be compensated for by spatially modulating the effective (i.e. averaged over the longitudinal structure) refractive index $n(x, y)$ of the VCSEL cavity to compensate for the spatial disorder in cavity length $L(x, y)$ (in reality, the VCSEL will have spatial disorder in refractive index and layers thicknesses but it is sufficient for our purposes to speak of an effective cavity length $L(x, y)$ alone):

$$n(x, y) = \frac{m\lambda_0}{2L(x, y)}, \tag{7.1}$$

where m is the mode order and λ_0 the design vacuum wavelength. This compensation can be achieved by injection of an external laser beam. This beam would alter the number of carriers, altering the refractive index via phase-amplitude coupling as described phenomenologically by Henry's α-factor [55]. In quantum well materials, decreasing the carrier density results in an increase in refractive index. This refractive index change alters locally the optical path length, resulting in a cavity resonance shift as desired by Eq. (7.1).

In order to achieve spatially resolved compensation, an injection beam with spatially varying intensity is required and thus the injection beam is combined with a spatial light modulator (SLM). The principle would be to obtain the map of the cavity defects by the methods outlined in the previous section, and then impose a spatial modulation of intensity such that 'deep' and 'shallow' traps receive different amounts of compensation, as illustrated in Fig. 7.6.

7.2.2 Experimental Setup

Figure 7.7 shows the experimental setup, which has three main components; a cavity soliton laser, a compensation beam and a detection arm. The cavity soliton laser is composed of a broad-area VCSEL with frequency-selective feedback from a VBG. The VCSEL is nominally the same design is the device which has been

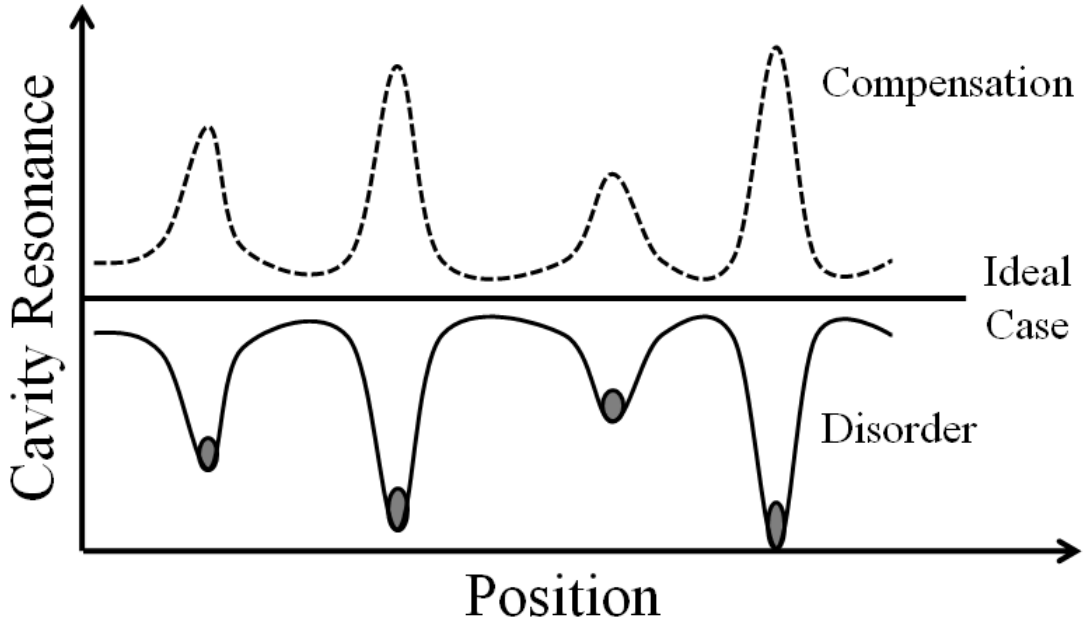

Figure 7.6: Sketch of the spatial variation of cavity resonance in a VCSEL. The straight central line represents the situation for an ideal plano-planar cavity. The lower line indicates how the resonance might vary in a real laser. Grey dots indicate CS pinning regions (traps). The dotted line corresponds to the externally injected laser beam intensity modulation required to compensate for the cavity resonance variation shown by the lower line. Wavelength increases from bottom to top, threshold decreases.

used until now, however it is mounted on a TO-56 submount. It has a 200 μm diameter circular aperture and is temperature tuned to have a cavity resonance at around 978 nm in order to approach the reflection peak of the VBG which is centred on 978.2 nm and 0.11 nm wide. The VCSEL and VBG are coupled via an external self-imaging cavity with length 61.6 cm [129].

The compensation beam is derived from a spatially modulated edge-emitting laser (EEL) diode. The diode emits at wavelengths around 978 nm and its wavelength is tunable via temperature. The beam from the diode is collected by a collimating lens and then circularised by an anamorphic prism pair. The circular beam is then expanded to a radius of approximately 10 mm. This large beam is then horizontally polarised by a polarising beamsplitter cube. Afterwards the beam is spatially modulated by a Holoeye LC 2002 transmissive spatial light

modulator (SLM). The SLM has a design wavelength of 532 nm, however some modulation is still present at 980 nm though it is smaller than 15%. This lack of modulation will turn out to be a significant restriction on the performance of the system. The total optical power which reaches the VCSEL front mirror is <1 mW when the whole SLM is set to transmit. The transmission aperture is 25.6 mm × 19.2 mm and contains 800 × 600 pixels.

The SLM induces a spatially modulated polarisation rotation upon the incident beam and when placed between crossed polarisers, the rotation is converted to an intensity modulation. After the beam passes through the SLM, it is demagnified to match the size of the VCSEL aperture and coupled into the cavity soliton laser (CSL) cavity via a polarising beam splitter. A consequence of the polarisation sensitive injection is that the compensation beam does not propagate in the external cavity. This however also means that the compensation beam is not visible in the detection arm. To align the compensation beam we therefore have to place a quarter-wave plate before the VCSEL in order to see the alignment of the compensation beam in relation to the VCSEL aperture. The quarter-wave plate is removed when the experiment commences. Note that there is no coherent interaction between the beam propagating in the external cavity and the compensation beam even if they are close in frequency because they are orthogonally polarised.

An example of the effect and resolution of the compensation beam is shown in Fig. 7.7a and Fig. 7.7b. If we apply the image shown in Fig. 7.7b then the modulation shown in Fig. 7.7a is achieved at the VCSEL surface. The circular disk seen in Fig. 7.7a is the 200 μm diameter aperture of the VCSEL showing spontaneous emission below threshold. The entire aperture is not illuminated by the EEL beam in order to achieve a reasonable compromise between intensity and spatial range covered.

The detection system is isolated from the laser cavity by an optical isolator. A photodiode records time-averaged intensity and two charge-couple device (CCD) cameras monitor the re-imaged near and far field planes of the VCSEL cavity.

Two choices for external laser wavelength are apparent. The first choice would be to use a beam with a frequency outside the stop-band of the Bragg mirrors

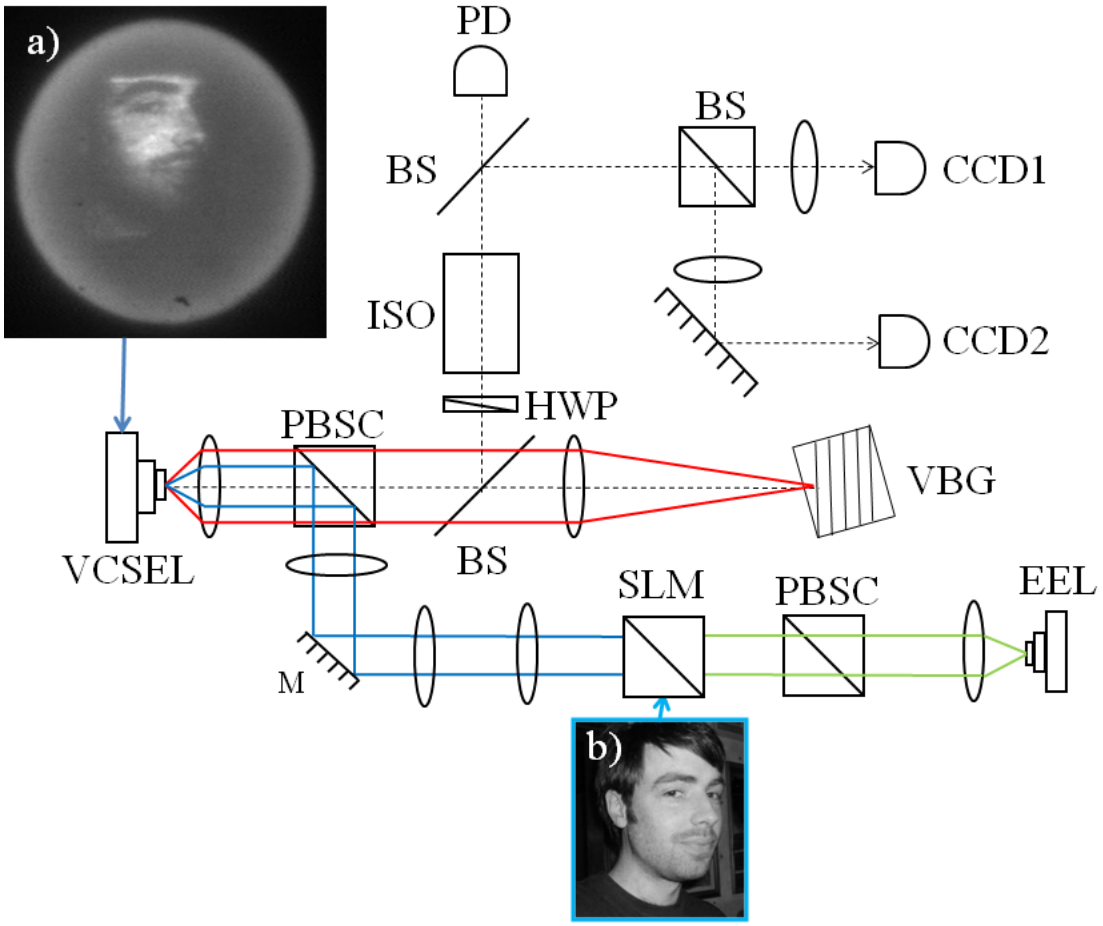

Figure 7.7: Experimental Setup. VCSEL: Vertical-cavity surface-emitting laser, BS: beam splitter, VBG: Volume Bragg grating, PBS: Polarising beam splitter, HWP: Half wave plate, QWP: Quarter wave plate ISO: Optical isolator, PD: Photodiode, CCD1(2): Charge coupled device camera imaging a near (far) field plane of the VCSEL gain region, EEL: Edge emitting laser, SLM: Spatial light modulator, APP: Anamorphic prism pair. a) Near field image of the VCSEL showing the aperture of the VCSEL being illuminated by the spatially modulated laser beam from the SLM with input b), the modulation image displayed on the SLM.

of the VCSEL in order to have high efficiency without the sensitivity of resonance effects. The beam should be absorbed in the active area and not in the Bragg mirrors. Hence, a wavelength in the 900-920 nm region is a good choice. Absorption of photons at this wavelength results in the creation of additional

carriers to the VCSEL. This results in a decrease of refractive index, a blue detuning of the cavity resonance, and thus increases the threshold of a CS. Hence, by aiming more power on the most reddish CS with the lowest thresholds, the thresholds should be equalised at a higher current (note that this is opposite to the situation depicted in Fig. 7.6). However, experimental investigations with a 905 nm control beam showed that the thresholds of the CS were actually reduced indicating that the cavity resonances were actually tuning towards the red. This can be understood by the fact that in practice there is also a thermal component to the refractive index change due to the dissipation of the excess energy of the 905 nm photon compared to the 980 nm band edge leading to heating. The experiments indicate that the thermal red-shift dominates over the carrier-induced blue-shift. This interpretation was reinforced when the locality of a 905 nm beam was tested, as the effect of a local control beam was found to have long-range influence over the entire VCSEL aperture. There was also a delay of some 25 ms between the application of the 905 nm beam and the switching of the CS. Both of these phenomena are compatible with a thermal dissipation mechanism which make a 905 nm control beam unsuitable for spatial compensation applications.

A 978 nm EEL was then used for the compensation beam. It needs to be injected within the resonance width of the VCSEL cavity because it is rejected by the high-reflectivity Bragg output coupler otherwise. In that wavelength range the VCSEL is inverted, hence injection actually reduces the carrier density, increases the refractive index, red-shifts the carrier resonance and hence lowers the thresholds. This situation is indicated in Fig. 7.6. There is no injection at the position of the CS with the lowest threshold (the most reddish CS) and the injection intensity is increased for the other CS in dependence on threshold such that the cavity resonance is equalised at the level of the first CS (lowest threshold situation).

7.2.3 Results: Local Threshold Control

Indeed, a 978 nm beam was found to be capable of lowering the threshold of a CS and the effect was found to be also local, as can be seen in Fig. 7.8. Figure 7.8 is produced by using the SLM to filter out a small circular beam, of similar

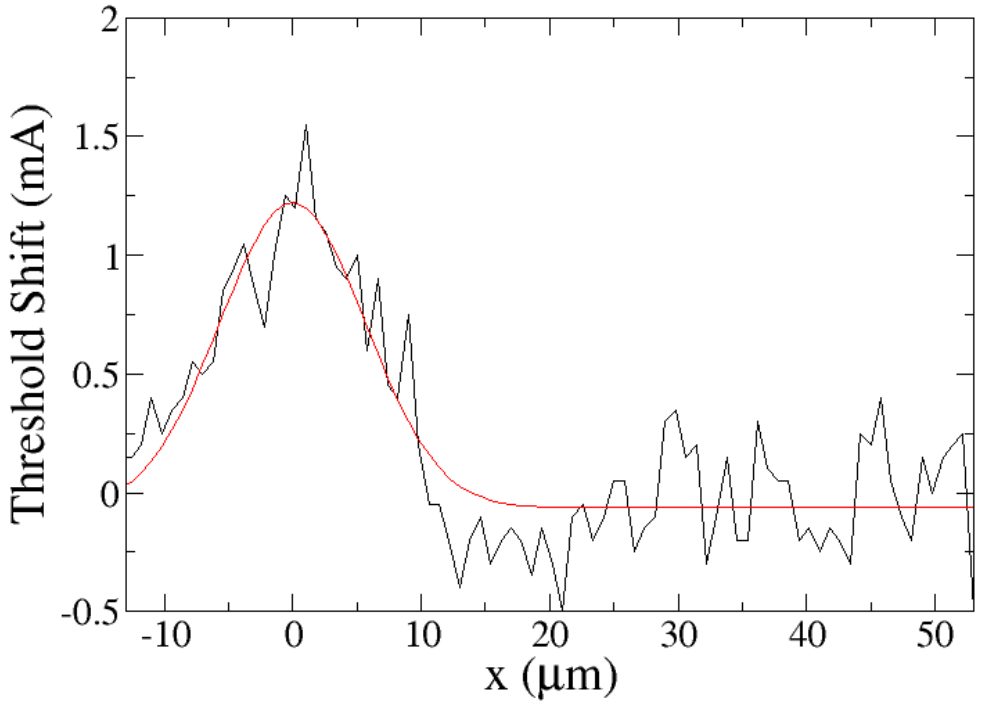

Figure 7.8: Reduction in threshold current of a CS induced by the application of a local 980 nm SLM beam for varying distance to the CS peak. The solid line represents experimental data, dashed red curve is a Gaussian fit to the data.

size to a CS, and directing it close to the location of a known CS. The light-current characteristic (LI-curve, see, e.g., the solid line in Fig. 7.9) for this CS is recorded with the compensation beam switched off, and the 'natural' threshold current is noted. The LI-curve is then repeated with the compensation beam switched on and the new threshold is noted. The LI-curve is then recorded a third time with the compensation beam off again. This is to compensate for any drift of the threshold which occurs due to macroscopic thermal fluctuations. These three LI-curves are compared to obtain the threshold reduction induced by the compensation beam for a particular position of the beam. The beam is then scanned spatially across the CS and the threshold reduction is noted at each point.

Figure 7.8 shows that the threshold reduction is largest when the beam is applied directly on top of the CS, as expected. The threshold reduction reduces rapidly as the beam is moved away from the centre of the CS ($1/e^2$ radius 5 μm) which indicates that the threshold reduction effect with a 980 nm compensation beam is indeed local.

Since the thresholds of the CS are governed by the local cavity resonance it is possible to assess the viability of any compensation scheme by monitoring the relative thresholds of several CS. It should be shown that any compensation scheme is capable of locally adjusting thresholds such that a number of CS which have differing thresholds, are made to share a common threshold.

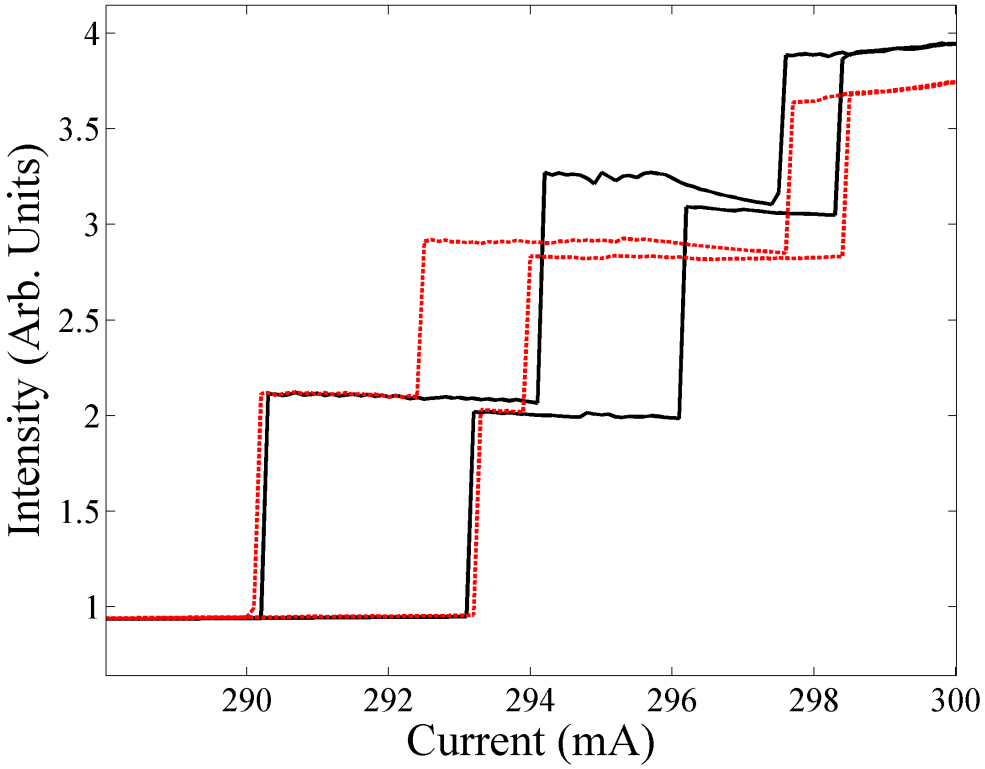

Figure 7.9: Light-Current (LI) characteristics for the system before (solid line) and after (dotted line) the application of the SLM beam.

To this end the system is set up such that it produces three CS with similar thresholds. An LI-curve for these CS is measured, and can be seen as the solid

curve in Fig. 7.9. It shows that the first CS has a threshold around 293 mA, the second around 296 mA and a third around 298 mA. Fig. 7.10a shows the position of the CS when the system is biased in the region where the two CS with lowest threshold are present. A compensation beam is then placed on top of the CS with the second lowest threshold (arrow in Fig. 7.10b) and the LI-curve is measured again. The near-field intensity distribution with the compensation beam on is shown in Fig. 7.10b. The dotted curve in Fig. 7.9 shows the LI-curve which is observed when the compensation beam is applied. There is a clear reduction in threshold current for the second CS, while the first and third remain unchanged. The shift of threshold of the middle CS shows that the system is capable of altering the cavity resonance of the VCSEL, and the lack of shift for the other two CS shows that the system is only shifting cavity parameters locally, which are the two ingredients for a successful compensation scheme. The first and second CS are now simultaneously bistable in a robust current range which they were not before.

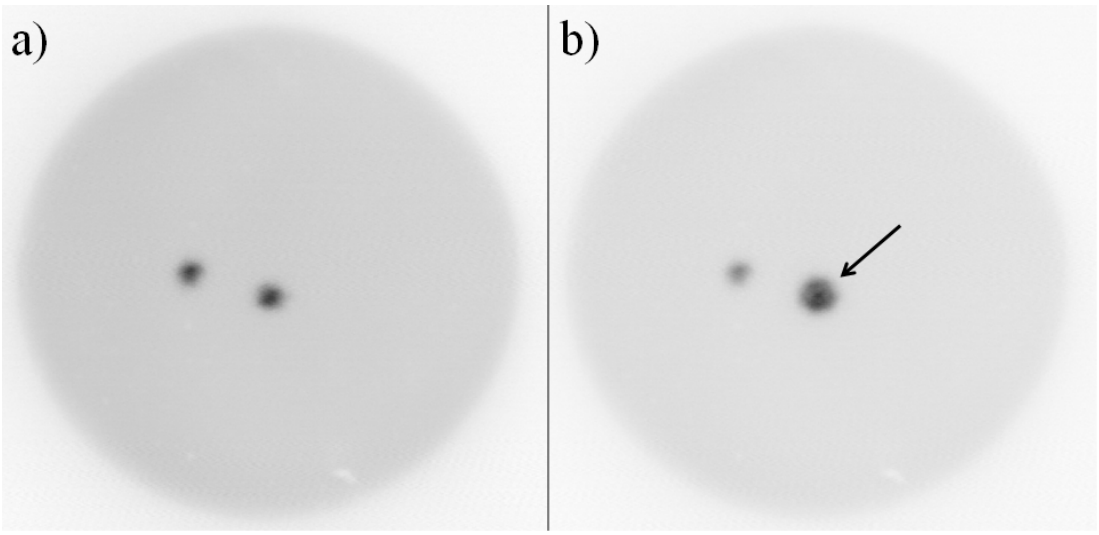

Figure 7.10: Negative intensity (black corresponds to high intensity) near field images of the VCSEL gain region. a) Two CS shown inside the circular VCSEL aperture. b) Application of the SLM beam on top of the right CS. The arrow shows the location of the SLM beam. I=297 mA.

The reported measurements confirm the feasibility of a local threshold correction of semiconductor CS but the system has two main limitations in its current

implementation. The first problem is that as the threshold of a CS is reduced by the application of the SLM beam, the bistable range also reduces. This can be seen in Fig. 7.9 as the difference in bistable widths between the solid line and the dotted line. The width reduces in proportion to the reduction in threshold which places a restriction on how far the threshold may be reduced before bistability is lost.

The second issue with the current realisation is that the power level available for control is rather low due to the low modulation efficiency (smaller 15% at 980 nm) of the SLM used. To achieve a sizable threshold reduction with these low powers, the SLM beam must be tuned in frequency to be resonant with the VCSEL cavity. Since the resonance condition differs between the locations of different CS, it is impossible to have good injection efficiency for more than one CS at a time, making threshold reduction of multiple CS difficult at these power levels. However, a more intense SLM beam would be able to affect CS threshold further off-resonance. This is supported by observations of switch-on thresholds of CS with an external, pulsed laser beam which demonstrate that one can trade detuning versus power [118].

7.2.4 Conclusion

In conclusion the constrains which spatial disorder imposes upon on CS have been outlined; limiting the freedom of location, spreading CS thresholds and thus causing problems for potential applications. The major origin of spatial disorder was inferred to be a spatial variation of cavity resonance. Therefore a scheme in which the cavity resonance is shifted locally via a carrier-induced refractive index change such that the thresholds of different CS may be aligned was realised. The effectiveness of the current realisation is limited by the power available and the resulting reliance on the individual VCSEL resonance conditions. However, an increase in power should allow the scheme to achieve spatial disorder compensation over the full aperture. It is expected that a compensation of the threshold conditions leads also to reduction of the spatial pinning effects. The ultimate goal would be to produce a spatially smoothly varying control beam to counteract the inhomogeneities at any location. This would allow further, more

focussed investigations into specific applications. After compensation is reached, additional modulations like in [20, 49, 87] might be superimposed on top of the compensating beam to control the locations and/or thresholds of CS at will in order to achieve a desired pattern or effect. If the superimposed modulations are random, one might investigate the effects of different strengths of disorder in a controlled way.

In addition, the shape of the necessary modulation for compensation will provide a 'map' of the spatial disorder of the VCSEL resonance and might be a useful diagnostic tool to characterise and understand growth defects in VCSELs. There is a close connection to other approaches to use the sensitivity of solitons to disorder in a kind of 'soliton force microscope' to learn about the parameters of photonic microcavities [5, 89].

Chapter 8

Conclusions

In conclusion, it has been shown that a cavity soliton laser based on a broad-area VCSEL with feedback from a volume Bragg grating is capable of supporting laser cavity solitons. This system has successfully achieved a miniaturisation of previous CSL schemes while also producing unique phenomena.

The LCS produced are localised with radii around 5 μm and Gaussian-like circularly symmetric intensity profiles. The LCS are on-axis within experimental measurement limits and have optical linewidths of the order 6 MHz making them act like micro-lasers. The LCS appear spontaneously when the pump current is increased and the threshold and position of each LCS is believed to be strongly linked with the spatial variation of VCSEL cavity parameters, most likely cavity resonance wavelength. The LCS are most commonly single-peaked at threshold but transition to structures with additional peaks for higher currents. The transitions are believed in tendency to follow a set order with structures with higher peak numbers forming for higher currents. This order is not always realised however due to the spatial disorder on which the LCS reside. The LCS also display a high degree of bistability between the homogeneous off state and the self-localised lasing on state and furthermore display strong bistability between each of the structures with additional peaks.

In comparison to the previous CSL realisation using a diffraction grating the LCS are of similar size however they have marginally narrower optical linewidth. Importantly for application, the VBG scheme has far greater resolution between spatially extended lasing patterns and LCS. The phenomena of structures with

higher numbers of peaks is not found in the diffraction grating scheme however it is present in a scheme employing two face-to-face VCSELs, with that scheme showing the first demonstration of ring-like structures with a phase vortex at the centre. Such structures have been found in numerical simulations of a VCSEL with frequency selective feedback [86] and so may also be present in the VBG scheme and this should be an area of future investigation. The bistability range of each LCS in the VBG scheme is also much larger than the diffraction grating case, typically 5 mA for VBG compared to 1 mA.

The lack of any strongly polarising element within the VBG system results in the LCS being able to choose their own polarisation properties based on local parameters. Simplified polarisation angle measurements reveal that each LCS has a unique polarisation state. This state is controllable via an intra-cavity half wave-plate and this polarisation spread can even be minimised, almost removed, by placing an intra-cavity polariser aligned such that it's polarising axis matches that of all other weakly polarising elements. LCS have essentially constant polarisation properties while it's spatial distribution remains constant, however changes sharply at transitions to structures with more or less peaks and then eventually settling towards a particular polarisation angle for high currents. The diffraction grating CSL does not display this degree of polarisation freedom due to the strongly anisotropic nature of the feedback which only allows polarisation parallel with the table to resonate in the external cavity. These extra degrees of polarisation freedom may allow greater option for applications with possible uses in multiplexing.

The frequency and phase of the LCS are shown to be a free parameter of the system, with each LCS able to choose it's own frequency based on local cavity parameters rather than pinned by externally applied references. The frequency is not totally free however as the LCS must remain within the gain peak and the comb of modes supported by the external cavity This manifests itself as each LCS in general having differing frequency but still within the comb of external cavity modes. Tuning current tunes the frequencies of the LCS until the external cavity mode on which they reside destabilises, forcing a hop to an adjacent cavity mode.

In general the LCS are single longitudinal mode however there is a transition region between external cavity modes in which the LCS operate on multiple ex-

ternal cavity modes, which is shown to result in fast temporal dynamics. These dynamics are not transient and can remain stable for seconds of minutes, limited by the thermal stability of the system. The fast dynamics manifest themselves as oscillations, or in certain cases as pulse-like intensity modulation, with strong evidence of a high modulation depth. The frequency of the oscillations has a tendency to operate on the third and fourth harmonic of the external cavity round trip frequency, making detection more difficult. The short cavity should be responsible for the appearance of fast dynamics, as the round trip time approaches the energy storage time and relaxation oscillation frequency in the VCSEL. Further shortening of the cavity may provide more reliable pulses, with even higher frequency, and is corroborated by the absence of such pulses in the long-cavity scheme used with the diffraction grating. Mode-locked operation has been demonstrated in the system with face-to-face VCSELs [42] by mis-aligning the cavity length however in this region of mode-locking there is no evidence that self-localisation is still present and thus cannot be considered to be a mode-locked LCS.

The LCS are also able to switch-on to an oscillating state, both through a spontaneous switching event and a switch-on induced by the WB. This switch to oscillation is also independent from the state of the other LCS, though it was not proven that this switch does not effect the dynamics of the other LCS due to detection bandwidth limitations imposed by the equipment. It is hoped that this proof can be obtained by simply using the correct equipment. The WB is also capable of producing perturbation induced mode-locking in the form of pulse like modulations when pulses are shone onto an LCS in the on-state. The mechanism for such behaviour is conjectured to be linked to a frequency perturbation which transitions back to the LCS frequency via a branch of unstable solitons, leading to temporal dynamics similar to those shown for a WB-induced switch-on.

It has been shown that if the feedback element is tilted, the frequencies of the LCS can be tuned relative to one another such that several LCS can operate on the same external cavity mode. This leads to the LCS locking in both frequency and phase, manifested as interference fringes in the far field emission with fringe separation corresponding to the separation of the LCS in near field. This is similar to phase locking in bulk, optically pumped semiconductor amplifiers, in which

the frequency of the localised lasing spots is detuned by tilting of the feedback outcoupler mirror and in the CSL the behaviour is rather similar, though in-phase locking is also possible in the CSL due to the lack of a mid-point inversion criteria in the CSL. It would also appear that the locking range is greater in the CSL, with locking demonstrated with LCS separation of up to 18 LCS radii being demonstrated. This long-range coupling seems to resist the explanation of coupling through the field contained in the evanescent tails of the LCS, however it should be noted that at zero detuning a trivially small intensity is required to incite locking, thus this mechanism is still reasonable. Reports on the frequency of the LCS in the face-to-face VCSEL scheme show that under nominal conditions none of the LCS are coherent with each other [40]. This however does not preclude the possibility that tilting the feedback may produce this effect and this phase and frequency locking may still be a possibility in that system.

The switching characteristics of the LCS show that there is a minimum peak power required to switch on an LCS for long pulses. More important for applications is the behaviour at short pulse switching and in this region a quasi-hyperbolic pulse power vs pulse length characteristic is recorded. The energy required does not form an area-law with pulse length however, and one is not expected in the current system since the shortest pulse length (15 ns) is still not short compared to the characteristic timescales involved in the VCSEL (1 ns). Numerical simulations show good agreement with experimental results and show that writing should still be possible down to 1.5 ns [131]. This investigation matches qualitatively what was seen on the diffraction grating CSL, as there as also a lack of an area-law in that system, instead a similar 'skewed area-law' was noted [118], as is the case in the VBG CSL.

There are fast transient dynamics induced during the switch-on, and for a short time after. At the start of the writing pulse, many modes are excited followed by a spectral narrowing until the LCS relaxes to a steady-state or a stable oscillatory mode. Numerical simulations show that these dynamics arise from the excitation of multiple external cavity modes. The optimum frequency with which to write an LCS is numerically found to be some 55 GHz blue detuned to the frequency of the grating peak, which is a good match to the value found qualitatively in the experiment. If the writing pulse is injected at this frequency

then several external cavity modes are excited in this part of the spectrum. This is followed by a spectral broadening coinciding with a fast carrier frequency sweep to the red culminating in a stable frequency settling close to the grating frequency. More interestingly the same frequency excursion is seen when the injected pulse has zero detuning to the final stable frequency. This indicates that there is a global attractor of the system which must pass through the 55 GHz detuning point. This is interpreted as an unstable soliton branch which eventually cascades down to the stable soliton solution. Transient oscillations were present in the diffraction grating CSL however a full spectral analysis was never undertaken, however it seems likely that the behaviour shown in the numerical simulations should hold for most CSL systems capable of operating on multiple external cavity modes.

The operating properties of the LCS are strongly affected by the spatial variation of cavity parameters on which the LCS reside. The measurement and compensation of this 'spatial disorder' is key to future applications. Three methods of disorder measurement were presented with varying benefits. The soliton force microscope (SFM) has the advantage that it probes directly the effect of the disorder on LCS, with no assumptions of the mechanism. SFM measurements with a diffraction grating are problematic due to anisotropic feedback but this is remedied by utilising a volume Bragg grating as the feedback element. This has the problem however that the spatial range of the measurement is extremely limited. The entire device may be mapped by using an external beam to probe the cavity resonance however repeatable measurements are considered to be very difficult due to the critical nature of the external beam alignment. The last solution is to use the device with feedback from a VBG and ramp the current. This has the advantage that all parts of the device are mapped with respect to resonance variation while also being fast, automated, and able to probe even monolithic devices. Hence this appears to be the best candidate for spatial disorder mapping.

With the spatial disorder mapped, the next demonstration showed that it is possible to compensate for such spatial disorder. A spatial light modulator (SLM) was used to inject an external beam locally such that the threshold of one LCS was altered without affecting the thresholds of the other LCS. In this way two LCS which are naturally separated in threshold were brought together to be simultaneously bistable. The end goal would be to bring all LCS to have the

same threshold, and thus would all be simultaneously bistable or even altering the spatial parameters to allow LCS to exist where previously there were none. The current experimental limit does not allow this scenario however as the low modulated power reaching the LCS, coupled with the low modulation capabilities of the particular SLM used means that threshold reduction relies on resonance effects. Due to the fact that each LCS has a different frequency it is therefore impossible to be resonant with two LCS simultaneously. However this problem should be easily overcome by simply using a more powerful laser or a more suitable SLM with greater modulation at the operating wavelength. With these problems overcome the spatial distribution of cavity parameters should be overcome, and even become controllable, making applications more viable, or even expanding the range of possible applications and fundamental studies into phase-locking and pulsing.

If all facets of this thesis can be refined and controlled then one can envisage a whole array of individually addressable, bistable, independent, polarisation multiplexed, mobile LCS which are phase-locked, synchronised and able to produce a pulse-train on demand. This, surely, would be a great step towards all-optical networking.

References

[1] T. Ackemann, 2009. Personal communication. 72

[2] T. Ackemann and W. J. Firth. Dissipative solitons in pattern-forming nonlinear optical systems: Cavity solitons and feedback solitons. In N. Akhmediev and A. Ankiewicz, editors, *Dissipative solitons*, volume 661 of *Lecture Notes in Physics*, pages 55–100. Springer, Berlin, 2005. 2, 62, 67

[3] T. Ackemann, B. Schäpers, J. P. Seipenbusch, Yu. A. Logvin, and W. Lange. Drifting and locking behavior of optical patterns - an analysis using Fourier filtering. *Chaos, Solitons & Fractals*, 10:665–673, 1999. 73

[4] T. Ackemann, S. Barland, M. Cara, S. Balle, J. R. Tredicce, R. Jäger, P. M. Grabherr, M. Miller, and K. J. Ebeling. Spatial mode structure of bottom-emitting broad-area vertical-cavity surface-emitting lasers. *J. Opt. B: Quantum Semiclass. Opt.*, 2:406–412, 2000. 67

[5] T. Ackemann, G.-L Oppo, and W. J. Firth. Fundamentals and applications of spatial dissipative solitons in photonic devices. *Adv. Atom. Mol. Opt. Phys.*, 57:323–421, 2009. 150

[6] T. Ackemann, N. Radwell, and R. Jäger. Optically controllable microlasers and 3d light confinement based on cavity solitons in vertical-cavity devices, Jan 12-14, 2009 2009. Paper TuB2. 2. 14, 96

[7] N. Akhmediev and A. Ankiewicz, editors. *Dissipative solitons*, volume 661 of *Lecture Notes in Physics*. Springer, Berlin, 2005. 1, 14, 110

[8] N. Akhmediev and A. Ankiewicz. Dissipative solitons in the complex Ginzburg-Landau and Swift-Hohenberg equations. In N. Akhmediev and A. Ankiewicz, editors, *Dissipative Solitons*, Lecture Notes in Physics, pages 1–17. Springer, Berlin, 2005. 1, 16

[9] N. Akhmediev and A. Ankiewicz, editors. *Dissipative Solitons: From Optics to Biology and Medicine*, volume 751 of *Lecture Notes in Physics*. Springer, 2008. 1

[10] I.V. Babushkin, M. Schulz-Ruhtenberg, N. A. Loiko, K. F. Huang, and T. Ackemann. Coupling of polarization and spatial degrees of freedom of highly divergent emission in broad-area square vertical-cavity surface-emitting lasers. *Phys. Rev. Lett.*, 100:213901, 2008. 129

[11] M. Bache, F. Prati, G. Tissoni, R. Kheradmand, L. A. Lugiato, I. Protsenko, and M. Brambilla. Cavity soliton laser based on VCSEL with saturable absorber. *Appl. Phys. B*, 81:913–920, 2005. 2

[12] S. Barbay, Y. Ménesguen, X. Hachair, L. Leroy, I. Sagnes, and R. Kuszelewicz. Incoherent and coherent writing and erasure of cavity solitons in an optically pumped semiconductor amplifier. *Opt. Lett.*, 31: 1504–1507, 2006. 67, 73

[13] S. Barbay, X. Hachair, T. Elsass, I. Sagnes, and R. Kuszelewicz. Homoclinic snaking in a semiconductor-based optical system. *Phys. Rev. Lett.*, 101: 253902, 2008. 70, 71

[14] S. Barland, 2008. Personal Communication. 17, 132

[15] S. Barland, J. R. Tredicce, M. Brambilla, L. A. Lugiato, S. Balle, M. Giudici, T. Maggipinto, L. Spinelli, G. Tissoni, T. Knödel, M. Miller, and R. Jäger. Cavity solitons as pixels in semiconductors. *Nature*, 419:699–702, 2002. 2, 16, 17, 19, 43, 62, 67, 73

[16] S. Barland, O. Piro, M. Giudici, J. R. Tredicce, and S. Balle. Experimental evidence of van der PolFitzhughNagumo dynamics in semiconductor optical amplifiers. *Phys. Rev. E*, 68:036209, 2003. 108

[17] V. Yu. Bazhenov, V. B. Taranenko, and M. V. Vasnetsov. Transverse optical effects in bistable active cavity with nonlinear absorber on bacteriorhodopsin. *Proc. SPIE*, 1840:183–193, 1991. 1

[18] P. Bhattacharya, D. Bimberg, and Y. Arakawa. Special issue on optoelectronic devices based on quantum dots. *Proc. IEEE*, 95:1718–1722, 2007. 7

[19] J. Y. Bigot, A. Daunois, and P. Mandel. Slowing down far from the limit points in optical bistability. *Phys. Lett. A*, 123:123–127, 1987. 94, 97

[20] U. Bortolozzo and S. Residori. Storage of localized structure matrices in nematic liquid crystals. *Phys. Rev. Lett.*, 96:037801, 2006. 150

[21] J. Burke and E. Knobloch. Localized states in the generalized Swift-Hohenberg equation. *Phys. Rev. E*, 73:056211, 2006. 1, 16, 70

[22] J. Burke and E. Knobloch. Snakes and ladders: Localized states in the SwiftHohenberg equation. *Phys. Lett. A*, 360:681–688, 2007. 1, 16

[23] A. R. Champneys. Homoclinic orbits in reversible systems and their applications in mechanics, fluids and optics. *Physica D*, 112:158–186, 1998. 1, 16

[24] Igor V. Ciapurin, Leonid B. Glebov, and Vadim I. Smirnov. Modeling of phase volume diffractive gratings, part 1: transmitting sinusoidal uniform gratings. *Optical Engineering*, 45(1):015802, 2006. doi: 10.1117/1.2159470. URL `http://link.aip.org/link/?JOE/45/015802/1`. 28

[25] C. Cleff, B. Gütlich, and C. Denz. Gradient induced motion control of drifting solitary structures in a nonlinear optical single feedback experiment. *Phys. Rev. Lett.*, 100:233902, 2008. 47

[26] M. G. Clerc and C. Falcon. Localized patterns and hole solutions in one-dimensional extended systems. *Physica A*, 356:48–53, 2005. 1, 16

[27] L. A. Coldren and S. W. Corzine. *Diode Lasers and Photonic Integrated Circuits*. Wiley, New York, 1995. 6

[28] D. Cotter, R. J. Manning, K. J. Blow, A. D. Ellis, A. E. Kelly, D. Nesset, I. D. Philips, A. J. Poustie, and D. C. Rogers. Nonlinear optics for high-speed digital information processing. *Science*, 286:1523–1528, 1999. 108

[29] P. Coullet, C. Riera, and C. Tresser. Stable static localized structures in one dimension. *Phys. Rev. Lett.*, 84:3069–3072, 2000. 70, 71

[30] P. Coullet, C. Riera, and C. Tresser. A new approach to data storage using localized structures. *Chaos*, 14:193–198, 2004. 1, 16

[31] A. M. C. Dawes, L. Illing, S. M. Clark, and D. J. Gauthier. All-optical switching in rubidium vapor. *Science*, 308:672–674, 2005. 17

[32] J. H. P. Dawes. Localized Pattern Formation with a Large-Scale Mode: Slanted Snaking. *SIAM J. Dyn. Sys*, 7:186, 2008. 1, 16

[33] T. Elsass, S. Barbay, K. Gauthron, G. Beaudoin, I. Sagnes, and R. Kuszelewicz. Monolithic vertical cavity laser with a saturable absorber: towards an integrated cavity soliton laser, Sep 29 - Oct 2, 2008 2008. 2

[34] T. Elsass, K. Gauthron, G. Beaudoin, I. Sagnes, R. Kuszelewicz, and S. Barbay. Control of cavity solitons and dynamical states in a monolithic vertical cavity laser with saturable absorber. *Euro. Phys. Jour. D*, 59(1):91, 2010. 126

[35] S. V. Fedorov, G. V. Khodova, and N. N. Rosanov. Soliton-like field transverse structures in passive and active optical bistable systems. *Proc. SPIE*, 1840:208–215, 1991. 1

[36] W. J. Firth and A. J. Scroggie. Optical bullet holes: robust controllable localized states of a nonlinear cavity. *Phys. Rev. Lett.*, 76:1623–1626, 1996. 67

[37] W. J. Firth and C. O. Weiss. Cavity and feedback solitons. *Opt. Photon. News*, 13(2):54–58, 2002. 1, 14, 16

[38] W. J. Firth, L. Columbo, and A. J. Scroggie. Proposed resolution of theory-experiment discrepancy in homoclinic snaking. *Phys. Rev. Lett.*, 99:104503, 2007. 70

[39] I. Ganne, G. Slekys, I. Sagnes, and R. Kuszelewicz. Optical switching waves in III-V semiconductor microresonators. *Phys. Rev. B*, 63(7):075318, 2001. 16

[40] P. Genevet. *Laser à solitons et vortex localisés*. PhD thesis, Université de Nice Sophia Antipolis, 2009. 70, 75, 154

[41] P. Genevet, S. Barland, M. Giudici, and J. R. Tredicce. Cavity soliton laser based on mutually coupled semiconductor microresonators. *Phys. Rev. Lett.*, 101:123905, 2008. 2, 74, 105

[42] P. Genevet, B. Barland, M. Giudici, and J. R. Tredicce. Stationary localized structures and pulsing structures in a cavity soliton laser. *Phys. Rev. A*, 79:033819, 2009. 2, 70, 74, 105, 123, 153

[43] P. Genevet, S. Barland, M. Giudici, and J. R. Tredicce. Bistable and addressable localized vortices in semiconductor lasers. *Phys. Rev. Lett.*, 104 (22):223902, Jun 2010. doi: 10.1103/PhysRevLett.104.223902. 70

[44] S. Giet, H.D. Sun, S. Calvez, M.D. Dawson, S. Suomalainen, A. Harkonen, M. Guina, O. Okhotnikov, and M. Pessa. Spectral narrowing and locking of a vertical-external-cavity surface-emitting laser using an intracavity volume bragg grating. *Photonics Technology Letters, IEEE*, 18(16):1786 –1788, aug. 2006. ISSN 1041-1135. doi: 10.1109/LPT.2006.880735. 62

[45] M. Giudici, L. Giuggioli, C. Green, and J. R. Tredicce. Dynamical behavior of semiconductor lasers with frequency selective optical feedback. *Chaos, Solitons & Fractals*, 10:811–818, 1999. 44, 45

[46] G. Giusfredi, J. F. Valley, R. Pon, G. Khitrova, and H. M. Gibbs. Optical instabilities in sodium vapor. *J. Opt. Soc. Am. B*, 5:1181–1191, 1988. 15

[47] D. Gomila and G.-L Oppo. Subcritical patterns and dissipative solitons due to intracavity photonic crystals. *Phys. Rev. A*, 76:043823, 2007. 1, 16

[48] G. Grynberg, A. Maître, and A. Petrossian. Flowerlike patterns generated by a laser beam transmitted through a rubidium cell with a single feedback mirror. *Phys. Rev. Lett.*, 72:2379–2382, 1994. 17

[49] B. Gütlich, H. Zimmermann, C. Cleff, and C. Denz. Dynamic and static position control of optical feedback solitons. *Chaos*, 17:037113, 2007. 150

[50] X. Hachair, L. Furfaro, J. Javaloyes, M. Giudici, S. Balle, J. Tredicce, G. Tissoni, L. Lugiato, T. Maggipinto, and M. Brambilla. Cavity-solitons switching in semiconductor microcavities. *Phys. Rev. A*, 72:013815–1–4, 2005. 97

[51] X. Hachair, F. Pedaci, E. Caboche, S. Barland, M. Giudici, J. R. Tredicce, F. Prati, G. Tissoni, R. Kheradmand, L. A. Lugiato, I. Protsenko, and M. Brambilla. Cavity solitons in a driven VCSEL above threshold. *IEEE J. Sel. Top. Quantum Electron.*, 12:339–351, 2006. 19, 105

[52] M. Haelterman and G. Vitrant. Drift instability and spatiotemporal dissipative structures in a nonlinear Fabry- Perot resonator under oblique incidence. *J. Opt. Soc. Am. B*, 9:1563–1570, 1992. 17

[53] G. K. Harkness, W. J. Firth, G.-L. Oppo, and J. M. McSloy. Computationally determined existence and stability of transverse structures: I. periodic optical patterns. *Phys. Rev. E*, 66:046605, 2002. 1

[54] S.P. Hegarty, G. Huyet, J. G. McInerney, and K. D. Choquette. Pattern formation in the transverse section of a laser with a large Fresnel number. *Phys. Rev. Lett.*, 82:1434–1437, 1999. 11

[55] C. H. Henry. Theory of the linewidth of semiconductor lasers. *IEEE J. Quantum Electron.*, 18:259–264, 1982. 71, 141

[56] K. F. A. Jentsch. *Charakterisierung von oberflächenemittierenden Halbleiterlasern mit optischer Rückkopplung*. Diplomarbeit, Westfälische Wilhelms-Universität Münster, 2006. 62

[57] Ziping Jiang and M. McCall. A theoretical study of coupled laser systems. *J. Mod. Opt.*, 39:159–172, 1992. 19

[58] Jr. K. S. Thornburg, M. Möller, Rajarshi Roy, T. W. Carr, R.-D. Li, and T. Erneux. Chaos and coherence in coupled lasers. *Phys. Rev. E*, 55:3865–3869, 1997. 19, 76, 82, 83

[59] D.M. Kane and K.A. Shore. *Unlocking Dynamical Diversity: Optical Feedback Effects on Semiconductor Lasers*. Wiley, New York, 2005. 43, 45

[60] Ursula Keller and Anne C. Tropper. Passively modelocked surface-emitting semiconductor lasers. *Physics Reports*, 429(2):67 – 120, 2006. ISSN 0370-1573. doi: DOI:10.1016/j.physrep.2006.03.004. URL `http://www.sciencedirect.com/science/article/B6TVP-4K07FKD-1/2/37ad705baf395a9e7a4ec04033d9efdf`. 11

[61] G. Kozyreff and S. J. Chapman. Asymptotics of large bound states of localized structures. *Phys. Rev. Lett.*, 97:044502, 2006. 1, 16

[62] M. Kreuzer, H. Gottschilk, Th. Tschudi, and R. Neubecker. Structure formation and self-organization phenomena in bistable optical elements. *Mol. Cryst. Liquid Cryst.*, 207:219–230, 1991. 15

[63] R. Kuszelewicz, I. Ganne, I. Sagnes, and G. Slekys. Optical self-organization in bulk and multiquantum well gaalas microresonators. *Phys. Rev. Lett.*, 84:6006–6009, 2000. 67, 129, 132

[64] R. Lang and K. Kobayashi. External optical feedback effects on semiconductor injection laser properties. *IEEE J. Quantum Electron.*, 16:347–355, 1980. 45

[65] H. E. Li and K. Iga, editors. *Vertical-cavity surface-emitting laser devices*, volume 6 of *Springer Series in Photonics*. Springer, Berlin, 2003. 7

[66] D. J. B. Lloyd, B. Sandstede, D. Avitabile, and A. R. Champneys. Localised patterns in the 2D Swift-Hohenberg equation. *SIAM J. Dyn. Sys.*, 7:1049, 2008. 1, 16

[67] L. A. Lugiato, F. Prati, G. Tissoni, M. Brambilla, S. Barland, M. Giudici, and J. R. Tredicce. Cavity solitons in semiconductor devices. In N. Akhmediev and A. Ankiewicz, editors, *Dissipative Solitons: From Optics to Biology and Medicine*, Lect. Notes Phys., page 978. Springer, 2008. 19

[68] K. Mahmoud Aghdami, F. Prati, P. Caccia, G. Tissoni, L. A. Lugiato, R. Kheradmand, and H. Tajalli. Comparison of different switching techniques in a cavity soliton laser. *Eur. Phys. J. D*, 47:447455, 2008. 98

[69] G. S. McDonald and W. J. Firth. Spatial solitary-wave optical memory. *J. Opt. Soc. Am. B*, 7:1328–1335, 1990. 15

[70] C. McIntyre, A. M. Yao, G. L. Oppo, F. Prati, and G. Tissoni. All-optical delay line based on a cavity soliton laser with injection. *Phys. Rev. A*, 81 (1):013838, Jan 2010. doi: 10.1103/PhysRevA.81.013838. 105, 128

[71] D. W. McLaughlin, J. V. Moloney, and A. C. Newell. Solitary waves as fixed points of infinite-dimensional maps in an optical bistable ring cavity. *Phys. Rev. Lett.*, 51:75–78, 1983. 15

[72] J. M. McSloy, W. J. Firth, G.-L. Oppo, and G. K. Harkness. Computationally determined existence and stability of transverse structures: II. multi-peaked cavity solitons. *Phys. Rev. E*, 66:046606, 2002. 1, 16, 70

[73] R. Michalzik, M. Grabherr, and K. J. Ebeling. High-power VCSELs: Modeling and experimental characterization. *Proc. SPIE*, 3286:206–219, 1998. 27, 139

[74] F. Mitschke, C. Boden, W. Lange, and P. Mandel. Exploring the dynamics of the unstable branch of bistable systems. *Opt. Commun.*, 71:385–392, 1989. 94, 97

[75] M. Möller, B. Forsmann, and W. Lange. Amplitude instability in coupled Nd:YVO_4 microchip lasers. *Chaos, Solitons & Fractals*, 10:825–830, 1999. 76, 82, 83

[76] J. V. Moloney and A. C. Newell. *Nonlinear Optics*. Addison-Wesley, Redwood City, 1992. 15

[77] A. Naumenko, N. A. Loiko, M. Sondermann, K. F. Jentsch, and T. Ackemann. Abrupt turn-on and hysteresis in a VCSEL with frequency-selective optical feedback. *Opt. Commun.*, 259:823–833, 2006. 20, 81, 88

[78] A. V. Naumenko, N. A. Loiko, and T. Ackemann. Analysis of bistability conditions between lasing and nonlasing states for a vertical-cavity surface-emitting laser with frequency-selective optical feedback using an envelope approximation. *Phys. Rev. A*, 76:023802, 2007. 20

[79] D. A. Neamen. *Semicondictor Physics and Devices; Basic Principles*. McGraw-Hill, New York, 2003. 6

[80] R. Neubecker and T. Tschudi. Self-induced mode as a building element of transversal pattern formation. *J. Mod. Opt.*, 41:885–906, 1994. 15

[81] Y. Nishiura and D. Ueyama. A skeleton structure of self-replicating dynamics. *Physica D*, 130:73–104, 1999. 1, 16

[82] Optigrate, 2010. OptiGrate Corp, 3267 Progress Drive, Orlando, Florida 32826. 28, 29

[83] K. Panajotov, B. Nagler, G. Verschaffelt, A. Georgievski, H. Thienpont, J. Danckaert, and I. Veretennicoff. Impact of in-plane anisotropic strain on the polarization behavior of vertical-cavity surface-emitting lasers. *Appl. Phys. Lett.*, 77(11):1590–1592, 2000. 89

[84] P. V. Paulau, A. J. Scroggie, A. Naumenko, T. Ackemann, N. A. Loiko, and W. J. Firth. Localized traveling waves in vertical-cavity surface-emitting lasers with frequency-selective optical feedback. *Phys. Rev. E*, 75:056208, 2007. 45, 105

[85] P. V. Paulau, D. Gomila, T. Ackemann, N. A. Loiko, and W. J. Firth. Self-localized structures in vertical-cavity surface-emitting lasers with external feedback. *Phys. Rev. E*, 78:016212, 2008. 2, 45, 71, 105

[86] P. V. Paulau, D. Gomila, P. Colet, N. A. Loiko, N. N. Rosanov, T. Ackemann, and W. J. Firth. Vortex solitons in lasers with feedback. *Opt. Express*, 18(9):8859–8866, 2010. URL `http://www.opticsexpress.org/abstract.cfm?URI=oe-18-9-8859`. 152

[87] F. Pedaci, P. Genevet, S. Barland, M. Giudici, and J. R. Tredicce. Positioning cavity solitons with a phase mask. *Appl. Phys. Lett.*, 89:221111, 2006. 150

[88] F. Pedaci, S. Barland, E. Caboche, P. Genevet, M. Giudici, J. R. Tredicce, T. Ackemann, A. J. Scroggie, W. J. Firth, G.-L. Oppo, G. Tissoni, and R. Jäger. All-optical delay line using semiconductor cavity solitons. *Appl. Phys. Lett.*, 92:011101, 2008. 43, 73, 128, 129

[89] F. Pedaci, G. Tissoni, S. Barland, M. Giudici, and J. R. Tredicce. Mapping local defects of extended media using localized structures. *Appl. Phys. Lett.*, 93:111104, 2008. 67, 133, 150

[90] H. Pier and E. Kapon. Photon localization in lattices of coupled vertical-cavity surface-emitting lasers with dimensionalities between one and two. *Opt. Lett.*, 22:546–548, 1997. 129

[91] A. Pikovsky, M. Rosenblum, and J. Kurths. *Synchronization - A universal concept in nonlinear sciences*, volume 12 of *Cambridge Nonlinear Science Series*. Cambridge University Press, Cambridge, 2001. 19

[129] N. Radwell and T. Ackemann. Characteristics of laser cavity solitons in a vertical-cavity surface-emitting laser with feedback from a volume Bragg grating. *IEEE J. Quantum Electron.*, 45:1388–1395, 2009. 75, 76, 91, 142

[130] N. Radwell, T. Ackemann, P. Rose, C. Cleff, and C. Denz. Disorder compensation in a cavity soliton laser using a spatial light modulator, 2010. Submitted for publication in Opt. Exp. 84

[131] N. Radwell, C. McIntyre, A. Sroggie, G.L. Oppo, W.J. Firth, and T. Ackemann, 2010. Accepted for publication in EPJD. 100, 101, 102, 104, 106, 154

[95] J. Renaudier, R. Brenot, B. Dagens, F. Lelarge, B. Rousseau, F. Poingt, O. Legouezigou, F. Pommereau, A. Accard, P. Gallion, and G.-H. Duan. 45 ghz self-pulsation with narrow linewidth in quantum dot fabry-perot semiconductor lasers at 1.5 μm. *Electron. Lett.*, 41:1007–1008, 2005. 127

[96] N. N. Rosanov. *Spatial hysteresis and optical patterns*. Springer Series in Synergetics. Springer, Berlin, 2002. 15, 20

[97] N. N. Rosanov. Transverse patterns in wide-aperture nonlinear optical systems. *Progress in Optics*, XXXV:1–60, 1996. 15

[98] N. N. Rosanov, S. V. Fedorov, and A. N. Shatsev. Curvilinear motion of multivortex laser-soliton complexes with strong and weak coupling. *Phys. Rev. Lett.*, 95:053903, 2005. 19

[99] J. S. Russel. Report on waves. *Brit. Assoc. Adv. Sci.*, pages 311–392, 1844. Report on 14th meeting. Marray, London. 11

[100] T. E. Sale. *Vertical Cavity Surface Emitting Lasers*. Research Studies Press Ltd. and John Wiley & Sons Inc., Taunton and New York, 1995. 7

[101] B. Schäpers, T. Ackemann, and W. Lange. Robust control of switching of localized structures and its dynamics in a single-mirror feedback scheme. *J. Opt. Soc. Am. B*, 19(4):707–715, 2002. 94, 97

[102] A. Schreiber, M. Kreuzer, B. Thüring, and T. Tschudi. Experimental investigation of solitary structures in a nonlinear optical feedback system. *Opt. Commun.*, 136:415–418, 1997. 94, 97

[103] M. Schulz-Ruhtenberg. *Experimental analysis of spatial states in broad-area vertical-cavity surface-emitting lasers*. PhD thesis, Westfälische Wilhelms-Universität Münster, 2008. 27

[104] M. Schulz-Ruhtenberg, I.V. Babushkin, N. A. Loiko, T. Ackemann, and K. F. Huang. Transverse patterns and length-scale selection in vertical-cavity surface-emitting lasers with a large square aperture. *Appl. Phys. B*, 81:945–953, 2005. 27

[105] M. Schulz-Ruhtenberg, Y. Tanguy, R. Jäger, and T. Ackemann. Length scales and polarization properties of annular standing waves in circular broad-area vertical-cavity surface-emitting lasers. *Appl. Phys. B*, 2009. 27, 129

[106] A. J. Scroggie, J. M. McSloy, and W. J. Firth. Self-propelled cavity solitons in semiconductor microresonators. *Phys. Rev. E*, 66:036607, 2002. 108

[107] A. J. Scroggie, J. Jeffers, G. McCartney, and G.-L. Oppo. Reversible soliton motion. *Phys. Rev. E*, 71:046602, 2005. 67

[108] A. J. Scroggie, W. J. Firth, and G.-L. Oppo. Cavity soliton laser with frequency selective feedback. *Phys. Rev. A*, 80:013829, 2009. 2, 43, 44, 45, 69, 81, 99, 101, 102, 105

[109] B. Segard, J. Zemmouri, and B. Macke. Noncritical slowing down in optical bistability. *Opt. Commun.*, 63:339–343, 1987. 94, 97

[110] M. Segev. Solitons: a universal phenomenon of self-trapped wave packets. *Opt. & Photon. News*, 13(2):27, 2002. Introduction to special issue on *Solitons*. 12, 108

[111] J. P. Seipenbusch, T. Ackemann, B. Schäpers, B. Berge, and W. Lange. Drift instability and locking behavior of optical patterns. *Phys. Rev. A*, 56: R4401–R4404, 1997. 17, 73

[112] A. E. Siegman. *Lasers*. University Science Books, Mill Valley, California, 1986. 89

[113] L. Spinelli, G. Tissoni, M. Brambilla, F. Prati, and L. A. Lugiato. Spatial solitons in semiconductor microcavities. *Phys. Rev. A*, 58:2542–2559, 1998. 43

[114] L. Spinelli, G. Tissoni, L. Lugiato, and M. Brambilla. Thermal effects and transverse structures in semiconductor microcavities with population inversion. *Phys. Rev. A*, 66:023817, 2002. 108

[115] G. I. Stegeman and M. Segev. Optical spatial solitons and their interactions: universality and diversity. *Science*, 286:1518–1523, 1999. 1, 12, 84

[116] Mitsuru Sugawara and M. Usami. Quantum dot devices: Handling the heat. *Nature Phot.*, 3:30–32, 2009. 7

[117] Andrzej Tabaka, Krassimir Panajotov, Irina Veretennicoff, and Marc Sciamanna. Bifurcation study of regular pulse packages in laser diodes subject to optical feedback. *Phys. Rev. E*, 70(3):036211, Sep 2004. doi: 10.1103/PhysRevE.70.036211. 110

[118] Y. Tanguy, T. Ackemann, and R. Jäger. Characteristics of switching in a semiconductor based cavity-soliton laser. *Opt. Exp.*, 15:16773–16780, 2007. 2, 3, 20, 102, 149, 154

[119] Y. Tanguy, T. Ackemann, W. J. Firth, and R. Jäger. Realization of a semiconductor-based cavity soliton laser. *Phys. Rev. Lett.*, 100:013907, 2008. 2, 3, 20, 47, 53, 62, 67, 73, 74, 75, 76

[127] Y. Tanguy, N. Radwell, T. Ackemann, and R. Jäger. Characteristics of cavity solitons and drifting excitations in broad-area vertical-cavity surface-emitting lasers with frequency-selective feedback. *Phys. Rev. A*, 78:023810, 2008. 2, 3, 20, 53, 67, 69, 73, 74, 123

[121] V. B. Taranenko, K. Staliunas, and C. O. Weiss. Spatial soliton laser: localized structures in a laser with a saturable absorber in a self-imaging resonator. *Phys. Rev. A*, 56:1582–1591, 1997. 1

[122] V. B. Taranenko, C. O. Weiss, and B. Schäpers. From coherent to incoherent hexagonal patterns in semiconductor resonators. *Phys. Rev. A*, 65:013812, 2001. 73

[123] Dmitry Turaev, Andrei G. Vladimirov, and Sergey Zelik. Chaotic bound state of localized structures in the complex ginzburg-landau equation. *Phys. Rev. E*, 75(4):045601, Apr 2007. doi: 10.1103/PhysRevE.75.045601. 85

[124] A. K. van Doorn, M. P. van Exter, and J. P. Woerdman. Strain-induced birefringence in vertical-cavity semiconductor lasers. *IEEE J. Quantum Electron.*, 34:700–706, 1998. 89

[125] A. G. Vladimirov, G. V. Khodova, and N. N. Rosanov. Stable bound states of one-dimensional autosolitons in a bistable laser. *Phys. Rev. E*, 63(5): 056607, Apr 2001. doi: 10.1103/PhysRevE.63.056607. 85

[126] Wei Zhang, T. Ackemann, M. Schmid, N. Langford, and A. I. Ferguson. Femtosecond synchronously mode-locked vertical-external cavity surface-emitting laser. *Opt. Exp.*, 14:1810–1821, 2006. 111

Publication List

Y. Tanguy, N. Radwell, T. Ackemann, and R. Jäger. Characteristics of cavity solitons and drifting excitations in broad-area vertical-cavity surface-emitting lasers with frequency-selective feedback. *Phys. Rev. A*, 78:023810, 2008. 2, 3, 20, 53, 67, 69, 73, 74, 123

B. Terhalle, N. Radwell, P. Rose, C. Denz, and T. Ackemann. Control of broad-area vertical-cavity surface emitting laser emission *Appl. Phys. Lett.*, 93:151114, 2008.

N. Radwell and T. Ackemann. Characteristics of laser cavity solitons in a vertical-cavity surface-emitting laser with feedback from a volume Bragg grating. *IEEE J. Quantum Electron.*, 45:1388–1395, 2009. 75, 76, 91, 142

N. Radwell, T. Ackemann, P. Rose, C. Cleff, and C. Denz. Disorder compensation in a cavity soliton laser using a spatial light modulator, 2010. Submitted for publication in Opt. Exp. 84

N. Radwell, C. McIntyre, A. Sroggie, G.L. Oppo, W.J. Firth, and T. Ackemann, 2010. Accepted for publication in EPJD. 100, 101, 102, 104, 106, 154

N. Radwell and T. Ackemann. Frequency and Phase locking in a cavity soliton laser. In preparation.